British Geological Survey
NATURAL ENVIRONMENT RESEARCH COUNCIL

Mineralogy, petrography and stable isotope study of methane-derived authigenic carbonates (MDAC) from the Croker Carbonate Slab, CEND 23/25 Survey. Part 1

Land, Soil and Coast Programme

Commissioned Report CR/16/164

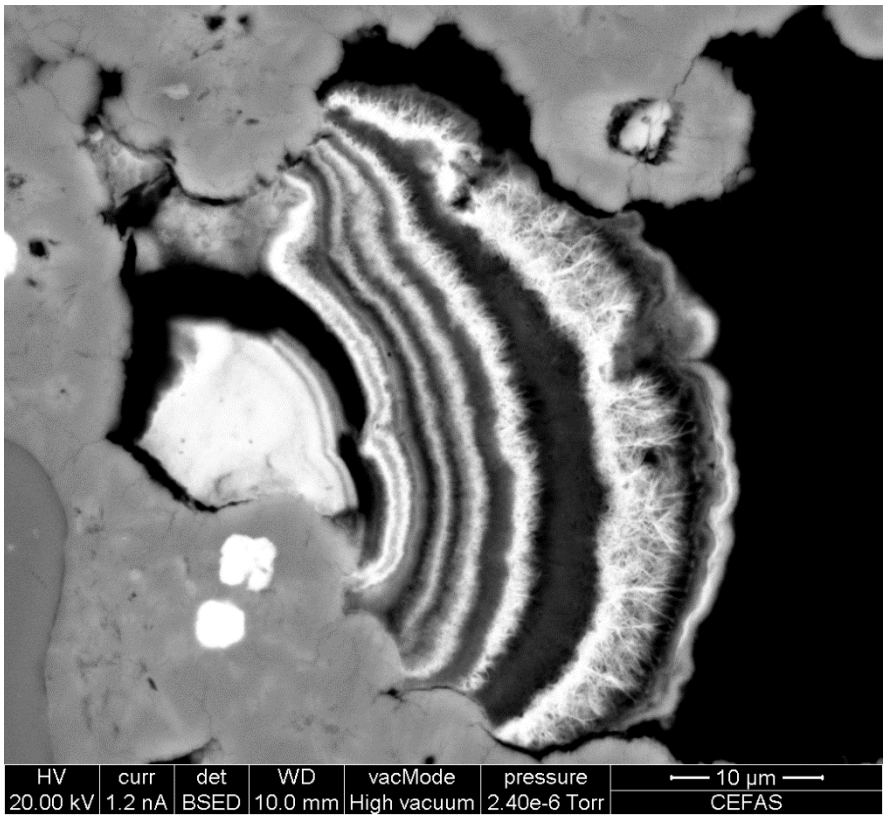

BRITISH GEOLOGICAL SURVEY

LAND, SOIL AND COAST PROGRAMME

COMMISSIONED REPORT CR/16/164

Keywords

Methane derived authigenic carbonate, MDAC, calcite, magnesian calcite, aragonite, dolomite, Irish Sea, Croker, XRD, petrography, BSEM, EDXA, stable isotopes.

National Grid Reference

Not applicable

Map

Not applicable

Front cover

BSEM image of a Mn-rich colloform precipitate from sample GT025.

Bibliographical reference

FIELD, L.P., MILODOWSKI, A.E., WAGNER, D., SLOANE, H., LENG, M.J., AND MARRIOTT, A.L.. 2016. Mineralogy, petrography and stable isotope study of methane-derived authigenic carbonates (MDAC) from the Croker Carbonate Slab, CEND 23/25 Survey. Part 1. *British Geological Survey Commissioned Report*, CR/16/164. 121pp.

Mineralogy, petrography and stable isotope study of methane-derived authigenic carbonates (MDAC) from the Croker Carbonate Slab, CEND 23/25 Survey. Part 1

L.P. Field, A.E. Milodowski, D. Wagner, H. Sloane, M.J. Leng, A.L. Marriott.

Keyworth, Nottingham British Geological Survey 2016

BRITISH GEOLOGICAL SURVEY

The full range of our publications is available from BGS shops at Nottingham, Edinburgh, London and Cardiff (Welsh publications only) see contact details below or shop online at www.geologyshop.com

The London Information Office also maintains a reference collection of BGS publications, including maps, for consultation.

We publish an annual catalogue of our maps and other publications; this catalogue is available online or from any of the BGS shops.

The British Geological Survey carries out the geological survey of Great Britain and Northern Ireland (the latter as an agency service for the government of Northern Ireland), and of the surrounding continental shelf, as well as basic research projects. It also undertakes programmes of technical aid in geology in developing countries.

The British Geological Survey is a component body of the Natural Environment Research Council.

British Geological Survey offices

BGS Central Enquiries Desk

Tel 0115 936 3143 Fax 0115 936 3276

email enquiries@bgs.ac.uk

Environmental Science Centre, Keyworth, Nottingham NG12 5GG

Tel 0115 936 3241 Fax 0115 936 3488
email sales@bgs.ac.uk

The Lyell Centre, Research Avenue South, Edinburgh EH14 4AP

Tel 0131 667 1000 Fax 0131 668 2683
email scotsales@bgs.ac.uk

Natural History Museum, Cromwell Road, London SW7 5BD

Tel 020 7589 4090 Fax 020 7584 8270
Tel 020 7942 5344/45 email bgslondon@bgs.ac.uk

Columbus House, Greenmeadow Springs, Tongwynlais, Cardiff CF15 7NE

Tel 029 2052 1962 Fax 029 2052 1963

Maclean Building, Crowmarsh Gifford, Wallingford OX10 8BB

Tel 01491 838800 Fax 01491 692345

Geological Survey of Northern Ireland, Department of Enterprise, Trade & Investment, Dundonald House, Upper Newtownards Road, Ballymiscaw, Belfast, BT4 3SB

Tel 028 9038 8462 Fax 028 9038 8461

www.bgs.ac.uk/gsni/

Parent Body

Natural Environment Research Council, Polaris House, North Star Avenue, Swindon SN2 1EU

Tel 01793 411500 Fax 01793 411501
www.nerc.ac.uk

Website www.bgs.ac.uk
Shop online at www.geologyshop.com

Foreword

This report is the published product of a study by the British Geological Survey (BGS) commissioned by the Centre for Environment, Fisheries and Aquaculture Science (Cefas) on behalf of the Joint Nature Conservation Committee (JNCC), to undertake petrographic, X-ray diffraction analysis and carbon and oxygen stable isotope compositions of samples of carbonate-cemented sediment recovered from the Croker Carbonate Slabs (Candidate Special Area of Conservation / Site of Community Importance (cSAC/SCI)) of the mid Irish Sea. Cefas recovered a suite of 30 samples as part of a multidisciplinary survey (Cefas cruise CEND 23/15). The objective of this study was to characterise the mineralogy and determine the origin of carbonate-cemented sediment, and in particular, to confirm whether the samples are methane-derived authigenic carbonates (MDAC). This report presents the analyses on all samples including the four samples identified by Cefas as a priority for investigation, which were reported on in BGS report number CR/16/156.

This work was carried out under Cefas purchase orders 20034409 and 20035669: contract reference MPM023-15. The specific objectives of the BGS study were as follows:

1. To undertake whole-sample X-ray diffraction analysis to determine the bulk mineralogy of 30 samples of potential MDAC collected by Cefas, and to confirm the nature of any carbonate cements.
2. To undertake detailed petrographic analysis of 30 polished thin sections prepared each of the potential MDAC samples, by scanning electron microscopy (backscattered electron imaging) with energy-dispersive X-ray microanalysis to characterise the composition of any carbonate cements, after initial optical observation of the thin sections in transmitted light by optical petrographic microscopy.
3. To undertake carbon ($\delta^{13}C$) and oxygen ($\delta^{18}O$) stable isotope analyses of the different carbonate mineral components in each of the potential MDAC samples to establish the origin of the cement.

Due to the size of this report, for convenience, it has been split into two parts:

- Part 1: Introduction, XRD and petrology (samples GT004 to GT0071);
- Part 2: Petrology (samples GT0076 to GT150), oxygen and carbon stable isotope analysis of carbonate cements and other carbonate components, discussion and conclusions.

Acknowledgements

Mr John Fletcher (BGS, Thin Section Laboratory) is gratefully acknowledged for preparing the polished thin sections and blocks from the MDAC samples.

Contents

FIGURES

PLATES

TABLES

Summary

This report describes the petrography and mineralogy on thirty samples of potential methane-derived authigenic carbonate (MDAC) from a programme of work undertaken by the British Geological Survey (BGS) that was commissioned by the Centre for Environment, Fisheries and Aquaculture Science (Cefas), on behalf of the Joint Nature Conservation Committee (JNCC). This work was carried out under Cefas purchase orders 20034409 and 20035669: contract reference MPM023-15. The purpose of the study was to characterise samples of carbonate-cemented fine sandy and silty sediment, recovered by Cefas from the seabed as part of a multidisciplinary survey (CEND 23/15) to Croker Carbonate Slabs cSAC/SCI between 24th October and 6th November 2015, and to ascertain whether the carbonate cements represent MDAC. These samples were collected from an area of active methane seeps, designated as a Candidate Special Area of Conservation (cSAC: UK0030381) and Site of Community Importance (SCI) following identification under the Annex I of the 1992 EC Habitats Directive; in particular, the Annex I habitat *Submarine structures made by leaking gases* (Whormersley et al., 2008). The Croker Carbonate Slabs are located in the mid-Irish Sea (centroid latitude N 53.4725°, longitude W 5.238055556°), approximately 30 km west of Anglesey, comprising a total area of 66 km^2. The seabed surface lies

in approximately 70 m water depth on top of the slabs in the north, descending to approximately 100 m below sea level at their base at the south west corner (JNCC, 2012).

The specific tasks within the BGS analytical programme were as follows:

1. To undertake whole-sample X-ray diffraction analysis to determine the bulk mineralogy of 30 samples of potential MDAC collected by Cefas, and to confirm the nature of any carbonate cements;
2. To undertake detailed petrographic analysis of 30 polished thin sections prepared each of the potential MDAC samples, by scanning electron microscopy (backscattered electron imaging) with energy-dispersive X-ray microanalysis to characterise the composition of any carbonate cements, after initial optical observation of the thin sections in transmitted light by optical petrographic microscopy;
3. To undertake carbon ($\delta^{13}C$) and oxygen ($\delta^{18}O$) stable isotope analyses of the different carbonate mineral components in each of the potential MDAC samples to establish the origin of the cement.

The carbonate cements in these thirty samples can be categorised into two main end-member types:

- *High-magnesian calcite-dominated cements* (e.g. GT004, GT005 and GT112) which contain up to 48 mole % $MgCO_3$ in solid-solution. As such, these cements are at the high-magnesian calcite end of the calcite ($CaCO_3$)-magnesite ($MgCO_3$) solid-solution series (cf. Deer et al., 1962a, b: Mackenzie et al., 1983).
- *Aragonite-dominated cements* with strontium-rich aragonite containing up to 2 mole % $SrCO_3$ in solid-solution (e.g. GT012, GT014, GT106).

Some samples contain a mix of both cements: an early high-magnesian calcite cement, with later acicular aragonite cements. The amount of aragonite varies, from trace amounts of early stage acicular crystals (e.g. GT050), to a major, pore filling cement which coats and encloses, or may partially replace, the earlier high-magnesian calcite cement (e.g. GT106).

Dolomite-dominated cements could not be definitively identified within these samples petrographically, although XRD confirmed the presence of dolomite within some samples, particularly GT024, GT108 and GT123. The increased lattice spacing exhibited by the dolomite in the XRD data from these samples (relative to ideal end-member dolomite) suggests that these dolomite cements may contain up to 10 mole % excess $CaCO_3$ relative to stoichiometric dolomite.

Sample GT141 has preserved interesting sedimentary characteristics, such as syn-sedimentary soft-sediment disturbance features which may be consistent with gas-release from the underlying sediment. In addition, geopetal 'beared-grain' micrite structures in this sample also provide strong evidence for gas accumulation, therefore indicating that the sediment porosity at this site was gas filled during the precipitation of the early micritic high magnesian calcite.

Many samples examined in this study display evidence of extensive bioturbation with burrowing and / or boring by marine organisms (e.g. GT014 and GT015). This has taken place both prior to lithification (e.g. GT143) and boring post-cementation (e.g. GT120). Surfaces of clasts also bear evidence of post-lithification colonisation by encrusting bryozoa, or calcareous serpulid casts. Many of the clasts have been exposed to oxidising conditions on the sea floor resulting in weathered, oxidised surfaces (e.g. GT004, GT0025, GT055). Some samples have developed Fe rich cements and Mn colloform precipitates, and Fe-Mn rich crusts (GT025, GT104, GT117, GT126 and GT129), which may have precipitated directly from overlying seawater in oxidising conditions.

Some samples of the carbonate sediment may well have been collected in-situ, as suggested by their angular nature, the formation of crusts or coatings which may indicate a 'way-up' orientation, and with distinct colonisation by encrusting marine organisms (e.g. GT104, GT106, GT110), However, other samples, most notably GT150, are more likely to have been loose clasts eroded

from their original sediment source. However, overall these samples do not show the high degree of abrasion and erosional surfaces that has been observed in MDAC samples from the Braemar Pockmark Area (Milodowski and Sloane, 2013).

The stable isotope analyses show that the aragonite and magnesian calcite cements have very low $\delta^{13}C_{PDB}$ values which fall between -31.04 to -50.94‰. This is consistent with a diagenetic origin in which carbonate precipitation is related to methane oxidation, and is characteristic of MDAC deposits described in previous reports from both the Mid Irish Sea and Braemar Pockmark Areas (Milodowski et al, 2009; Milodowski and Sloane, 2013). Therefore, our analyses of the aragonite and high-magnesian calcite-cemented sandstones and siltstones recovered from the Croker Carbonate Slabs are consistent with an origin related to MDAC.

1 Introduction

The British Geological Survey (BGS) was contracted by the Centre for Environment, Fisheries and Aquaculture Science (Cefas), to undertake a mineralogical and petrological study of thirty samples of diagenetic, carbonate-cemented sediment samples recovered by Cefas from the seabed as part of a multidisciplinary survey (CEND 23/15) to Croker Carbonate Slabs cSAC/SCI (Figure 1) between 24th October and 6th November 2015. These carbonate-cemented sediments are considered to potentially represent Methane-Derived Authigenic Carbonate (MDAC).

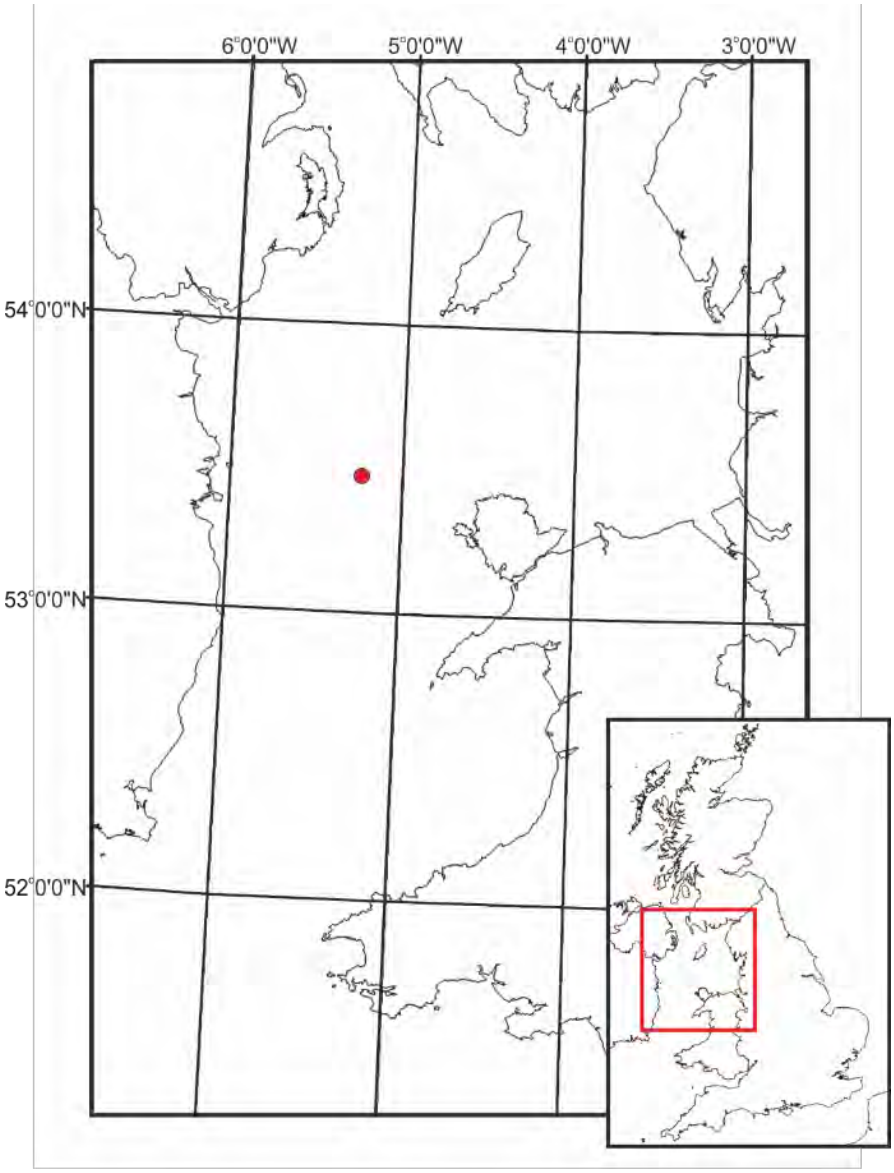

Figure 1. Location of the Croker Carbonate Slabs SCI/cSAC shown by the red dot (centrum N 53.4725°, W 5.238°). The red box in the insert map of the UK shows the approximate area of the enlargement. Map derived from Ordnance Survey data © Crown Copyright and database rights 2016. Ordnance Survey Licence No. 100021290.

The specific objectives and tasks of this phase of the BGS study (under Cefas purchase orders 20034409 and 20035669, contract reference MPM023-15) were as follows:

1. Whole-sample X-ray diffraction analysis to determine the bulk mineralogy of 30 samples of potential MDAC collected by Cefas, and to confirm the nature of any carbonate cements;

2. Petrographic analysis of 30 polished thin sections prepared each of the potential MDAC samples by scanning electron microscopy (backscattered electron imaging) with energy-dispersive X-ray microanalysis to characterise the composition of any carbonate cements. This was done after initial optical observation of the thin sections in transmitted light by optical petrographic microscopy;
3. Determination of carbon ($\delta^{13}C$) and oxygen ($\delta^{18}O$) stable isotope analyses of the different carbonate mineral components in each of the potential MDAC samples to establish the origin of the cement.

This report presents the mineralogical and petrological observations (including, petrographic, X-ray diffraction (XRD) and carbon ($\delta^{13}C$) and oxygen ($\delta^{18}O$) stable isotope analyses) on the carbonate-cemented sediment samples, and discusses these findings in regard to whether the carbonate cements and associated mineralisation can be interpreted to have an MDAC origin.

1.1 GENERAL

The Centre for Environment, Fisheries and Aquiculture Science (Cefas) undertook a survey of the Mid Irish Sea area (Cruise CEND 23/15) to assess the geomorphology, and the distribution and range of seabed habitats, within this area of interest. Interest was focussed on identifying and delineating habitats listed under Annex I of the 1992 EC Habitats Directive; in particular, the Annex I habitat *Submarine structures made by leaking gases* (Whormersley et al., 2008). These features are considered to be of important ecological significance and there is a requirement to adequately characterise these features in order to develop appropriate conservation management plans for such habits in UK offshore waters. The structures consist of carbonate-cemented sediments that are believed to have a Methane-Derived Authigenic Carbonate (MDAC) origin.

1.2 SAMPLES

Thirty-two samples of potential MDAC samples were provided to the BGS, and thirty were chosen for petrological, X-ray diffraction and carbon ($\delta^{13}C$) and oxygen ($\delta^{18}O$) stable isotope analysis in order to characterise the nature and origin of the carbonate cementation (Table 1). They were recovered from the seabed using grab sampling.

Table 1. List of MDAC samples submitted to BGS for analysis

Station code CRKS	Station no	Sample no	Petrography	Whole rock XRD	Stable isotopes	Brief description of hand sample
GT004	160A2	**GT004**	x	x		Light grey cemented medium-grained sandstone. Patchy iron oxyhydroxide stained surfaces. One surface is pock-marked, the other is stained dark brown and contains some borings, and some calcareous serpulid / worm encrustations.
GT005	169A2	**GT005**	x	x		Mid brown, sandstone, friable (lightly cemented) with parallel laminations. Pale orange-brown, iron oxyhydroxide staining. Some shell fragments are cemented onto the surface.
GT007	142A2	**GT007**	x	x		Light grey, medium-grained, cemented sandstone clast. Sub-angular. Minor light orange-brown iron oxyhydroxide staining. Some sediment-infilled burrows present.
GT009	175A3	**GT009**	x	x		Light grey, medium grained, carbonate-cemented angular sandstone clasts containing an assortment of angular to sub-angular grains. The clasts are stained with orange-brown iron oxyhydroxides. The surfaces have evidence of numerous calcareous serpulid, and minor

Station code CRKS	Station no	Sample no	Petrography	Whole rock XRD	Stable isotopes	Brief description of hand sample
						bryozoan encrustations and sediment-infilled burrows.
GT012	184A1	**GT012**	x	x		Light and dark grey speckled, medium-grained, friable, cemented sandstone. Patchy, light orange-brown iron oxyhydroxide staining on the clast surface, and in broadly horizontal bands within the clasts. Some minor bryozoan encrustation, and numerous exposed burrows on surface. Some burrows are infilled with fine-grained silty sediment.
GT014	188A1	**GT014**	x	x		Massive, medium-grained, grey sandstone, heavily bioturbated. Burrows and borings are infilled with dark brown mud and coarse sand. Numerous calcareous serpulid encrustations on the surface.
GT015	174A3	**GT015**	x	x		Massive, fine to medium grained, buff coloured sandstone and siltstone, heavily-bioturbated. Minor bryozoan encrustations on the surface.
GT024	171A3	**GT024**	x	x		Massive, fine-grained, buff-coloured sandstone, with some borings filled with loosely-cemented coarser sand. Minor amounts of shell fragments are present that are cemented onto the surface.
GT025	173A2	**GT025**	x	x		Massive, fine to medium-grained, buff-coloured sandstone, heavily bioturbated. Abundant shell fragments within the cemented sediment, and calcareous serpulid encrustations present on the surface of the sample. Iron oxyhydroxide cement and colloform, pore-lining manganese oxyhydroxide precipitates are present.
GT036	143A2	**GT036**	No analysis			Light grey, fine-grained, well-cemented sandstone. Minor light orange-brown iron oxyhydroxide staining in patches.
GT039	156A3	**GT039**	x	x		Angular to sub-angular clasts of fine to medium-grained, buff coloured sandstone, with some evidence of bioturbation and boring by marine microorganisms. Some light orange-brown iron oxyhydroxide staining is present around the outer edges of the clasts.
GT050	144A1	**GT050**	x	x		Heavily bioturbated, light grey siltstone and buff-coloured sandstone. Numerous borings and some calcareous serpulid encrustations present.
GT055	168A2	**GT055**	x	x		Medium-grained, light grey-buff-coloured, well-cemented sandstone. Some light orange-brown iron oxyhydroxide surface staining. Surfaces patchily-encrusted with bryozoan.
GT066	166A3	**GT066**	x	x		Several sub-rounded knobbly clasts, comprising grey, siltstone and poorly-sorted sandstone with a grain-supported fabric and muddy matrix. Abundant shell fragments and other bioclastic detritus have been incorporated within the carbonate cemented sediment.
GT071	165A3	**GT071**	x	x		Fine-grained, grey-buff carbonate-cemented sandstone. Patchy orange-brown iron oxyhydroxide staining. Minor bioturbation and rare borings.

Station code CRKS	Station no	Sample no	Petrography	Whole rock XRD	Stable isotopes	Brief description of hand sample
GT076	209A2	**GT076**	x	x		Fine-grained, grey-buff sandstone. Some orange-brown iron oxyhydroxide staining. Rare borings. Some bryozoan encrustations on the surface.
GT104	153A2	**GT104**	x	x		Fine- to medium-grained, grey-buff well-sorted, grain-supported sandstone, with lenses of poorly-sorted sandstone with a muddy matrix Some orange-brown to black iron oxyhydroxide staining. Abundant shell fragments included within the cemented sandstone. Numerous calcareous serpulid worm and bryozoan encrustations on the surfaces of the sandstone clasts.
GT106	162A5	**GT106**	x	x		Angular clasts comprising a medium-grained grey sandstone. In places, a fine-grained calcareous coating is visible. The sample has been bioturbated, and is heavily bored by marine microorganisms. Orange to brown-black coating on some surfaces due to iron oxyhydroxide staining.
GT108	148A2	**GT108**	x	x		Medium-grained, grey-buff sandstone. Some orange-brown iron oxyhydroxide staining. Bryozoan, and calcareous serpulid encrustations on the surface.
GT110	203A3	**GT110**	x	x		Coarse grained, well-cemented buff sandstone.
GT112	163A1	**GT112**	x	x		Heavily bioturbated, light-grey, massive siltstone to fine sandstone, with some burrows and borings infilled with coarser-grained sand. Abundant shells and shell fragments incorporated within the carbonate-cemented sandstone. Bryozoan encrustations on surfaces.
GT116	191A2	**GT116**	x	x		Light grey, coarse-grained, grain-supported sandstone with muddy matrix.
GT117	159A5	**GT117**	x	x		Dark grey, well-cemented, medium grained sandstone. Patchy, orange-brown iron oxyhydroxide staining. Bryozoan, and calcareous serpulid encrustations on the surface.
GT120	150A1	**GT120**	x	x		Medium to coarse-grained, light buff, carbonate - cemented bioclastic sandstone, with abundant shells / shell fragments. Some evidence of boring by microorganisms of shell fragments that are now included within the cemented sandstone.
GT121	205A1	**GT121**	x	x		Buff-coloured, medium-grained, cemented sandstone, heavily bioturbated. Bryozoan, and calcareous serpulid worm encrustations, and borings by microorganisms. Orange-brown staining by iron oxyhydroxides.
GT123	178A3	**GT123**	x	x		Dark grey, heavily-bioturbated, fine to very fine-grained, sandstone. Shell fragments and muddy sediment infill some burrows and borings by micro-biota. Bryozoan, and calcareous serpulid encrustations on surfaces.
GT126	186A1	**GT126**	x	x		Medium-grained, highly-bioturbated, grey-buff sandstone. Orange-brown iron oxyhydroxide staining. Bryozoan, and worm casts composed of carbonate-cemented coarse-grained sandstone,

Station code CRKS	Station no	Sample no	Petrography	Whole rock XRD	Stable isotopes	Brief description of hand sample
						and calcareous serpulid encrustations on surfaces.
GT129	207A2	**GT129**	x	x		Light grey, well-cemented, coarse-grained sandstone. Patchy orange-brown iron oxyhydroxide-staining. Pock-marked surfaces containing some borings. One clast has a dark brown-black, manganese oxyhydroxide-rich crust.
GT141	154A2	**GT141**	x	X*		Very pale cream-coloured, coarse-grained, cemented sandstone, heavily bioturbated. Numerous bryozoan and calcareous encrustations on surfaces.
GT143	179A1	**GT143**	x	x		Mid-grey coloured, medium to fine-grained cemented sandstone, some borings of bioclasts by microorganisms. Bryozoan and calcareous serpulid encrustations on the surface.
GT147	195A3	**GT147**	No analysis			Cream-coloured, coarse grained, cemented sandstone, with complete mollusc shells and shell fragments.
GT150	211A1	**GT150**	x	x		Fine-grained, grey- to buff-coloured clasts. Some of which are clearly lithic clasts. No evidence of borings. Some bryozoan encrustations on the surfaces.

*For sample GT141, an additional XRD point analysis of the bryozoan (sea-mat) encrustation was carried out in addition to the whole rock XRD analysis.

1.3 GEOLOGICAL BACKGROUND

The location of the study area (Figure 1) is similar to that described by Milodowski et al., (2009) in an earlier study of MDAC from the Croker Carbonate Slabs area of the Irish Sea. The geological background of the study area is summarised by Whormersley et al. (2008). The study area is underlain by inclined strata of Carboniferous (Dinantian and Westphalian) age. These bedrocks have been weathered and form an irregular unconformity surface that is between 20 to 60 m below the seabed. Carboniferous strata are overlain by the shallow-dipping or sub horizontal sediments of the Quaternary Prograded Facies of the Western Irish Sea Formation, formed during deglaciation of the Irish Sea after the last glacial maximum. The Quaternary sediments are themselves cut by several trenches and scarps that are presumed by Whormersley et al. (2008) to be related to ongoing erosion at the sea floor by tidal currents, possibly augmented by gas escape at the seabed.

A thin veneer of gravely sand containing shell fragments covers much of the study area. This is the active layer being mobilised at the seabed in the current hydrological regime. Larger sediment wave forms are present in the area, with crests running east-west for up to 1 km, but these may not be active. MDAC has previously been identified beneath the active layer, and may be exposed and undercut by seabed erosion (Milodowski et al., 2009).

2 Analytical methods

2.1 X-RAY DIFFRACTION ANALYSIS

Whole rock X-ray diffraction (XRD) analysis was undertaken on 30 samples to confirm the identification of the carbonate cements. For XRD analysis, approximately 10 mm^3 lumps of the rock were ground in pestle and mortar and a c.3 g portion of the ground material was then wet-micronised under acetone for 10 minutes, dried, disaggregated and back-loaded into standard stainless steel sample holders to prepare random-orientated powder mounts for analysis.

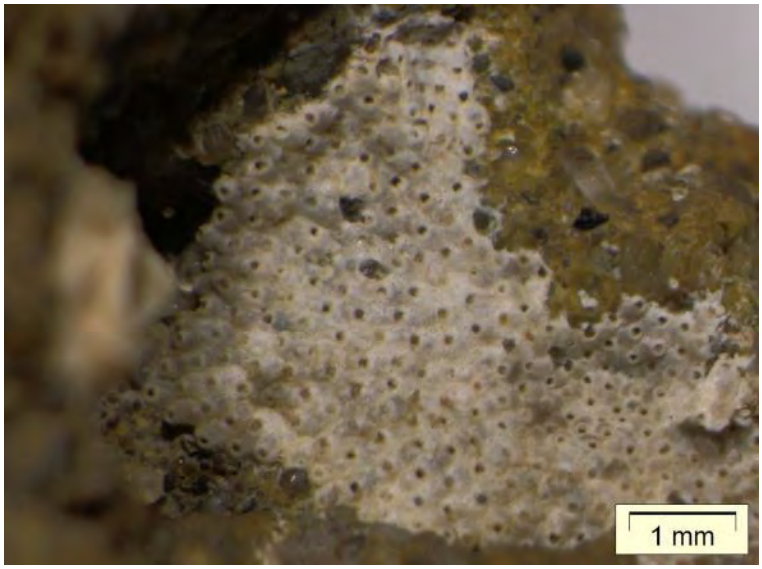

Plate 1. Photograph of sample GT141 showing the white, bryozoan encrustation on which a point XRD analysis was undertaken.

XRD analysis was carried out using a PANalytical X'Pert Pro series diffractometer equipped with a cobalt-target tube, X'Celerator detector and operated at 45 kV and 40 mA. The random powder mounts were scanned from 4.5-85 °2θ at 2.06 °2θ/minute. Diffraction data were initially analysed using PANalytical X'Pert Highscore Plus version 4.1 software coupled to the latest version of the International Centre for Diffraction Data (ICDD) database followed by mineral quantification applying the Rietveld refinement method using PANalytical Highscore Plus software.

For sample GT141, in addition to the whole rock analysis, a small amount of sample was scraped off the white calcareous bryozoan encrustation (Plate 1), then ground in a pestle and mortar and deposited onto the surface of a 'zero-background' silicon crystal using a single drop of acetone. The XRD analysis was carried out as per the whole rock samples.

2.2 PETROGRAPHICAL ANALYSIS

2.2.1 Polished section and polished block preparation

Polished thin sections for petrographical analysis were prepared from small blocks, approximately 40 x 25 x 15 mm, that were sawn from the MDAC samples. The blocks were impregnated with epoxy-resin under vacuum in order to stabilise the material for polished section preparation. A blue dye was added to the epoxy-resin prior to vacuum impregnation to differentiate between porosity originally present within sample and any artefacts of the sectioning process (e.g. grain plucking), when subsequently observed by transmitted-light microscopy. These resin-impregnated blocks were then sliced, and the slice polished to produce polished thin sections 30 µm thick

bonded onto 45 x 28 mm glass microscope slides with a colourless epoxy-resin. The thin sections were finished by polishing with 0.45 µm diamond paste.

The residual counterpart resin-impregnated block to each thin section slice was also polished. This block was then used for microsampling, by microdrilling, of selected areas and types of carbonate mineral material for stable isotope analysis as described in Section 2.3.

2.2.2 Optical microscopy

The polished thin sections were initially scanned, using a digital flatbed scanner, to provide reference images of the whole section/block area. The polished sections were then examined by optical microscopy under plane-polarized light (PPL) and cross-polarized light (XPL) condition, using a Zeiss AxioImager A2m polarizing microscope equipped with a bespoke Zeiss AxioCam ICC5 digital camera. Representative images of key features were recorded in TIFF format at a resolution of 2452 x 2056 pixels, using the Zeiss AxioVision SE64 software package (Release 4.9.1).

2.2.3 Scanning electron microscopy and electron probe microanalysis

Backscattered scanning electron microscopy (BSEM) was used to make detailed high-resolution petrographical observations of the polished thin sections. BSEM analyses were carried out using a FEI QUANTA 600 environmental scanning electron microscope (ESEM) fitted with an Oxford Instruments INCA Energy 450 energy-dispersive X-ray microanalysis (EDXA) system with an Oxford Instruments X-MAX 50 mm^2 Peltier-cooled (liquid nitrogen free) silicon drift detector (SSD). This X-ray detector is capable of operating at very high input X-ray count rates (up to ~10^6 counts per second). The polished sections were coated with a nominally 25 nm thick film of carbon, prior to examination in the ESEM instrument, to make them electrically-conductive. Carbon-coating was carried out using an EMITECH 960L evaporation-coating unit.

The ESEM instrument was operated in conventional high vacuum mode, with a routine electron beam accelerating voltage of 20 kV, and beam probe currents of between 0.71 and 1.2 nA, and a working distance of 10 mm. SEM and BSEM photomicrographs were recorded as 8-bit greyscale TIF digital image over a range of magnifications at a resolution of 1024 x 884 pixels. Image brightness in BSEM images is related to the average atomic number of the phases observed (Goldstein et al., 1981), and this therefore allows differentiation of the minerals observed in polished sections on the basis of the image brightness. Prior to BSEM examination, the polished surface of the thin section was made electrically conductive by coating with a thin layer of carbon (25 nm thick) by vacuum evaporation of carbon.

Mineral/phase identification was aided by micro-chemical information routinely obtained from simultaneous observation of semi-quantitative EDXA spectra recorded from features of interest. EDXA data was acquired and processed using the Oxford Energy INCA Suite Version 5.04 Issue 21a+SP2 (2012) software package. The EDXA system used is capable of detecting elements from atomic number 4 (boron) to atomic number 92 (uranium), and has detection limits of the order of 0.2 to 0.5 wt. % for most common major elements (sodium to iron). Quantitative energy-dispersive electron probe microanalysis (ED-EPMA) of the carbonate cements observed in polished thin section was also undertaken using the same instrumentation. Quantitative ED-EPMA were preformed using a 20 kV electron beam, 1.2 nA beam currents at a working distance of 10 mm. EDXA spectra were processed and quantified using the INCA analysis software package detailed above. The EDXA system was calibrated by reference to individual element X-ray spectra recorded from pure metal, oxide and known mineral standards that are normalised against the X-ray spectrum from pure cobalt recorded under the same operational conditions. Cobalt is subsequently used as an internal reference against which sample spectra are normalised.

2.3 STABLE ISOTOPE ANALYSIS

One hundred and fifty sub-samples of MDAC were analysed to determine oxygen and carbon isotope ($\delta^{18}O$ and $\delta^{13}C$) composition of the carbonate components. These included bulk cement samples and targeted subsamples, recovered by microsampling discrete areas of the polished blocks that contained (or were dominated by) specific generations or types of carbonate (including bioclasts and cement types). The areas for microsampling were initially identified from optical microscopy and SEM observations carried out previously on the corresponding polished thin sections. This methodology has been very successfully used in previous studies to sample and analyse discrete generations of carbonate mineralisation in intergrown polymineralic or multi-generation carbonate cements (Milodowski et al., 2005).

Microsampling was undertaken using a diamond-tipped microdrill, whilst observing the block sample in reflected light under an optical microscope. The microdrill was capable of drilling, and retrieving material from areas as small as 100 µm. However, in order to obtain sufficient material for analysis areas up to 1 mm diameter were drilled. After microdrilling, the microdrilled areas in each block were examined by BSEM-EDXA to verify the mineralogical identity of the material sampled for stable isotope analysis.

Approximately 50-100 micrograms of carbonate are used for isotope analysis using an IsoPrime dual inlet mass spectrometer plus Multiprep device. Samples are loaded into glass vials and sealed with septa. The automated system evacuates vials and delivers anhydrous phosphoric acid to the carbonate at 90 °C. The evolved CO_2 is collected for 15 minutes, cryogenically cleaned and passed to the mass spectrometer. Isotope values ($\delta^{13}C$, $\delta^{18}O$) are reported as per mille (‰) deviations of the isotopic ratios ($^{13}C/^{12}C$, $^{18}O/^{16}O$) calculated to the VPDB (Vienna Pee Dee Belemnite) scale using a within-run laboratory standard calibrated against NBS-19. The Calcite-acid fractionation factor applied to the gas values is 1.00798 dolomite-acid =1.00873 and aragonite 1.00782. Due to the long run time of 21 hours a drift correction is applied across the run, calculated using the standards that bracket the samples. The Craig correction is also applied to account for $\delta^{17}O$. The average analytical reproducibility of the standard calcite (KCM: Keyworth carbonate marble) is 0.08‰ for $\delta^{13}C$ and $\delta^{18}O$.

3 X-ray diffraction analysis

3.1 WHOLE ROCK X-RAY DIFFRACTION

Quantitative whole rock XRD analysis was carried out on each of the samples and the carbonate mineral contents are given in Table 2 and non-carbonate mineral contents are given in Table 3 (Iron oxyhydroxides, silicates and clay minerals).

All thirty samples were found to contain calcite and/or magnesian-calcite in variable amounts, ranging from trace levels (<0.5% e.g. GT150), to GT050 with 14.5 % (total of calcite and magnesian calcite combined). Much of the calcite (i.e. non-magnesian calcite) reflects the presence of abundant fragmental shell material within the samples (clearly seen in thin sections during petrographic analysis – see Section 4).

Aragonite was also identified in many of the samples, in varying amounts ranging from trace amounts (<0.5% aragonite) up to 59.5% aragonite in sample GT106. Some of the aragonite detected by XRD may be due to the presence of molluscan shell fragments (mollusc shells can be composed of aragonite and/or calcite). However, petrographic analysis shows that much of the aragonite in these samples is present as authigenic cement Section 4). Aragonite is the dominant carbonate mineral in nine of the samples: GT012, GT066, GT104, GT106, GT110, GT116, GT120, GT121 and GT141. Only four samples did not contain any detectable aragonite: GT004, GT015, GT024 and GT129. Most of the samples that are dominated by aragonite had very low contents of both magnesian-calcite or the carbonate defined here (Table 2) as “very high

magnesian calcite" (see further discussion below on its identification): where aragonite content was over 14%, magnesian-calcite content was <3%.

Dolomite was identified by XRD in eight of the samples (Table 2). In three of these, dolomite was present as a major component: GT024 (14.7 % dolomite), GT150 (24.4 % dolomite) and GT123 (9.6 % dolomite). Although the highest dolomite content was recorded from one of the clasts in sample GT150 the actual clast that was selected for sectioning and SEM analysis proved to contain no carbonate. This demonstrates that the clasts in sample GT150 are very heterogenous.

Although identified by XRD, dolomite could not be clearly distinguished by either qualitative BSEM-EDXA or quantitative ED-EPMA analysis. In some cases, petrographic analysis revealed that the magnesium-rich micritic carbonate matrix was intimately intergrown with fine grained low-magnesian calcite (e.g. see sample GT123: Part 2, Sample GT123, Plate 67). Consequently, any ED-EPMA analyses of the matrix carbonate would have represented unresolved mixtures of calcite and dolomite within the analytical volume of the electron beam. Furthermore, because the average atomic number of dolomite and magnesian-calcite with a high degree of magnesium substitution are very similar, there is insufficient backscattered electron contrast (cf. Goldstein et al., 1981) to differentiate these two minerals in the BSEM images. This difficulty in differentiation is further compounded by the fine grained nature of the matrix carbonate. Some of the high resolution BSEM observations do indicate the presence of euhedral rhombic microcrystals (microsparry cement) nucleated around microporous aggregates of anhedral micrite particles. These more crystalline microcrystals resemble the typical rhombic morphology commonly found in dolomite cements. Some of the ED-EPMA data from the very magnesium-rich carbonate cements approach dolomite in composition with up to 47 mole % $MgCO_3$ (e.g. sample GT129). These higher $MgCO_3$ compositions could be interpreted to represent dolomite with excess calcium. Non-stoichiometric dolomite cements with excess $CaCO_3$ are often associated with low-temperature diagenetic systems (see: Skinner, 1963; Searl, 1994), and have been recorded previously from MDAC deposits (Jensen et al., 1992; Milodowski and Sloane, 2013). Reeder (1983) suggests that the maximum extent of solid-solution of Ca^{2+} in dolomite is limited to about 57 mole % $CaCO_3$, even in low-temperature (diagenetic) systems. The composition of dolomite cements (3 to 8 mole % excess $CaCO_3$) studied previously, from MDAC deposits in the Irish Sea (Milodowski et al., 2009), Braemar pockmark in the North Sea (Milodowski and Sloane, 2013), and the Kattegat off the coast of Denmark (average composition $Ca_{0.53}Mg_{0.47}CO_3$ - described by Jensen et al., 1992), are consistent with this compositional limit.

Table 2. Quantitative XRD results for carbonate mineralogy (weight % of total sample)

	Carbonate minerals					
Sample no	Aragonite %	Calcite %	Mg-calcite %	Dolomite %	Very high Mg-calcite	
					%	XRD [104] *d*-spacing (Å)
GT004		3.9	3.2		22.8	2.910
GT005	0.5	4.6	1.1		13.1	2.913
GT007	<0.5	3.5	1.0		11.4	2.911
GT009	0.5	4.6	0.6		15.4	2.918
GT012	14.0	4.6	1.0		2.7	2.930
GT014	5.1	5.1	1.1		16.9	2.916
GT015		5.2	0.9		7.2	2.912
GT024		4.0	0.5	14.7		
GT025	<0.5	4.7	4.3		9.2	2.931
GT039	<0.5	5.0	1.2		5.9	2.931

	Carbonate minerals					
Sample no	Aragonite %	Calcite %	Mg-calcite %	Dolomite %	Very high Mg-calcite	
					%	XRD [104] *d*-spacing (Å)
GT050	2.8	8.4	6.1		28.9	2.935
GT055	<0.5	4.0	1.9		10.5	2.921
GT066	21.0	5.5	0.8	<0.5	<0.5	2.934
GT071	1.2	6.2			9.7	2.926
GT076	5.5	4.6	0.5		11.3	2.922
GT104	35.1	4.2			1.1	2.920
GT106	59.5	2.3			0.5	2.920
GT108	4.1	5.0	1.0	3.6	16.9	2.918
GT110	26.6	2.5		<0.5		
GT112	1.0	4.0	<0.5		20.5	2.912
GT116	37.6	5.0		1.0		
GT117	6.5	3.6	0.6		10.9	2.917
GT120	51.7	4.0	<0.5		<0.5	2.914
GT121	24.8	4.3	0.7		1.8	2.929
GT123	1.7	4.1	<0.5	9.6	10.8	2.923
GT126	0.7	3.2	<0.5		31.1	
GT129		3.6	<0.5		22.6	2.911
GT141	38.7	3.5	<0.5	1.5		
GT143	2.7	3.5	<0.5		15.8	2.910
GT150	1.0	<0.5		24.4		

Table 3. Quantitative XRD results for non-carbonate mineralogy: iron oxides, oxyhydroxides, silicates and clay minerals (weight % of total sample)

	Fe-oxides (%)		Silicates (%)			Clay minerals (%)	
Sample no	hematite	goethite	plagioclase	K-feldspar	quartz	chlorite	mica'
GT004	<0.5		4.3	3.8	59.2	<0.5	2.3
GT005	<0.5		4.7	3.8	69.5	0.5	2.1
GT007	<0.5		4.9	5.1	70.6	<0.5	2.7
GT009	<0.5	2.3	4.1	4.1	63.1	1.1	4.0
GT012	<0.5		3.2	3.5	67.7	0.6	2.6
GT014	<0.5		3.5	3.2	61.2	0.6	3.2
GT015	<0.5		4.4	4.1	74.8	0.6	2.7
GT024	<0.5		4.8	4.2	68.5	0.6	2.4
GT025	<0.5		3.8	5.1	70.1	<0.5	2.0
GT039	<0.5		3.9	4.6	75.5	<0.5	2.9
GT050	<0.5		2.8	4.8	39.7	2.0	4.2
GT055	<0.5		4.2	5.0	70.1	0.6	3.0
GT066	<0.5		2.9	2.1	64.0	0.6	2.3
GT071	<0.5		5.1	5.8	68.0	0.7	3.0

	Fe-oxides (%)		Silicates (%)			Clay minerals (%)	
Sample no	hematite	goethite	plagioclase	K-feldspar	quartz	chlorite	mica'
GT076	<0.5		4.6	2.9	68.0	0.5	1.9
GT104	<0.5		2.8	3.8	51.2	<0.5	1.3
GT106	<0.5		0.7	2.1	33.6	<0.5	0.8
GT108	<0.5		4.8	2.9	58.1	0.7	2.6
GT110	<0.5		1.8	1.0	65.6	<0.5	1.7
GT112	<0.5		4.6	4.1	62.5	0.9	1.7
GT116	<0.5		1.5	2.4	49.4	0.8	2.2
GT117	<0.5		3.2	2.9	69.4	0.5	2.2
GT120	<0.5		0.8	1.3	39.7	<0.5	1.3
GT121	<0.5		2.3	1.8	61.4	0.6	2.1
GT123	<0.5		3.1	2.9	64.5	0.6	2.2
GT126	<0.5		2.8	3.9	54.9	<0.5	2.9
GT129	<0.5		4.2	3.6	61.6	1.0	2.7
GT141	<0.5		1.4	2.4	50.2	<0.5	1.5
GT143	<0.5		3.3	2.7	68.7	0.6	2.2
GT150	<0.5		5.5	9.6	44.9	2.0	12.0

The XRD analyses also indicated the presence of another major carbonate mineral component, with diffraction spacings that could be interpreted as "non-ideal" dolomite, and that is different to the definitive dolomite identified in some of the samples. However, the diffraction spacings could possibly be interpreted to represent calcite with an exceptionally-high degree of magnesium substitution (referred to here as "*very high Mg-calcite*"), and appears to be a major component of the carbonate cement in many of the samples (Table 2). Magnesium substitution in calcite reduces the crystal lattice spacing (magnesium being a smaller cation than calcium). Crystallographic studies (Althoff, 1977; Reeder, 1983) have shown that the dimensions of the crystal unit cell of disordered magnesian calcites decreases linearly with increasing substitution of Ca^{2+} by Mg^{2+}. Therefore, assuming a linear relationship in the XRD lattice diffraction spacings between pure calcite with 0 mole % $MgCO_3$ (*d*-spacing for main [104] plane at 3.03 Å) and magnesite at 100 mole % $MgCO_3$ (*d*-spacing for main [104] plane at 2.742 Å) the variation in the *d*-spacing for the [104] plane (Figure 2) can be used to estimate the amount of $MgCO_3$ in solid-solution in the calcite. If this linear relationship holds true, then the observed *d*-spacing (2.910 to 2.935 Å: Table 2) for this phase in these samples could equate to between 32.8 to 41.4 mole % $MgCO_3$ substitution in calcite. This is significantly more calcic than the 57 mole % $CaCO_3$ solid-solution limit for calcium-rich dolomite (Reeder, 1983). Its predicted composition from XRD (Figure 2) is consistent with that obtained by ED-EPMA from the higher magnesium carbonate cements found in these MDAC samples (described in Section 4). As such, these cements (with >57 mole % $CaCO_3$) are at the high-magnesian calcite end of the calcite-magnesite solid-solution series, and probably represent metastable disordered high-magnesian calcite rather than ordered dolomite with excess calcium (see Deer et al., 1962a, b; Reeder, 1983; Mackenzie et al., 1983). This very high magnesian calcite may comprise up to 31 % of some of the samples (Table 2).

Sample GT123 had similar dolomite and very high magnesian-calcite values at 9.6% and 10.8% respectively.

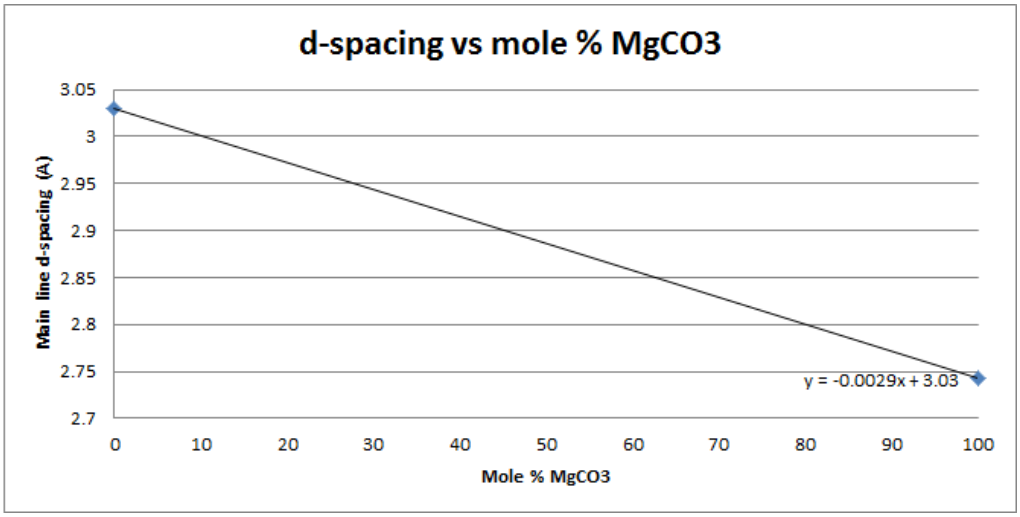

Figure 2. Predicted variation in the main X-ray diffraction spacing ([104] plane) with magnesium-substitution in calcite, assuming a linear relationship between end-member calcite and magnesite.

3.2 GT141 XRD POINT SAMPLE ANALYSIS

Quantitative XRD analysis of material scraped directly from the bryozoan encrustation (Figure 3) from sample GT141 showed that this subsample is predominantly composed of quartz (50.7%) and subordinate amounts of calcite (28%) and aragonite (21.2%). This shows that the bryozoan encrustation comprises both polymorphs of calcium carbonate: i.e. calcite and aragonite. The quartz present within the XRD subsample will be derived from the silty-sandy sediment substrate included within the analysed sub-sample, during scraping the bryozoan encrustation.

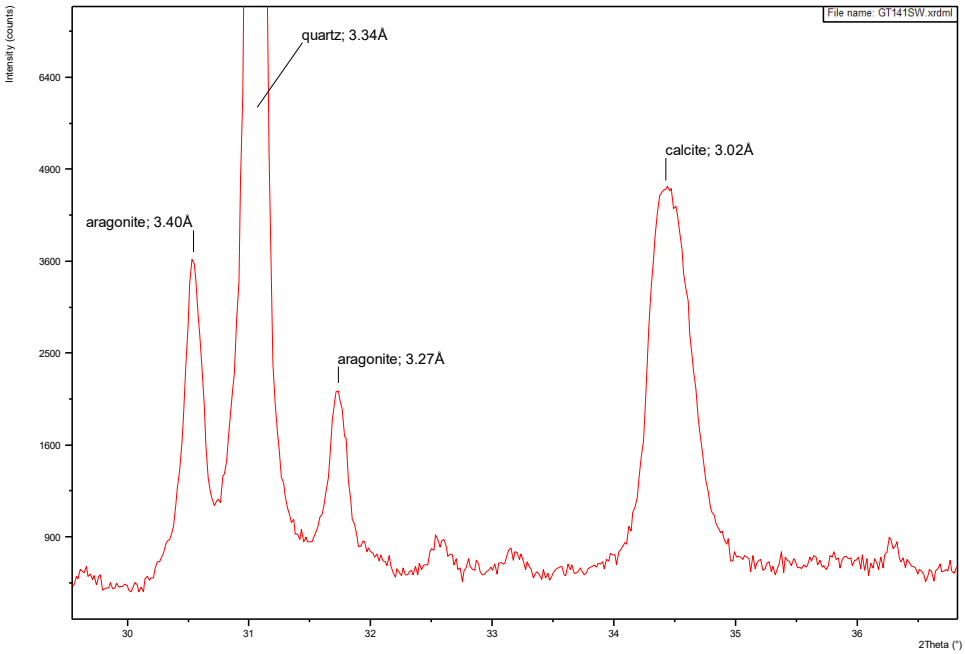

Figure 3. XRD trace for point analysis of the bryozoan encrustation on sample GT141

4 Petrology

4.1 SAMPLE GT004

Sample GT004 comprised a single, tabular clast (<35 mm thick), approximately 170 mm diameter (Plate 2). The clast consisted of light grey, cemented, medium-grained sandstone with a patchy brown iron oxyhydroxide-stained surface. One surface of the clast is pitted with pockmarks of uniform size (approximately 4 mm diameter). The opposite side of the clast is stained a darker brown and contains evidence of borings and calcareous serpulid / worm encrustations.

Plate 2. Photograph showing sample GT004. One surface (shown) is pitted with small pockmarks approximately 4 mm across. The other side does not display such a regular texture. Some calcareous serpulid / worm encrustations are visible on the surfaces. Field of view ~180 mm wide.

A scan of the polished thin section prepared through sample GT004 is shown in Plate 3. The sample comprises fine to medium sandstone with variable carbonate variable carbonate cementation, with a largely grain-supported fabric. The thin section displayed three lithotypes in horizontal layers: (i) a well-cemented, poorly-sorted (muddy), iron oxyhydroxide stained brown sandstone layer; (ii) a discontinuous or lensoid, highly porous and relatively clean sandy layer, and; (iii) a sandstone layer which is carbonate-cemented but is less highly stained (also refer to Plate 4). The sample is dominated by detrital quartz, with subordinate feldspar sand. Detrital grains are largely sub-angular to sub-rounded (<400 µm). Numerous rounded, detrital or pelloidal grains of glauconite ("glauconie" *sensu lato*) are also present (Plate 5). Shell fragments are minor to rare components, and are fine-grained (<500 µm). Secondary, oversized pore spaces resulting from the dissolution of primary grains (cf. Schmidt and McDonald, 1979) are observed both within the well-

cemented and less-well cemented portions of the sample. The sandstone shows little evidence of burial compaction, demonstrating generally "open" grain-packing with simple point-contacts between detrital grains.

The matrix of the sample is micritic, high-magnesian calcite, which has formed as microcrystalline rims around grains (sometimes preferentially nucleated on detrital calcium carbonate grains and calcareous bioclasts), and as "globular "clots" or spherical aggregates of microcrystalline calcite. High-resolution BSEM observations show that the micritic high-magnesian calcite cement comprises spherical to micro-boytryoidal aggregates up to 50 µm diameter (e.g. Plate 6 and Plate 7), which typically have a microporous core and a coarser blocky, more crystalline (microsparite) overgrowth rim of euhedral (idiomorphic) rhombs. BSEM also shows that these rhombs also form rims lining the intergranular pores and walls of larger cavities. The development of larger rhombic calcite crystal rims around detrital grains and lining intergranular pore space (Plate 7) may be due to recrystallisation and coarsening-up of the cement at the expense of the finer micritic carbonate cement.

In some areas, the high-magnesian calcite was observed to contain microscopic cavities (<2 µm), around which the calcite crystals appear to have nucleated (Plate 7). These tiny cavities are similar in size to bacterial cells, and although no internal microstructure can be seen these cavities might possibly represent bacterial cells around which the carbonate may have precipitated. These cellular microfabrics closely resemble some fossilised and mineralised bacterial cells described from experimental studies and other environments in the literature (c.f. Martill and Wilby, 1994; Wilby and Whyte, 1995). Some of the larger cavities within the carbonate cement could also potentially have originated as former gas bubbles trapped in the sediment.

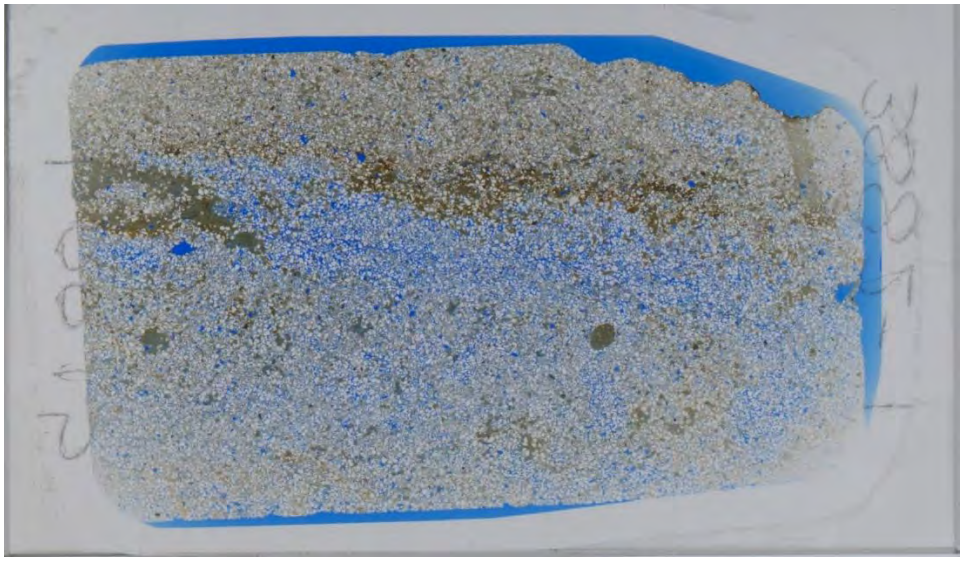

Plate 3. Scan of sample GT004 polished thin section. Cementation, intergranular porosity (shown by blue-dyed resin impregnation) and dark brown iron oxyhydroxides staining are heterogeneously distributed across the sample. Some evidence of patchy, diffuse burrows infilled with fine muddy sediment is present. Field of view = 48 mm wide.

Minor fine (<7 µm) framboidal iron oxide or oxyhydroxide (hereafter referred to as iron oxyhydroxide) was observed to be disseminated within the microporous micrite, and clay-rich areas, but no discrete pyrite was identified. It is likely that the framboidal iron oxyhydroxide represents pseudomorphs after early diagenetic framboidal pyrite (which is morphologically similar). Finely disseminated iron oxyhydroxide also stains the matrix of the sandstone in general, and in particular is concentrated within a discontinuous diffuse band, parallel to, and about 5 to 10 mm from one of the tabular surfaces of the clast (Plate 3). Although the way-up orientation of the

clast unknown, this oxidative alteration is concentrated along the interface between the layers of well-cemented and weakly cemented, porous sandstone (Plate 3), with the iron oxyhydroxide being predominantly precipitated within the micritic carbonate-cemented layer (Plate 4). Some of the darker iron oxide may be more crystalline hematite rather than iron oxyhydroxide, since traces (<0.5 %) of hematite were detected by XRD (Table 3). The concentration of iron oxide mineralisation along this sedimentary interface suggests that the iron oxide formed *in situ* in the sandstone, and may be indicative of some oxidative alteration of the carbonate-cemented sediment on the seabed.

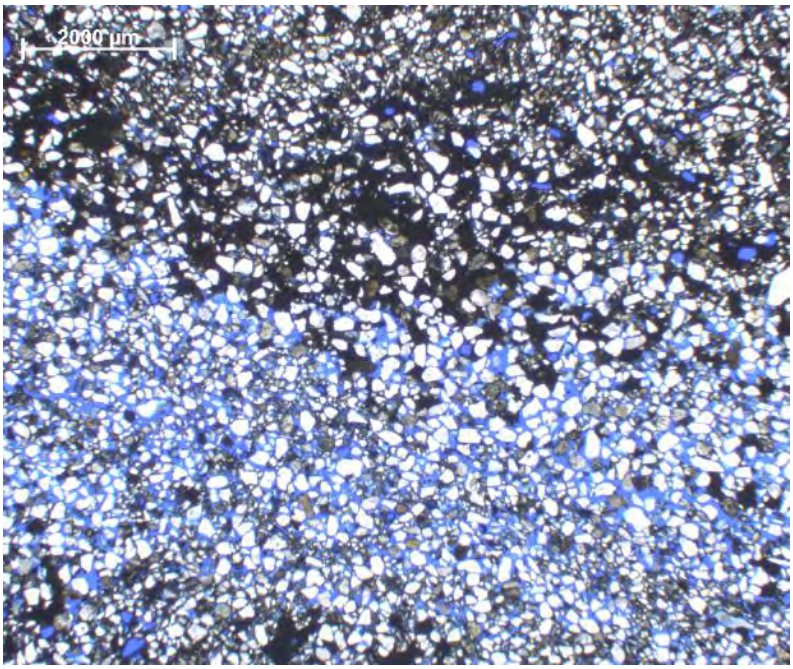

Plate 4. Transmitted light photomicrograph (plain polarised light) showing the contrast in porosity between a well-cemented sandstone stained by opaque iron oxyhydroxide and a more porous weakly-cemented sandstone layer. Secondary oversized pore spaces (large blue-resin-impregnated pores) are present (see lower left corner of image and upper right, within the cemented area). Sample GT004.

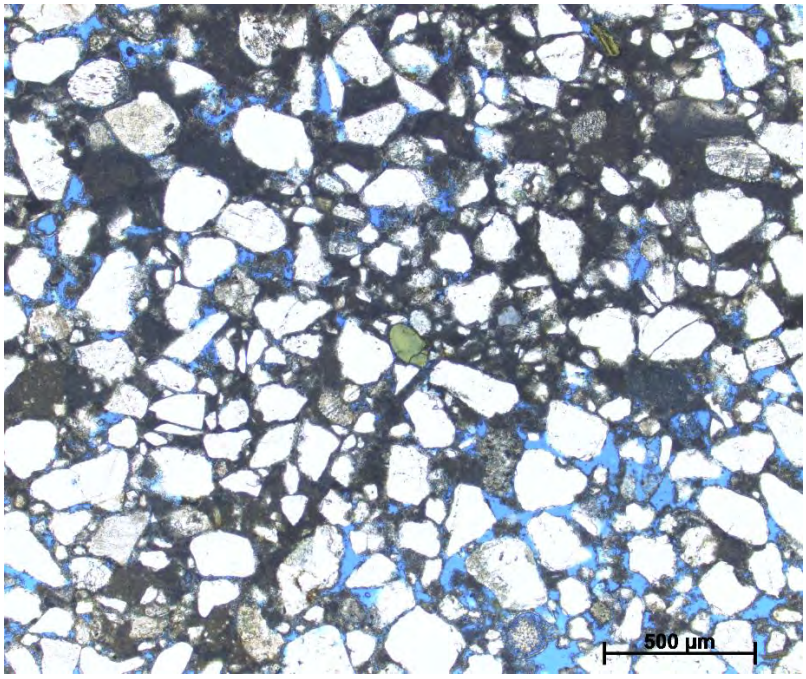

Plate 5. Transmitted light photomicrograph (plain polarised light) showing fine to medium grain-supported sandstone, with angular to sub-angular detrital quartz (clear) and feldspar (cloudy) grains. In the centre is a detrital glauconite grain. Sample GT004.

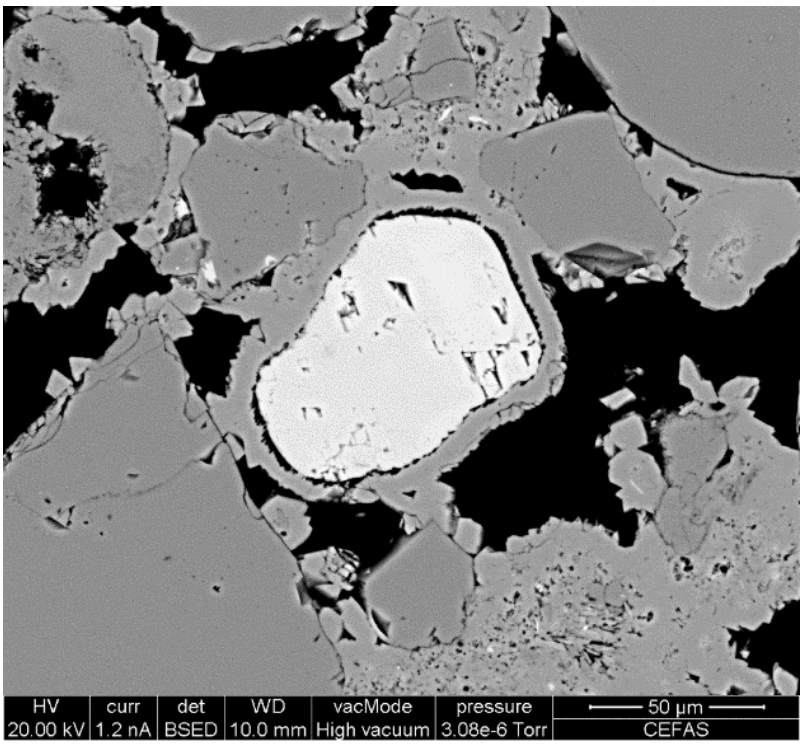

Plate 6. BSEM image showing the globular aggregates of micrite (mid-grey) with microporous cores and the preferential formation of a cement rim around a detrital limestone or calcite grain (centre, white). Sample GT004.

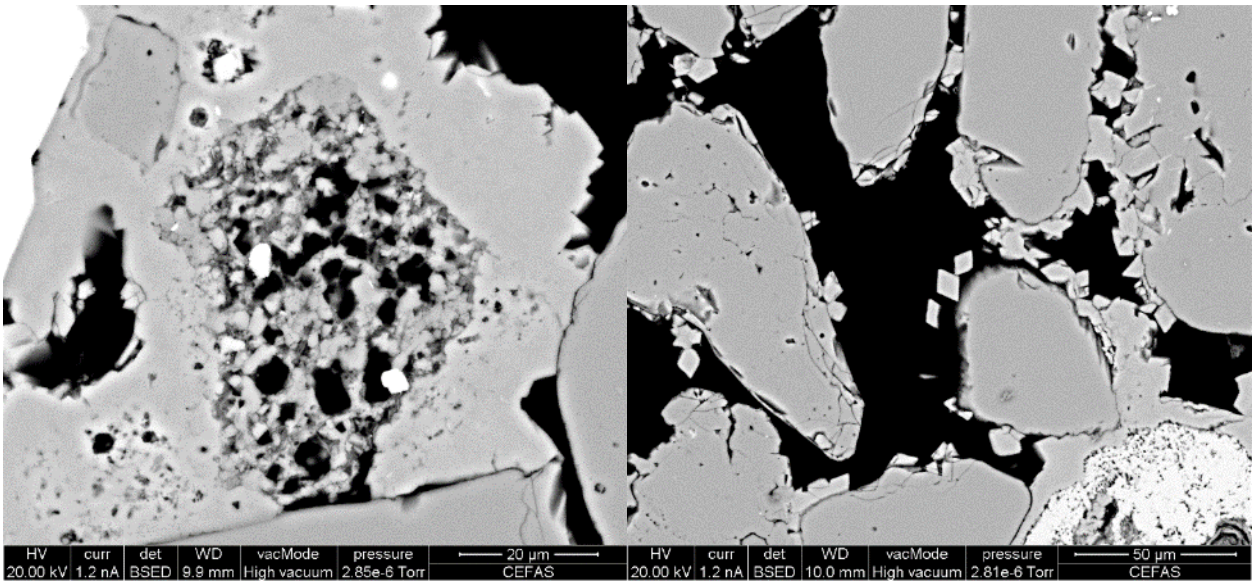

Plate 7. BSEM images of the micritic, high- magnesium cement in sample GT004. The image on the left shows a microporous core (porosity is back) surrounded by a blocky rim, the image on the right shows the development of grain-coating euhedral rhombs of high magnesium calcite.

The idiomorphic rhomb morphology of the microcrystalline micritic to microsparry carbonate cement is very typical of dolomite. ED-EPMA analysis of the carbonate cement is presented in Table 4 and is summarised in Figure 4. The micritic and microsparite cements are very similar in composition, and contain between 39 and 44 mole % $MgCO_3$ in solid-solution (i.e. the structural formula of the calcite can be represented as $Ca_{0.56\text{-}0.61}Mg_{0.44\text{-}0.39}CO_3$). With up to 44 mole % $MgCO_3$ (Table 4, Figure 4) some of these analyses approach calcium-rich dolomite in composition (Reeder, 1983). The composition of some of the micritic carbonate in this sample is very similar to that seen in excess-calcium dolomites (average composition $Ca_{0.53}Mg_{0.47}CO_3$) reported from MDAC deposits in the Kattegat off the coast of Denmark (Jensen et al., 1992), and described previously from the Irish Sea (Milodowski et al., 2009). However, XRD analysis did not identify dolomite as a definite component in this sample but did show that the bulk of the carbonate cement (comprising 22.8 wt % of the sample) produced a diffraction pattern interpreted as very magnesian-calcite (Section 3.1, Table 2).

The sequence of sedimentary and post-depositional diagenetic events recorded from sample GT004 can be summarised as follows:

1. Deposition of sand and silt sediment.
2. Syndepositional bioturbation.
3. Precipitation of micritic high-magnesian calcite within the near-surface of the sediment, causing lithification.
4. Precipitation of framboidal pyrite coeval with, and in close association with, precipitation of high-magnesian calcite under reducing porewater conditions.
5. Minor dissolution of unstable detrital feldspars and some calcareous bioclasts and formation of minor secondary porosity (grain dissolution porosity).
6. Exposure and erosion of the carbonate-cemented sediment, and abrasion of the eroded clasts (forming the pockmarked surface). Exposure and erosion of the carbonate sediment on the seabed may have resulted in oxidation of earlier-formed pyrite and precipitation of secondary iron oxyhydroxide.

7. Minor boring of the clast surfaces by marine biota. In part this may have been coeval with [4], and may be on-going.
8. Formation of calcareous serpulid encrustations on the lithified surface of the clast.

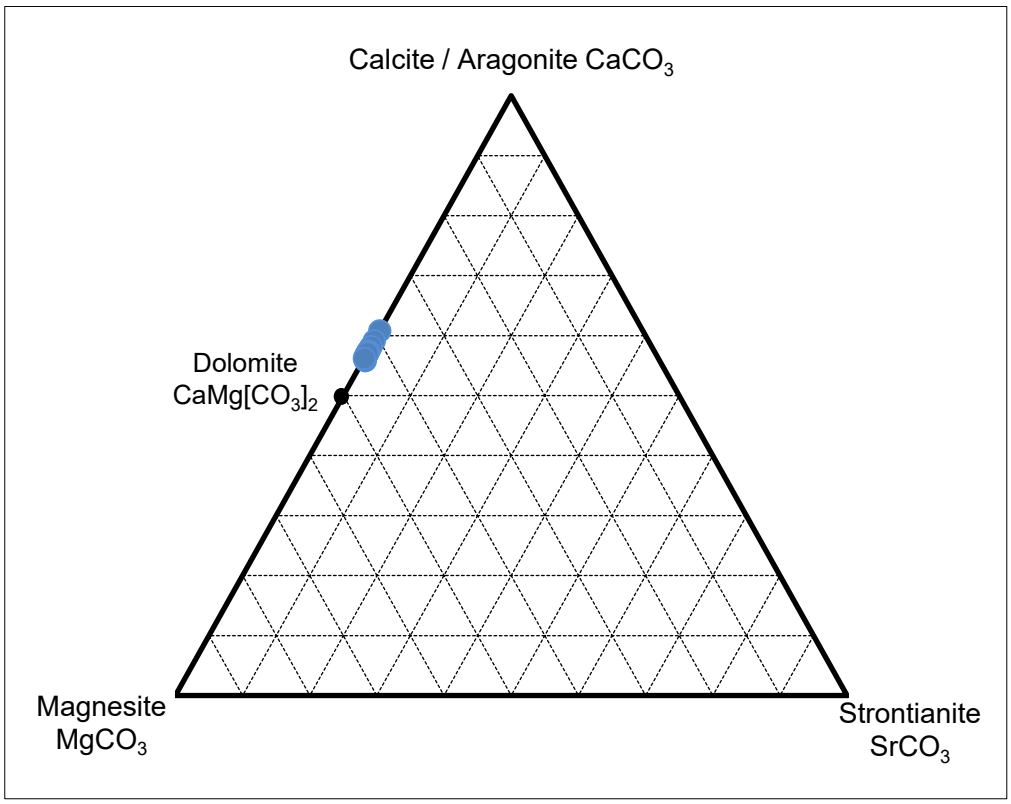

Figure 4. $CaCO_3$-$MgCO_3$-$SrCO_3$ molar ratio plot illustrating the compositions of the micritic high-magnesian calcite cement (solid blue circles) from sample GT004.

Table 4. Electron microprobe analyses of high-magnesian calcite cement from sample GT004

		Weight % oxide (normalised)							Ionic ratio [normalised to 3 [O]						COMMENTS
SAMPLE	No	MgO	CaO	MnO	FeO	SrO	CO_2 (calc)	*Total wt%	Mg^{2+}	Ca^{2+}	Mn^{2+}	Fe^{2+}	Sr^{2+}	CO_3^{2-}	
GT004	1	18.78	34.03	0.00	0.00	0.00	47.19	100	0.43	0.57	0.00	0.00	0.00	1.00	blocky micrite
GT004	2	18.71	34.11	0.00	0.00	0.00	47.18	100	0.43	0.57	0.00	0.00	0.00	1.00	blocky micrite
GT004	3	18.55	34.29	0.00	0.00	0.00	47.16	100	0.43	0.57	0.00	0.00	0.00	1.00	blocky micrite
GT004	4	18.56	34.29	0.00	0.00	0.00	47.16	100	0.43	0.57	0.00	0.00	0.00	1.00	blocky micrite
GT004	5	18.35	34.26	0.00	0.29	0.00	47.09	100	0.43	0.57	0.00	0.00	0.00	1.00	blocky micrite
GT004	6	18.44	34.14	0.00	0.31	0.00	47.11	100	0.43	0.57	0.00	0.00	0.00	1.00	blocky micrite
GT004	7	18.65	34.18	0.00	0.00	0.00	47.17	100	0.43	0.57	0.00	0.00	0.00	1.00	blocky micrite
GT004	8	18.89	33.89	0.00	0.00	0.00	47.21	100	0.44	0.56	0.00	0.00	0.00	1.00	blocky micrite
GT004	9	18.71	34.11	0.00	0.00	0.00	47.18	100	0.43	0.57	0.00	0.00	0.00	1.00	blocky micrite
GT004	10	18.18	34.72	0.00	0.00	0.00	47.09	100	0.42	0.58	0.00	0.00	0.00	1.00	blocky micrite
GT004	11	16.81	36.33	0.00	0.00	0.00	46.86	100	0.39	0.61	0.00	0.00	0.00	1.00	blocky micrite
GT004	12	17.58	35.44	0.00	0.00	0.00	46.99	100	0.41	0.59	0.00	0.00	0.00	1.00	blocky micrite
GT004	13	18.71	34.10	0.00	0.00	0.00	47.18	100	0.43	0.57	0.00	0.00	0.00	1.00	blocky rim micrite
GT004	14	18.92	33.58	0.00	0.00	0.36	47.15	100	0.44	0.56	0.00	0.00	0.00	1.00	blocky rim micrite
GT004	15	18.55	34.30	0.00	0.00	0.00	47.15	100	0.43	0.57	0.00	0.00	0.00	1.00	blocky rim micrite
GT004	16	18.46	34.40	0.00	0.00	0.00	47.14	100	0.43	0.57	0.00	0.00	0.00	1.00	blocky rim micrite
GT004	17	18.72	34.10	0.00	0.00	0.00	47.18	100	0.43	0.57	0.00	0.00	0.00	1.00	blocky rim micrite
GT004	18	18.63	34.20	0.00	0.00	0.00	47.17	100	0.43	0.57	0.00	0.00	0.00	1.00	blocky rim micrite
GT004	19	18.00	34.94	0.00	0.00	0.00	47.06	100	0.42	0.58	0.00	0.00	0.00	1.00	blocky rim micrite
GT004	20	18.35	34.52	0.00	0.00	0.00	47.12	100	0.43	0.57	0.00	0.00	0.00	1.00	blocky rim micrite
GT004	21	18.38	34.49	0.00	0.00	0.00	47.13	100	0.43	0.57	0.00	0.00	0.00	1.00	blocky rim micrite
GT004	22	18.42	34.45	0.00	0.00	0.00	47.13	100	0.43	0.57	0.00	0.00	0.00	1.00	blocky rim micrite
GT004	23	18.65	34.18	0.00	0.00	0.00	47.17	100	0.43	0.57	0.00	0.00	0.00	1.00	blocky rim micrite
GT004	24	18.59	34.25	0.00	0.00	0.00	47.16	100	0.43	0.57	0.00	0.00	0.00	1.00	blocky rim micrite
GT004	25	18.57	34.08	0.00	0.21	0.00	47.14	100	0.43	0.57	0.00	0.00	0.00	1.00	blocky rim micrite
GT004	26	18.50	34.36	0.00	0.00	0.00	47.15	100	0.43	0.57	0.00	0.00	0.00	1.00	blocky rim micrite
GT004	27	18.93	33.85	0.00	0.00	0.00	47.22	100	0.44	0.56	0.00	0.00	0.00	1.00	blocky rim micrite

**Note: Some analytical totals were low (<90%) because of the microporous nature of the cements. Therefore all data were normalised to 100%*

4.2 SAMPLE GT005

This sample comprised a number of sub-angular to sub-rounded, tabular mid-brown, carbonate-cemented sandstone clasts ranging from approximately 40 to 110 mm diameter (Plate 8). The clasts are stained and coated by very fine grained, pale, orange-brown, iron-oxyhydroxide (Plate 8).

The polished thin section was prepared from one of the clasts, and a scanned image is shown in Plate 9. In general, the sandstone is friable and only weakly cemented. Very thin (<1 mm), horizontal laminae of mid to dark brown, iron oxyhydroxide-stained cemented sandstone are visible in this scan, contrasting with thicker (2-5 mm) bands of less-well cemented sandstone. Although the way-up of the sample is unknown, it is probable that these laminae reflect the depositional bedding fabric of the sandstone. Some of the thicker, porous bands of sand are lenticular in cross section, indicative of ripple-lamination (Plate 9).

Detrital sand grains are sub-angular to sub-rounded (<400 µm), and dominated by detrital quartz. The sandstone fabric is grain-supported, and the grains show little evidence of compaction: with an open-packed grain framework, and grain contacts being simple point- or long-edge contacts. Shell fragments are more numerous than GT004 but are still a minor component. However, numerous detrital shell fragments have been cemented onto the surfaces of the clasts, and minor bryozoan encrustations on the surfaces are also present. Intergranular porosity in the less-well cemented sandstone is often oversized (Plate 10), which indicates the dissolution of unstable framework detrital grains or calcareous bioclasts (cf. Schmidt and McDonald, 1979).

The matrix of the well-cemented sandstone layers is a micritic high magnesian calcite. XRD analysis indicates that very high magnesian calcite comprises the bulk of the carbonate present in the sample (Table 2). This was sometimes observed in thin section to form globular aggregates enclosing clay-rich cores (Plate 11). Microsparry calcite cement can also sometimes be seen to enclose small spherical cavities less than 10 um diameter. Blocky, subidiomorphic to idiomorphic rhombic calcite crystals also form thin rims around grains, lining the intergranular pore space and forming a weak cement in the porous sand layers

Plate 8. Photograph showing sample GT005. This sample comprises a number of sub-angular to sub-rounded clasts from 40 – 110 mm. Detrital shell fragments and minor bryozoan encrustations can be seen on the surfaces. Field of view ~250 mm wide.

Plate 9. Scan of sample GT005 thin section. Horizontal discontinuous laminae of mid-dark brown cemented sand separate very porous lenticular layers of sand Field of view = 48 mm wide.

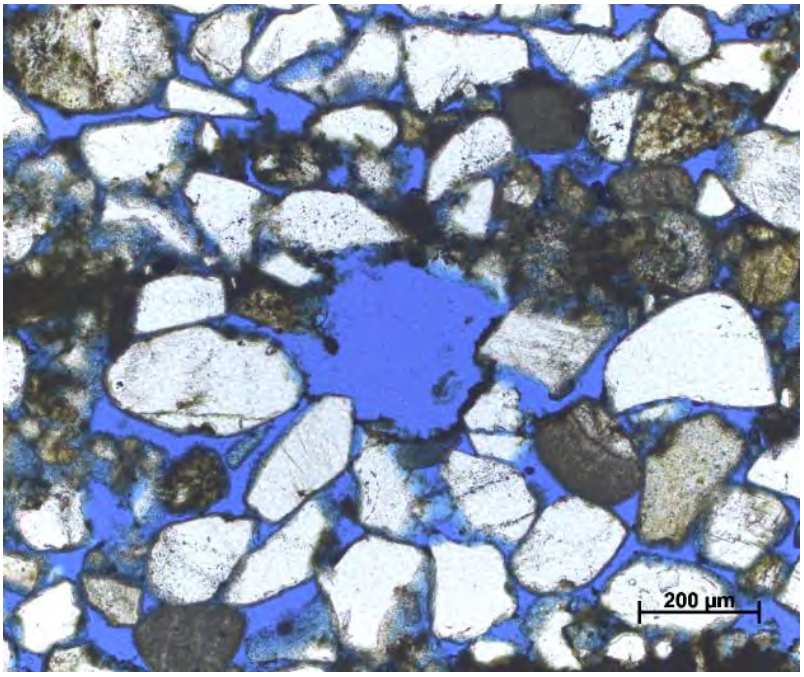

Plate 10. Transmitted light photomicrograph (plain polarised light) showing grain-supported medium sandstone with a cemented band (darker, centre-horizontal) within sparsely sandstone. A secondary, oversized pore (blue) can be seen in the centre of the image and represents a detrital grain dissolution site. The micritic cement is mid-dark brown and forms globular aggregates or clots. Sample GT005.

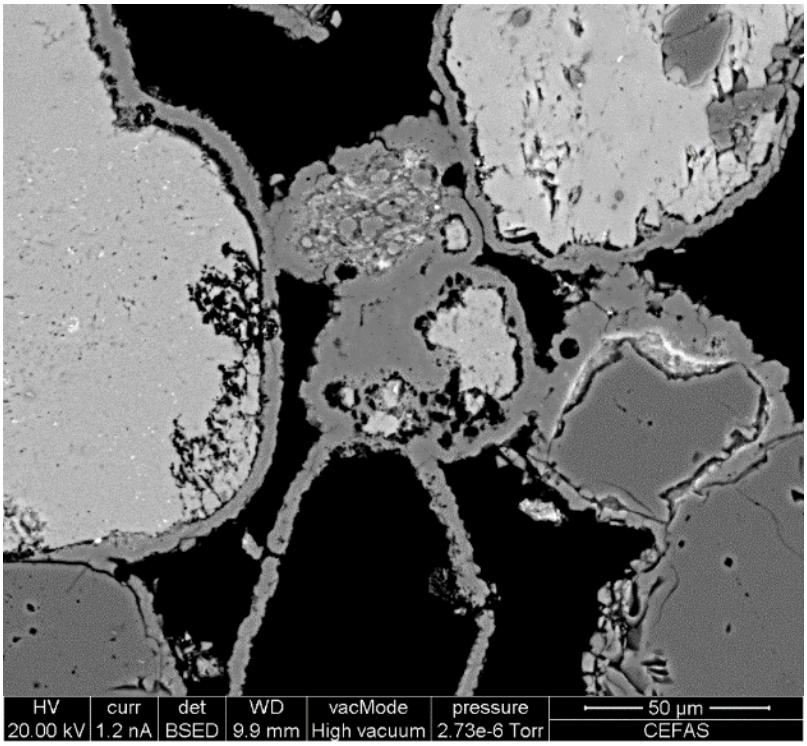

Plate 11. BSEM image showing the thin micrite rims around the grains, lining the intergranular pore space. The globular clots of micrite contain clay-rich cores. Sample GT005.

ED-EPMA analysis of the carbonate cements are presented in Table 5 and are summarised in Figure 5. The micritic magnesian calcite cements contain between 30 and 43 mole % $MgCO_3$ in

solid solution (i.e. the structural formula of the calcite can be represented as $Ca_{0.57-0.70}Mg_{0.43-0.30}CO_3$). This composition is consistent with the XRD analysis (Table 2), which showed that very high magnesian calcite represents the bulk of the carbonate present (13.1% of the rock).

The sequence of sedimentary and post-depositional diagenetic events recorded from sample GT005 can be summarised as follows:

1. Deposition of ripple-laminated sand and fine muddy sediment.
2. Precipitation of micritic high-magnesian calcite causing lithification.
3. Minor dissolution of unstable detrital grains and bioclast framework grains, producing some secondary porosity. This may coeval with the formation of the magnesian calcite precipitation.
4. Minor oxidation of reduced iron phases on the clast surfaces, and within the cement, associated with staining by secondary iron oxyhydroxide.
5. Minor colonisation of bryozoans Some detrital shell fragments appear to have been cemented onto the surface of the clast at this stage, which may indicate some continuing carbonate cementation.

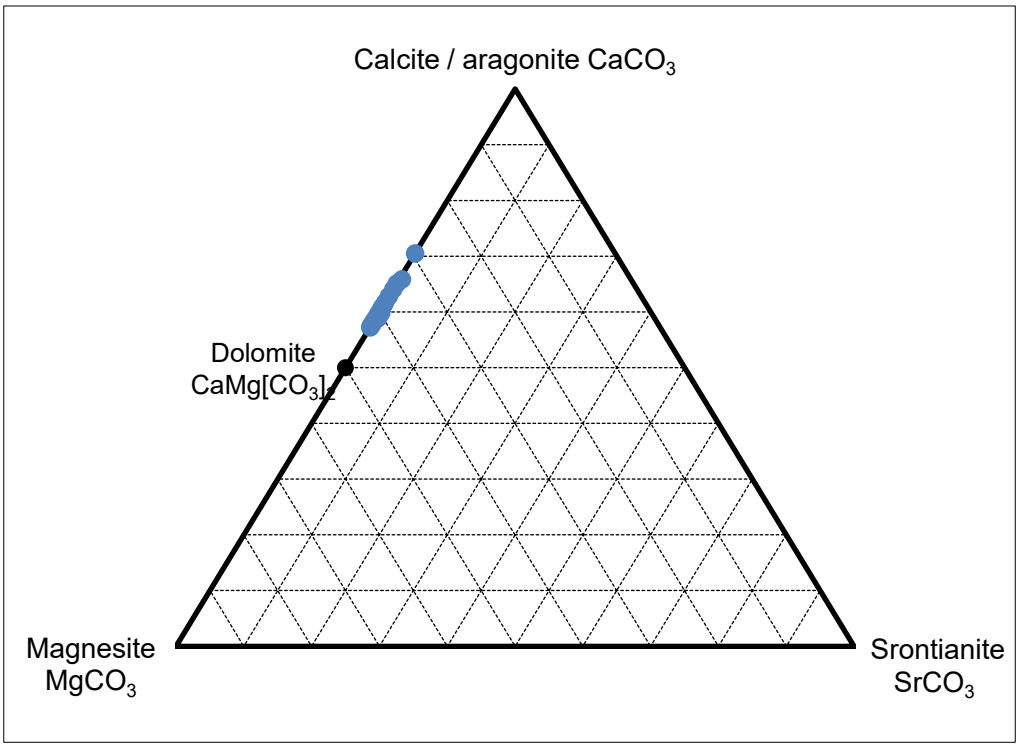

Figure 5. $CaCO_3$-$MgCO_3$-$SrCO_3$ molar ratio plot illustrating the compositions of the micritic high-magnesian calcite cement (solid blue circles) from sample GT005.

Table 5. Electron microprobe analysis of carbonate cements in sample GT005

		Weight % oxide (normalised)							Ionic ratio [normalised to 3 [O]						COMMENTS
SAMPLE	No	MgO	CaO	MnO	FeO	SrO	CO_2 (calc)	*Total wt%	Mg^{2+}	Ca^{2+}	Mn^{2+}	Fe^{2+}	Sr^{2+}	CO_3^{2-}	
GT005	1	12.46	41.43	0.00	0.00	0.00	46.11	100	0.30	0.70	0.00	0.00	0.00	1.00	blocky rim micrite
GT005	2	18.47	34.39	0.00	0.00	0.00	47.14	100	0.43	0.57	0.00	0.00	0.00	1.00	blocky rim micrite
GT005	3	18.27	34.62	0.00	0.00	0.00	47.11	100	0.42	0.58	0.00	0.00	0.00	1.00	blocky rim micrite
GT005	4	18.40	34.47	0.00	0.00	0.00	47.13	100	0.43	0.57	0.00	0.00	0.00	1.00	blocky rim micrite
GT005	5	17.96	34.98	0.00	0.00	0.00	47.05	100	0.42	0.58	0.00	0.00	0.00	1.00	blocky rim micrite
GT005	6	17.10	35.71	0.00	0.00	0.35	46.84	100	0.40	0.60	0.00	0.00	0.00	1.00	blocky rim micrite
GT005	7	18.06	34.56	0.00	0.34	0.00	47.04	100	0.42	0.58	0.00	0.00	0.00	1.00	blocky rim micrite
GT005	8	18.04	34.90	0.00	0.00	0.00	47.07	100	0.42	0.58	0.00	0.00	0.00	1.00	blocky rim micrite
GT005	9	17.77	34.96	0.00	0.28	0.00	46.99	100	0.41	0.58	0.00	0.00	0.00	1.00	blocky rim micrite
GT005	10	17.68	35.31	0.00	0.00	0.00	47.01	100	0.41	0.59	0.00	0.00	0.00	1.00	blocky rim micrite
GT005	11	17.51	35.21	0.00	0.00	0.38	46.90	100	0.41	0.59	0.00	0.00	0.00	1.00	blocky rim micrite
GT005	12	16.71	36.10	0.00	0.39	0.00	46.80	100	0.39	0.61	0.00	0.01	0.00	1.00	blocky rim micrite
GT005	13	15.85	37.19	0.00	0.29	0.00	46.66	100	0.37	0.63	0.00	0.00	0.00	1.00	blocky rim micrite
GT005	14	16.84	36.29	0.00	0.00	0.00	46.86	100	0.39	0.61	0.00	0.00	0.00	1.00	blocky rim micrite
GT005	15	17.41	35.64	0.00	0.00	0.00	46.96	100	0.40	0.60	0.00	0.00	0.00	1.00	blocky rim micrite
GT005	16	17.27	35.79	0.00	0.00	0.00	46.94	100	0.40	0.60	0.00	0.00	0.00	1.00	blocky rim micrite
GT005	17	14.10	38.25	0.00	1.01	0.44	46.20	100	0.33	0.65	0.00	0.01	0.00	1.00	blocky rim micrite
GT005	18	16.77	36.01	0.00	0.41	0.00	46.81	100	0.39	0.60	0.00	0.01	0.00	1.00	blocky rim micrite
GT005	19	16.55	35.95	0.00	0.75	0.00	46.74	100	0.39	0.60	0.00	0.01	0.00	1.00	blocky rim micrite
GT005	20	16.93	35.94	0.00	0.27	0.00	46.85	100	0.39	0.60	0.00	0.00	0.00	1.00	blocky rim micrite
GT005	21	16.36	36.55	0.00	0.35	0.00	46.74	100	0.38	0.61	0.00	0.00	0.00	1.00	blocky rim micrite
GT005	22	14.71	38.23	0.00	0.62	0.00	46.44	100	0.35	0.65	0.00	0.01	0.00	1.00	blocky rim micrite
GT005	23	15.24	37.80	0.00	0.42	0.00	46.55	100	0.36	0.64	0.00	0.01	0.00	1.00	blocky rim micrite

**Note: Some analytical totals were low (<90%) because of the microporous nature of the cements. Therefore all data were normalised to 100%*

4.3 SAMPLE GT007

This sample comprised a single, sub-angular tabular clast (<70 mm) in diameter, and is a light-grey, medium-grained carbonate-cemented sandstone (Plate 12). The surface displayed some minor, light orange-brown, iron oxyhydroxide staining. Some burrows, infilled with fine-grained muddy sediment were clearly visible on the surface.

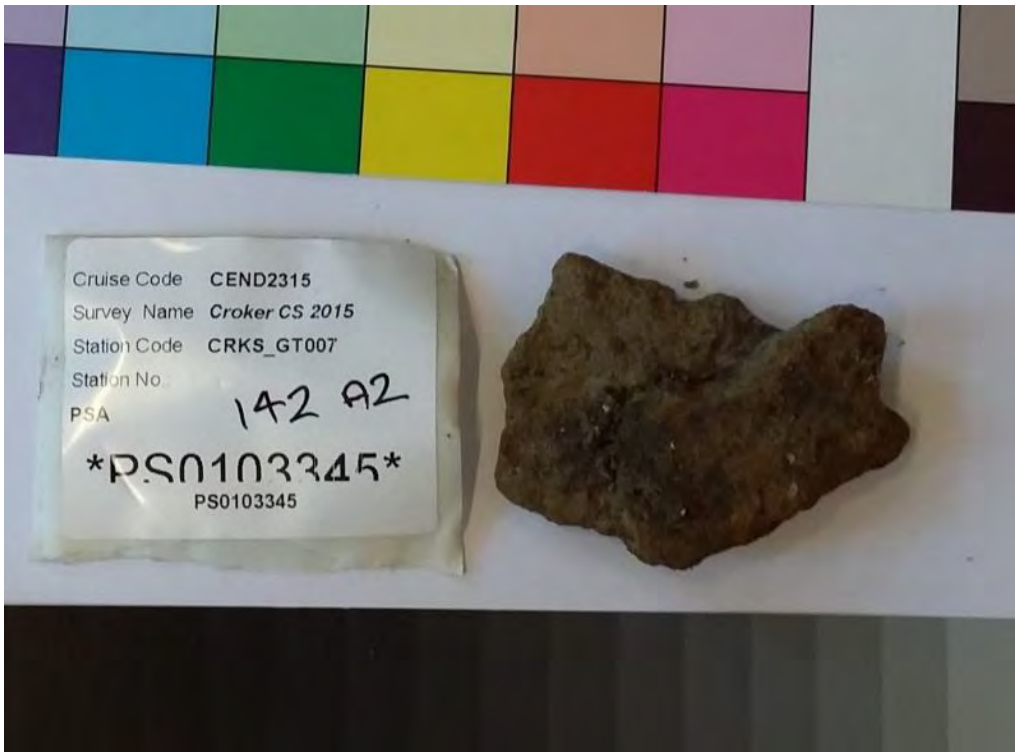

Plate 12. Photograph of sample GT007. This is a single, sub-angular clast (<70 mm) in diameter. Field of view ~150 mm wide.

The polished thin section prepared through the GT007 clast is shown in Plate 13. The sample is predominantly fine to medium sandstone, with a brown patchy siltstone and micrite matrix. It has a patchy, brown colouration, predominantly towards the margins of the plate, where the carbonate cement, silt matrix and grain surfaces have been stained by brown iron oxyhydroxide. Numerous cross- and longitudinal-sections of burrows are visible, the majority of which have been infilled by a dark, fine-grained muddy sediment.

The sandstone has an uncompacted, largely grain-supported fabric, comprising angular to sub-angular detrital grains which are in simple point contact with each other. The sample is dominated by detrital quartz, with subordinate feldspars and lithic fragments (including some limestone clasts). Bioclastic debris is relatively uncommon. Rare, rounded, detrital glauconite ("glauconie" *sensu lato*) grains are present. Evidence of minor secondary framework grain dissolution pore space was observed, resulting from the dissolution of unstable detrital silicactes and some shell fragments.

XRD analysis shows that very high magnesian calcite is the major carbonate mineral present (Table 2). High resolution BSEM imaging shows that it mainly as the intergranular matrix of the sandstone, occurring as "clots" of aggregated very fine micritic magnesian calcite particles (Plate 14). In addition, coarser, blocky rims of denser subidiomorphic microcrystalline calcite rhombs have preferentially formed around rare detrital limestone grains, which appear to have acted as a localised nucleation points. The micritic matrix cement becomes more microporous towards the centre of intergranular regions.

The micrite matrix also contains aggregates of calcite microcrystals forming small clots enclosing small spherical voids (Plate 15) These cavities are of the order of 1 to 2 µm in size, which is about the size expected for bacterial cells (cf. Konhauser 2007), These well-developed cellular microfabrics resemble fossilised and mineralised bacterial cells described from experimental studies and other environments in the literature (c.f. Martill and Wilby, 1994; Wilby and Whyte, 1995). The cavities observed in this micritic cement may therefore similarly represent bacterial cells around which the micritic carbonate may have nucleated (similar features were also observed in sample GT004). Some of the larger voids observed in this sandstone could potentially be former gas bubbles that were trapped and preserved in the micritic cement.

Some cemented areas are rich in fine-grained clay, which in places displays a pelloidal fabric, possibly representing localised concentrations of faecal pellets (Plate 16). The clay-rich patches contain numerous spherical iron oxyhydroxides (<5 µm) that may represent pseudomorphs after oxidised framboidal pyrite.

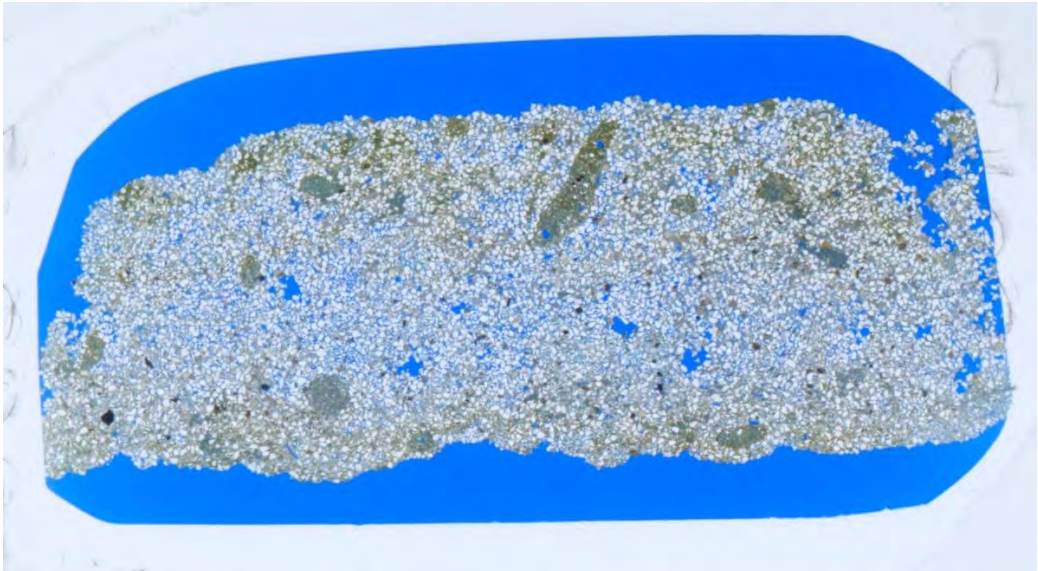

Plate 13. Scan of sample GT007 polished thin section from sample GT007. Numerous infilled burrows are visible. The outer surfaces of the clast show a brown colouration associated with finely disseminated Fe-oxyhydroxide. Field of view = 48 mm wide.

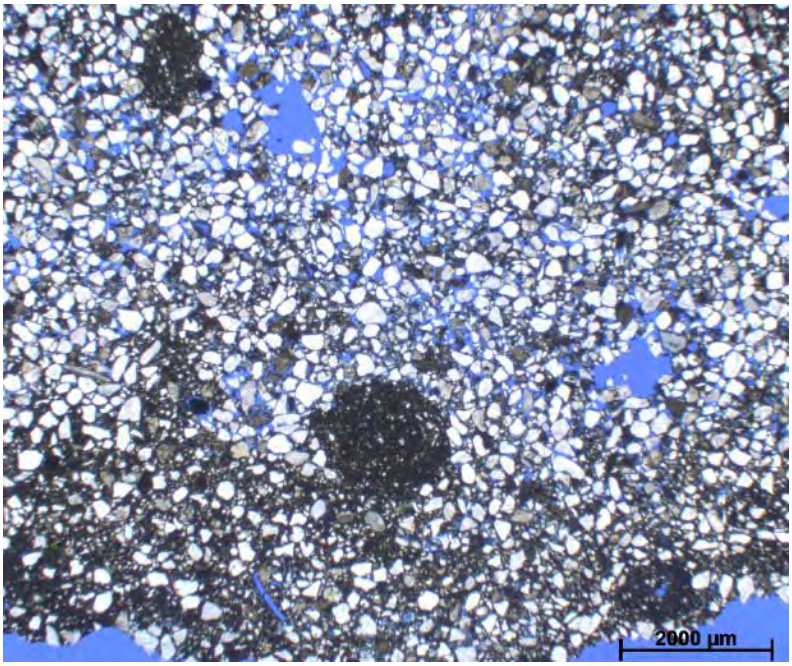

Plate 14. Transmitted light photomicrograph (plain polarised light) of fine to medium-grained sandstone showing cross-sections through three burrows infilled with a dark-brown, fine-grained silt and clay. Cementation is patchy, and there are some oversized pore spaces present (blue-dye resin-impregnated). Sample GT007.

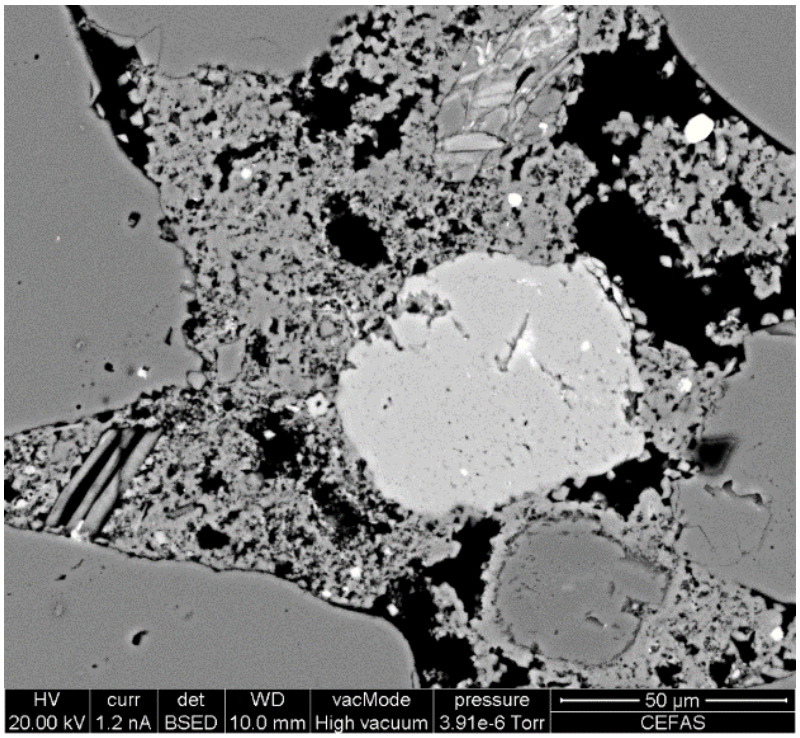

Plate 15. BSEM image showing the microporous nature of the micritic magnesian calcite cement, and the local development of coarser blocky rims around some grains. Sample GT007.

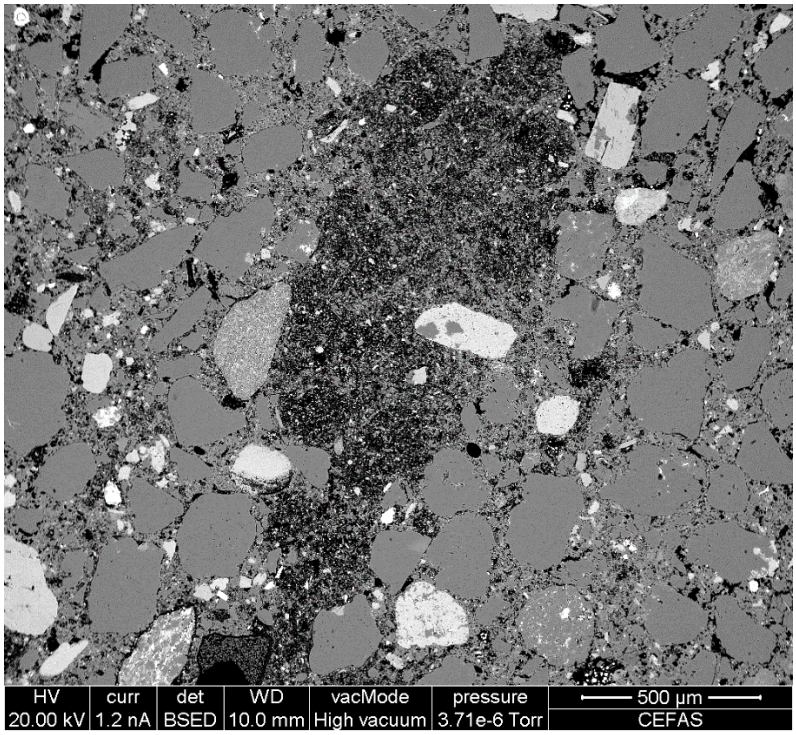

Plate 16. BSEM image showing a clay-rich area (dark, centre) which has a pelloidal fabric. This probably represents a cluster of relic faecal pellets. Sample GT007.

ED-EPMA analysis of the carbonate cements are presented in Figure 6 and are summarised in Table 6. The micritic magnesian calcite cements are very similar in composition and contain between 32 and 43 mole % $MgCO_3$ in solid solution within the crystal lattice (i.e. the structural formula of the calcite can be represented as $Ca_{0.57\text{-}0.68}Mg_{0.43\text{-}0.32}CO_3$).

Shell fragments are composed of pure calcite, plotting at the apex of the triplot diagram (Figure 6).

The sequence of sedimentary and post-depositional diagenetic events recorded from sample GT007 can be summarised as follows:

1. Deposition of fine to medium sand sediment, and fine-grained clay material (including faecal pellets).
2. Syndepositional bioturbation.
3. Minor pyrite formation under reducing porewater conditions
4. Precipitation of micritic high-magnesian calcite within the near-surface of the sediment, causing lithification. This may have been coeval with [2].
5. Minor oxidation of early digenetic pyrite and other reduced iron phases within the carbonate cemented sediment.

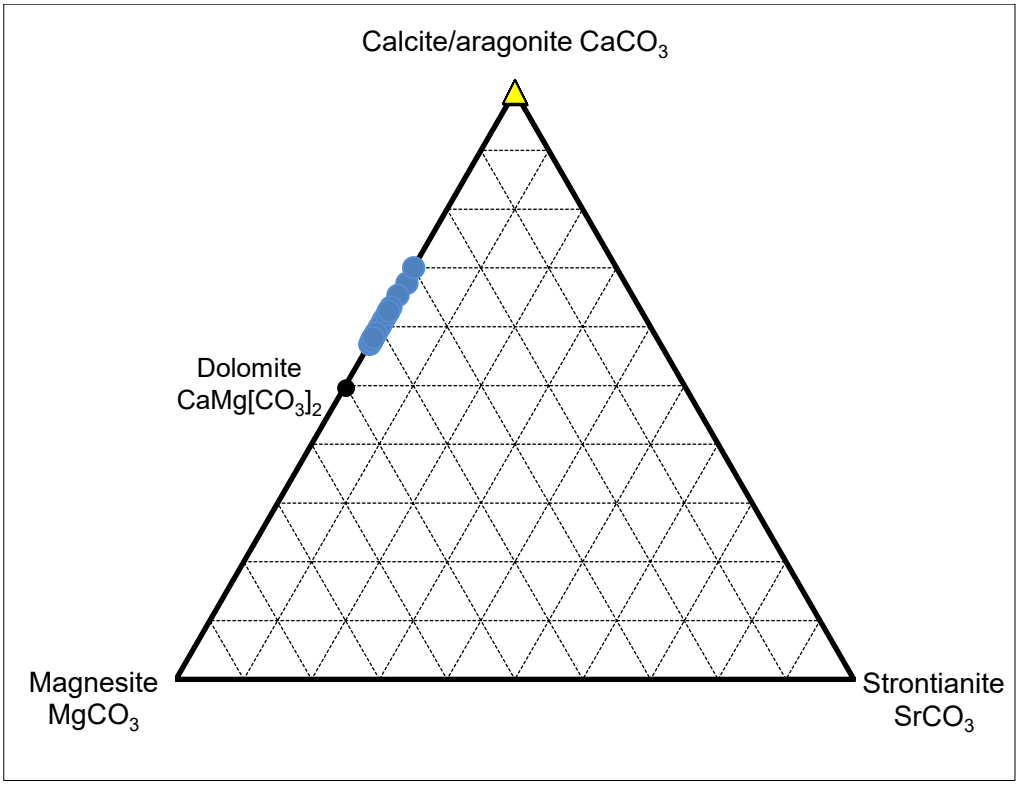

Figure 6. $CaCO_3$-$MgCO_3$-$SrCO_3$ molar ratio plot illustrating the compositions of the high-magnesian calcite micritic cement (solid blue circles), and detrital shell fragments (yellow triangles) from sample GT007.

Table 6. Electron microprobe analyses of carbonate cements and detrital shell fragments in sample GT007.

		Weight % oxide (normalised)							Ionic ratio [normalised to 3 [O]						COMMENTS
SAMPLE	No	MgO	CaO	MnO	FeO	SrO	CO_2 (calc)	*Total wt%	Mg^{2+}	Ca^{2+}	Mn^{2+}	Fe^{2+}	Sr^{2+}	CO_3^{2-}	
GT007	1	0.00	56.04	0.00	0.00	0.00	43.96	100	0.00	1.00	0.00	0.00	0.00	1.00	shell
GT007	2	0.00	56.04	0.00	0.00	0.00	43.96	100	0.00	1.00	0.00	0.00	0.00	1.00	shell
GT007	3	0.00	56.04	0.00	0.00	0.00	43.96	100	0.00	1.00	0.00	0.00	0.00	1.00	shell
GT007	4	0.00	56.04	0.00	0.00	0.00	43.96	100	0.00	1.00	0.00	0.00	0.00	1.00	shell
GT007	5	0.00	56.04	0.00	0.00	0.00	43.96	100	0.00	1.00	0.00	0.00	0.00	1.00	shell
GT007	6	0.00	55.79	0.00	0.00	0.30	43.90	100	0.00	1.00	0.00	0.00	0.00	1.00	shell
GT007	7	0.00	56.04	0.00	0.00	0.00	43.96	100	0.00	1.00	0.00	0.00	0.00	1.00	shell
GT007	8	0.00	56.04	0.00	0.00	0.00	43.96	100	0.00	1.00	0.00	0.00	0.00	1.00	shell
GT007	9	16.55	36.45	0.00	0.21	0.00	46.79	100	0.39	0.61	0.00	0.00	0.00	1.00	micrite
GT007	10	18.09	34.62	0.00	0.24	0.00	47.05	100	0.42	0.58	0.00	0.00	0.00	1.00	micrite
GT007	12	18.48	34.19	0.00	0.20	0.00	47.12	100	0.43	0.57	0.00	0.00	0.00	1.00	micrite
GT007	13	13.61	39.62	0.22	0.00	0.34	46.22	100	0.32	0.67	0.00	0.00	0.00	1.00	micrite
GT007	14	18.18	34.73	0.00	0.00	0.00	47.09	100	0.42	0.58	0.00	0.00	0.00	1.00	micrite
GT007	15	17.95	33.85	0.00	1.27	0.00	46.93	100	0.42	0.57	0.00	0.02	0.00	1.00	micrite
GT007	16	16.74	36.41	0.00	0.00	0.00	46.84	100	0.39	0.61	0.00	0.00	0.00	1.00	micrite
GT007	17	17.91	35.04	0.00	0.00	0.00	47.05	100	0.42	0.58	0.00	0.00	0.00	1.00	micrite
GT007	18	15.93	37.36	0.00	0.00	0.00	46.71	100	0.37	0.63	0.00	0.00	0.00	1.00	micrite
GT007	19	12.66	41.20	0.00	0.00	0.00	46.14	100	0.30	0.70	0.00	0.00	0.00	1.00	micrite
GT007	20	14.74	38.76	0.00	0.00	0.00	46.50	100	0.35	0.65	0.00	0.00	0.00	1.00	micrite
GT007	21	16.01	37.28	0.00	0.00	0.00	46.72	100	0.37	0.63	0.00	0.00	0.00	1.00	micrite
GT007	22	17.26	35.81	0.00	0.00	0.00	46.93	100	0.40	0.60	0.00	0.00	0.00	1.00	micrite
GT007	23	18.12	34.80	0.00	0.00	0.00	47.08	100	0.42	0.58	0.00	0.00	0.00	1.00	micrite
GT007	24	18.13	34.79	0.00	0.00	0.00	47.08	100	0.42	0.58	0.00	0.00	0.00	1.00	micrite
GT007	25	18.31	34.58	0.00	0.00	0.00	47.11	100	0.42	0.58	0.00	0.00	0.00	1.00	micrite
GT007	26	15.60	37.53	0.00	0.25	0.00	46.62	100	0.37	0.63	0.00	0.00	0.00	1.00	micrite
GT007	28	17.07	36.03	0.00	0.00	0.00	46.90	100	0.40	0.60	0.00	0.00	0.00	1.00	micrite
GT007	29	16.25	36.99	0.00	0.00	0.00	46.76	100	0.38	0.62	0.00	0.00	0.00	1.00	micrite
GT007	30	17.65	35.35	0.00	0.00	0.00	47.00	100	0.41	0.59	0.00	0.00	0.00	1.00	micrite
GT007	31	17.67	35.32	0.00	0.00	0.00	47.00	100	0.41	0.59	0.00	0.00	0.00	1.00	micrite
GT007	32	15.85	37.09	0.00	0.41	0.00	46.65	100	0.37	0.62	0.00	0.01	0.00	1.00	micrite
GT007	33	17.89	34.63	0.00	0.48	0.00	47.00	100	0.42	0.58	0.00	0.01	0.00	1.00	micrite

**Note: Some analytical totals were low (<90%) because of the microporous nature of the cements. Therefore all data were normalised to 100%*

4.4 SAMPLE GT009

Sample GT009 comprised eight tabular, angular clasts of light grey fine-to medium, and coarse grained sandstone, and siltstone. Most clasts have some freshly broken edges (Plate 17). The more weathered edges have been rounded off. Some clasts are pervasively stained orange-brown by iron oxyhydroxide. In other cases, the staining is confined within horizontal bands in the centre of the tabular clasts. The surfaces have evidence of numerous burrows, and calcareous serpulid worm and bryozoan encrustations (e.g. Plate 18).

Plate 17. Photographs of sample GT009. Left: the angular clasts (up to 90 mm diameter). Field of view ~180 mm wide. Right: the fresh internal surfaces showing orange-brown staining from iron-oxyhydroxide. Field of view ~250 mm wide.

Plate 18. Photograph of an encrusting bryozoan on sample GT009 which populate the clasts after lithification.

The polished thin section prepared through one of the GT009 clasts is shown in Plate 19. The sample comprises fine- to medium grained, strongly bioturbated sandstone with a very fine-grained dark brown micritic to microsparite matrix cement. It has a patchy orange-brown colouration, distributed in broadly horizontal bands, where the cement and grain surfaces have been stained by brown iron oxyhydroxide. This staining is probably picking out a weak sedimentary bedding fabric. In thin section the sample appears more tightly packed than the previous samples described above, with a grain-supported fabric dominated by long-grain contacts rather than simple point-contacts (Plate 20). Detrital grains are angular to sub-angular, predominantly medium-grained (<400 µm) quartz with subordinate feldspars. Minor detrital glauconite ("glauconie" *sensu lato*) grains, some of which are badly corroded, are also present. Bioclastic detritus is extremely sparse within this sample. This sample is well-cemented, with very little secondary framework grain dissolution porosity. Burrows infills are dominated by, illitic clay and silica-rich silty sediment containing little sand-grade detrital quartz.

BSEM observations clearly show the extent of the iron oxidation (Plate 21), and how the iron oxyhydroxides are locally concentrated in some areas of the cement. The distribution of this oxidative alteration appears to follow a patchy, heterogeneous fabric that may be influenced by bioturbation fabrics (e.g. burrows) (Plate 19). High-resolution BSEM observations also show that the micritic high-magnesian calcite cement comprises idiomorphic rhombic calcite microcrystals (Plate 22). In general, the micritic, or microsparite calcite are relatively evenly dispersed within the intergranular pore spaces, rather than occurring as the globular aggregates seen in many of the other samples. Sometimes the microsparite cement has precipitated as thin rims nucleated preferentially around minor detrital calcite or limestone grains. The microcellular textures observed in other samples (e.g. GT004 and GT112) were not observed in this sample. Clay and silica-rich material is present within the micrite, although this is not evenly distributed.

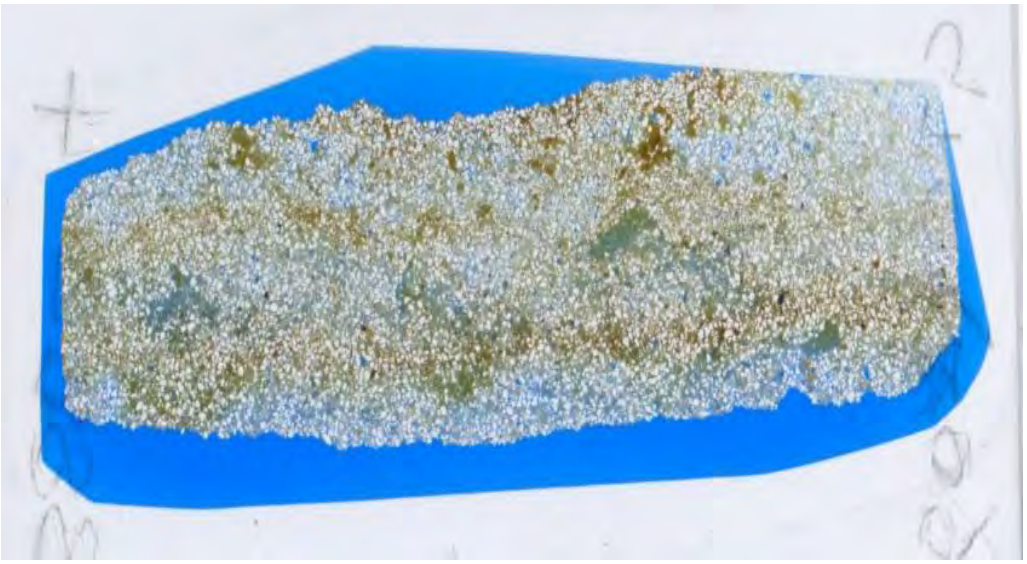

Plate 19. Scanned image of the thin section prepared from one of the clasts of sample GT009. Patchy orange-brown staining due to the presence of iron oxyhydroxides is clearly visible. Field of view = 48 mm wide.

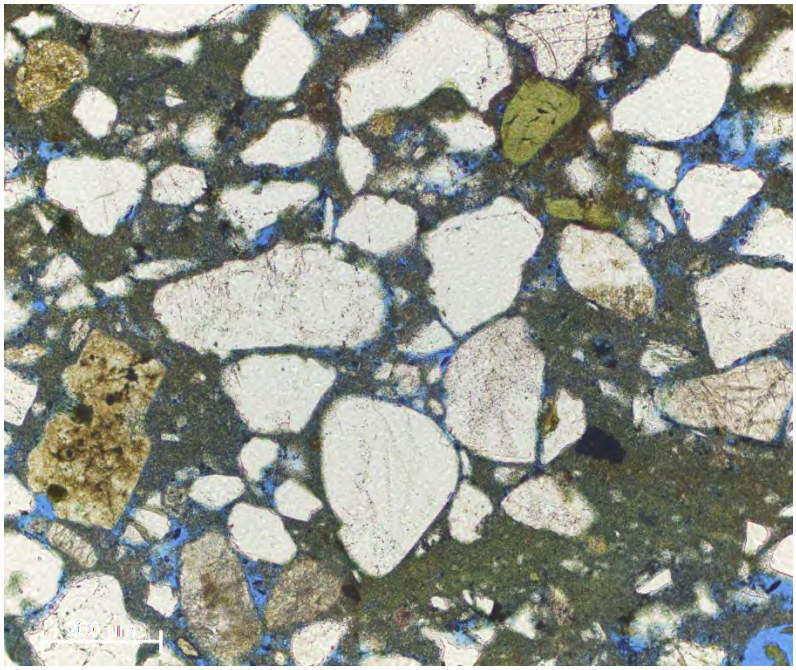

Plate 20. Transmitted light photomicrograph (plain polarised light) showing the close-packed grain-supported fabric with common long-grain contacts. The micritic magnesian calcite matrix is dark brown in colour. Sample GT009

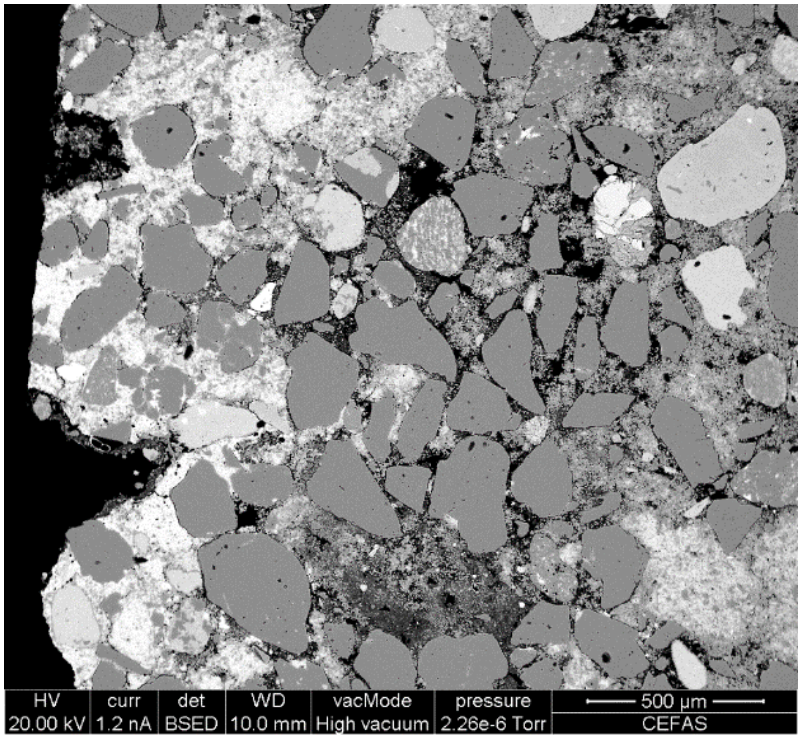

Plate 21. BSEM image showing an area with concentrated iron oxyhydroxides (bright white) dispersed throughout the micritic cement. Sample GT009

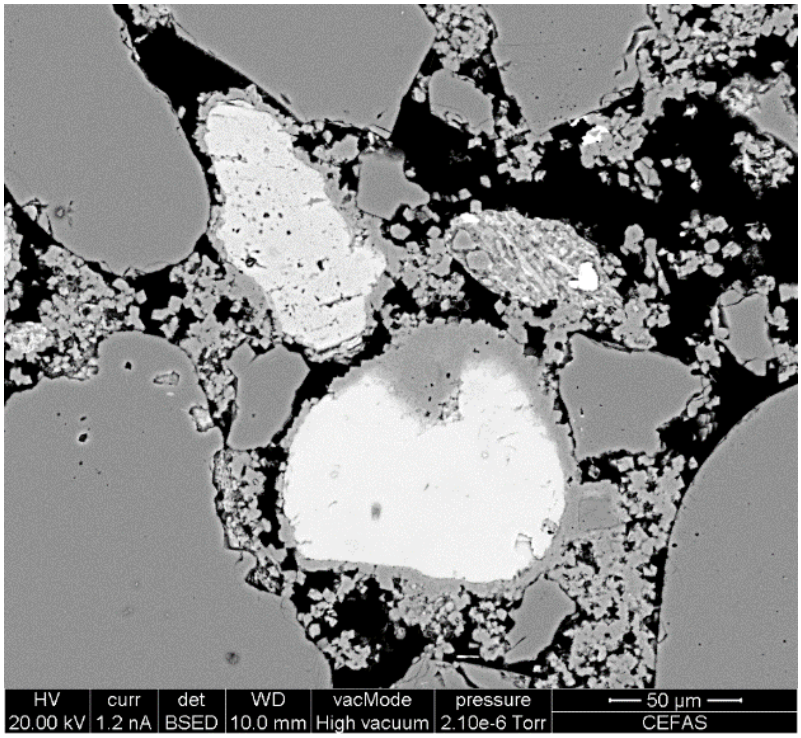

Plate 22. BSEM image showing the micritic cement which comprises idiomorphic rhombs of high magnesian calcite. Note that rims of micrite have preferentially formed around the detrital calcite grains. Sample GT009

ED-EPMA analysis of the carbonate cements are presented in Figure 7 and are summarised in Table 7. The micritic magnesian calcite cements contain between 32 and 46 mole % $MgCO_3$ in solid solution (i.e. the structural formula of the calcite can be represented as $Ca_{0.54-0.68}Mg_{0.46-0.32}CO_3$). This is consistent with the XRD which shows that very high magnesian calcite is the dominant carbonate mineral (Table 2). The composition of the coarser microsparite rims around detrital carbonate grains is similar to the micritic intergranular cement (Figure 7).

The sequence of sedimentary and post-depositional diagenetic events recorded from sample GT009 can be summarised as follows:

1. Deposition of fine, medium- and coarse grained sand, and finer-grained silty sediment.
2. Syndepositional bioturbation and subsequent burrow infill with fine-grained, muddy material.
3. Precipitation of micritic high-magnesian calcite within the near-surface of the sediment, causing lithification.
4. Oxidation of reduced iron minerals, producing secondary iron oxyhydroxide staining, with oxidation pathways possibly controlled by burrows.

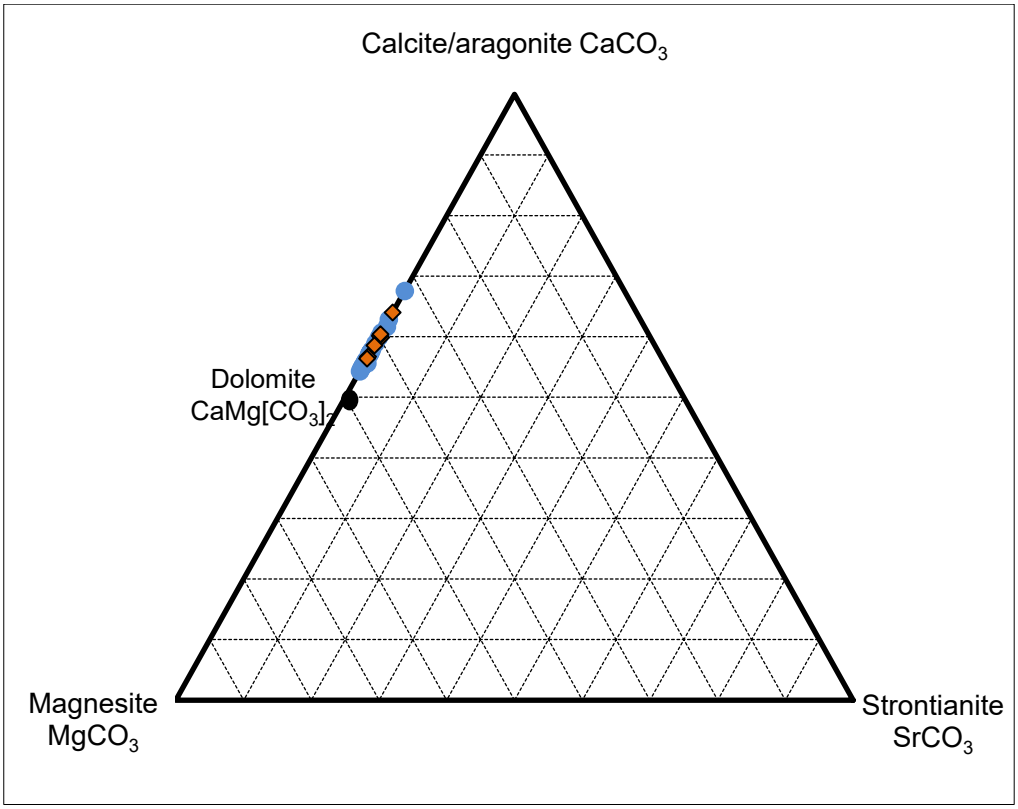

Figure 7. $CaCO_3$-$MgCO_3$-$SrCO_3$ molar ratio plot illustrating the compositions of the high-magnesian calcite micritic cement (solid blue circles), and blocky micrite rims (solid orange diamonds) from sample GT009.

Table 7. Electron microprobe analyses of carbonate cements in sample GT009

		Weight % oxide (normalised)							Ionic ratio [normalised to 3 [O]						COMMENTS
SAMPLE	No	MgO	CaO	MnO	FeO	SrO	CO_2 (calc)	*Total wt%	Mg^{2+}	Ca^{2+}	Mn^{2+}	Fe^{2+}	Sr^{2+}	CO_3^{2-}	
GT009	1	19.83	32.79	0.00	0.00	0.00	47.38	100	0.46	0.54	0.00	0.00	0.00	1.00	micrite
GT009	2	18.97	33.80	0.00	0.00	0.00	47.23	100	0.44	0.56	0.00	0.00	0.00	1.00	micrite
GT009	3	19.22	33.51	0.00	0.00	0.00	47.27	100	0.44	0.56	0.00	0.00	0.00	1.00	micrite
GT009	4	18.26	34.21	0.00	0.48	0.00	47.06	100	0.42	0.57	0.00	0.01	0.00	1.00	micrite
GT009	5	18.90	33.30	0.00	0.22	0.48	47.10	100	0.44	0.55	0.00	0.00	0.00	1.00	micrite
GT009	6	18.43	34.24	0.00	0.21	0.00	47.12	100	0.43	0.57	0.00	0.00	0.00	1.00	micrite
GT009	7	16.19	36.52	0.00	0.30	0.34	46.65	100	0.38	0.61	0.00	0.00	0.00	1.00	micrite
GT009	8	18.99	33.53	0.00	0.27	0.00	47.20	100	0.44	0.56	0.00	0.00	0.00	1.00	micrite
GT009	9	18.56	34.28	0.00	0.00	0.00	47.16	100	0.43	0.57	0.00	0.00	0.00	1.00	micrite
GT009	10	18.55	34.30	0.00	0.00	0.00	47.15	100	0.43	0.57	0.00	0.00	0.00	1.00	micrite
GT009	11	19.35	33.05	0.00	0.34	0.00	47.26	100	0.45	0.55	0.00	0.00	0.00	1.00	micrite
GT009	12	19.66	33.00	0.00	0.00	0.00	47.35	100	0.45	0.55	0.00	0.00	0.00	1.00	micrite
GT009	13	17.98	34.34	0.00	0.69	0.00	46.99	100	0.42	0.57	0.00	0.01	0.00	1.00	micrite
GT009	14	18.26	34.24	0.00	0.43	0.00	47.07	100	0.42	0.57	0.00	0.01	0.00	1.00	micrite
GT009	15	17.23	35.84	0.00	0.00	0.00	46.93	100	0.40	0.60	0.00	0.00	0.00	1.00	micrite
GT009	16	16.88	36.25	0.00	0.00	0.00	46.87	100	0.39	0.61	0.00	0.00	0.00	1.00	micrite
GT009	17	15.89	37.41	0.00	0.00	0.00	46.70	100	0.37	0.63	0.00	0.00	0.00	1.00	micrite
GT009	18	19.31	32.93	0.00	0.52	0.00	47.24	100	0.45	0.55	0.00	0.01	0.00	1.00	micrite
GT009	19	18.15	33.93	0.00	0.92	0.00	47.00	100	0.42	0.57	0.00	0.01	0.00	1.00	micrite
GT009	20	13.36	38.69	0.00	1.87	0.00	46.08	100	0.32	0.66	0.00	0.02	0.00	1.00	micrite
GT009	21	17.61	35.13	0.00	0.29	0.00	46.97	100	0.41	0.59	0.00	0.00	0.00	1.00	micrite
GT009	22	19.20	32.61	0.00	1.01	0.00	47.17	100	0.44	0.54	0.00	0.01	0.00	1.00	micrite
GT009	23	15.19	37.58	0.00	0.73	0.00	46.51	100	0.36	0.63	0.00	0.01	0.00	1.00	blocky rim micrite
GT009	24	16.88	35.36	0.00	0.64	0.39	46.73	100	0.39	0.59	0.00	0.01	0.00	1.00	blocky rim micrite
GT009	25	16.99	35.70	0.00	0.47	0.00	46.84	100	0.40	0.60	0.00	0.01	0.00	1.00	blocky rim micrite
GT009	26	17.77	34.94	0.00	0.30	0.00	46.99	100	0.41	0.58	0.00	0.00	0.00	1.00	blocky rim micrite
GT009	27	16.93	35.93	0.00	0.29	0.00	46.85	100	0.39	0.60	0.00	0.00	0.00	1.00	blocky rim micrite
GT009	28	18.63	33.99	0.00	0.23	0.00	47.15	100	0.43	0.57	0.00	0.00	0.00	1.00	blocky rim micrite
GT009	29	18.78	33.83	0.00	0.21	0.00	47.18	100	0.43	0.56	0.00	0.00	0.00	1.00	blocky rim micrite

**Note: Some analytical totals were low (<90%) because of the microporous nature of the cements. Therefore all data were normalised to 100%*

4.5 SAMPLE GT012

This sample comprised two sub-angular tabular clasts (approximately 100 mm in diameter) of medium grained sandstones. Surfaces show numerous exposed burrows, and minor bryozoan calcareous worm / serpulid encrustations. One clast has a strong orange-brown colouration on the surface, and the second clast is generally light grey with a patchy colouration, from iron oxyhydroxide staining (Plate 23).

Plate 23. Photograph of sample GT012 which comprises two sub-angular sandstone clasts. The samples show evidence of oxidation with orange-brown colouration caused by iron oxyhydroxides. Surfaces contain detrital bioclastic debris and are encrusted with minor bryozoan and calcareous worm / serpulid formations. Field of view ~210 mm wide.

The polished thin section prepared through one of the two GT012 clasts is shown in Plate 24. It shows diffuse, broad, horizontal laminations across the sample, which alternate between dark-mid brown, well-cemented, micritic bands, and less well-cemented, more porous bands of sandstone. The more porous areas have a well-developed acicular aragonite cement, where needles of aragonite up to 50 µm long, have nucleated on clots of micrite, and have grown into the adjacent intergranular pore spaces (Plate 25). Some aragonite cement appears to have grown locally as coarser fibrous fringes around fragments of mollusc shell. This may be due to preferential seeding on primary aragonite in the mollusc shell (since some shell fragments may originally have been aragonitic). The micrite-dominated sandstone bands (e.g. Plate 26) are more densely cemented with a fine-grained matrix of magnesian calcite, and show little or no evidence of acicular aragonite cements. Some dense, roughly elliptical patches of micritic clay (>500 µm) are seen in thin section that are probably a combination of detrital faecal pellets, and cross sections through infilled burrows. Detrital grains are angular to sub-angular, and quartz dominated. Rare microfossil bioclasts and rounded grains of detrital glauconite ("glauconie" *sensu lato*) are present throughout the sample.

High resolution BSEM indicates that the intergranular matrix of the sandstone comprises patches of siliceous clay-rich material mixed with anhedral magnesian calcite crystals, and more

microsparry cemented areas with euhedral rhombs of magnesian-calcite (Plate 27). Some minor acicular aragonite crystals are present in these areas, although very few compared to the cleaner, better-sorted and more porous sandstone bands, which are aragonite-cement dominated (Plate 28).

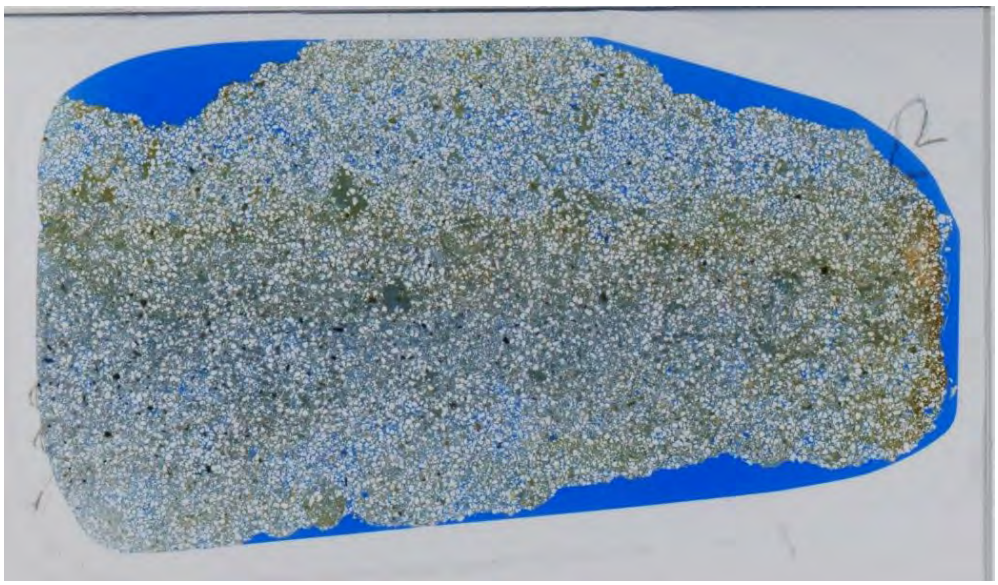

Plate 24. Scanned image of thin section from sample GT012. Areas of cementation and contrasting higher porosity are distributed in broadly horizontal bands. An orange-brown colouration from finely disseminated iron oxyhydroxides is visible within the well-cemented bands, and is particularly noticeable along the right edge of the above image. Field of view = 48 mm wide.

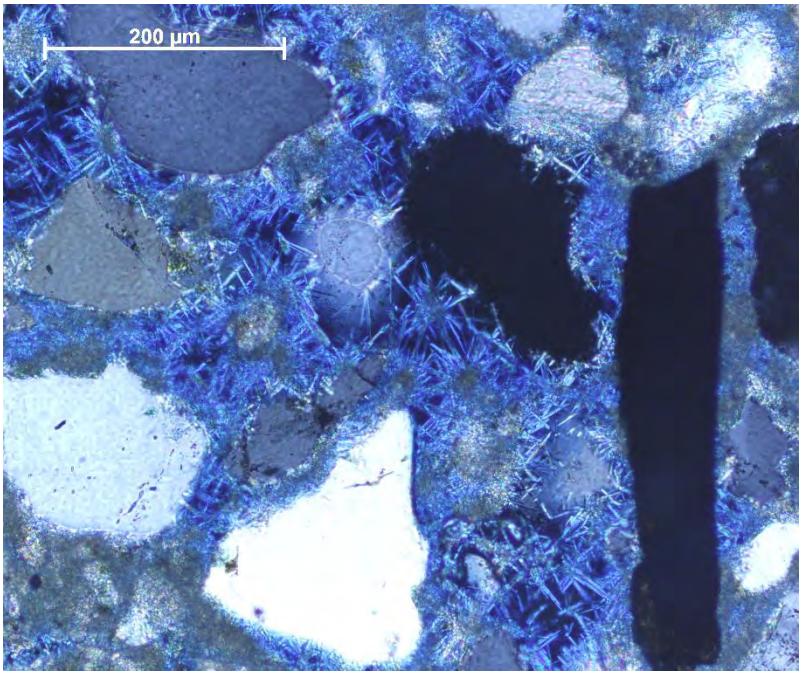

Plate 25. Transmitted light micrograph (cross-polarised light) from an area of high porosity. Acicular aragonite crystals can be seen nucleated around clots of micritic magnesian calcite and growing into the adjacent intergranular pore spaces. Sample GT012

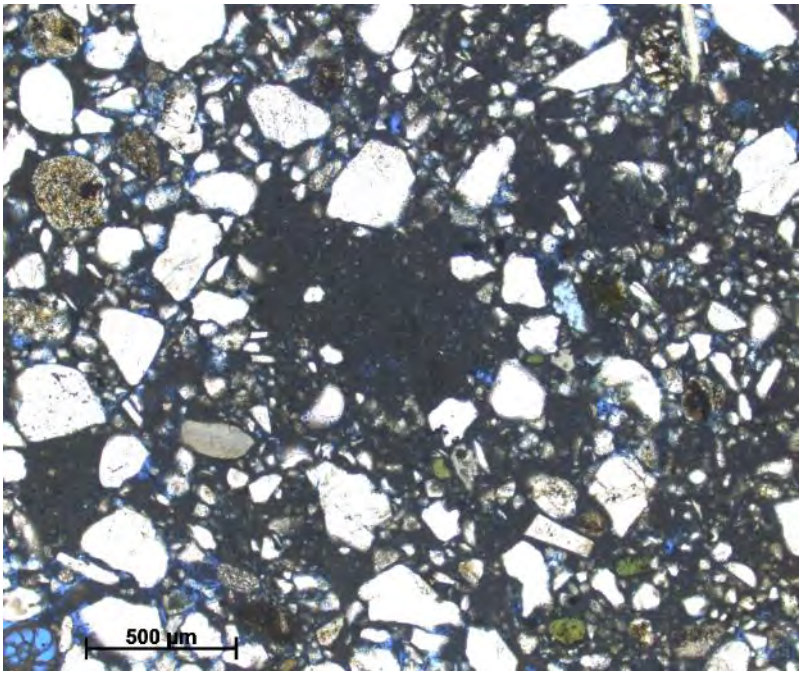

Plate 26. Transmitted light micrograph (plane-polarised light) showing a more densely cemented area. The cement here is a dense, dark brown, fine-grained magnesian calcite micrite with little evidence of any acicular aragonite cement. Three micrite-dominated patches with a slightly elliptic form are visible across the sample which are possibly slightly compacted faecal pellets, or cross sections of infilled burrows. Sample GT012

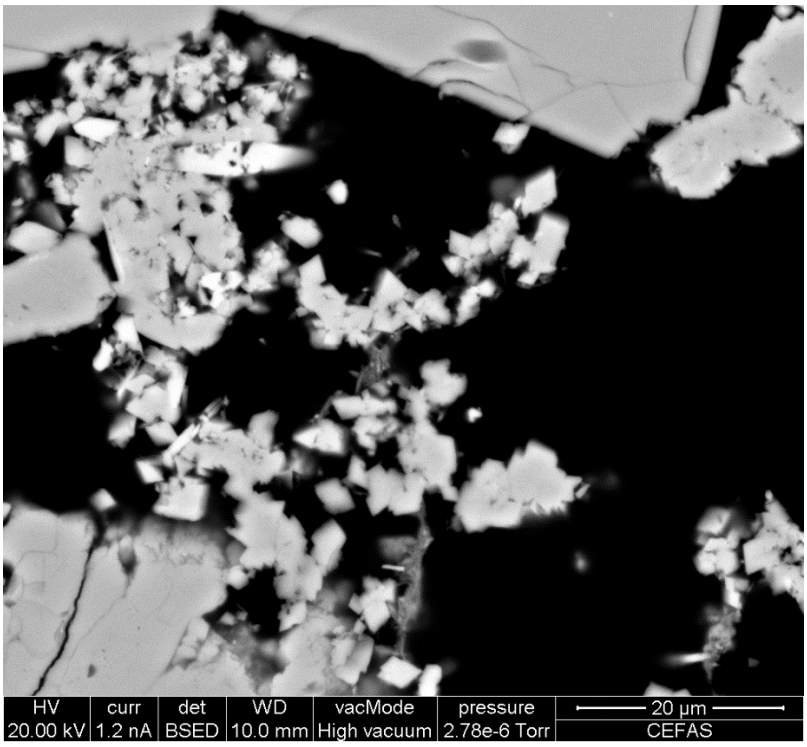

Plate 27. An area of micrite comprising euhedral rhombs of magnesian calcite (mid-grey). Note the presence of an acicular needle of aragonite (white) growing on and around the magnesian calcite, seen towards the top of the image. Sample GT012.

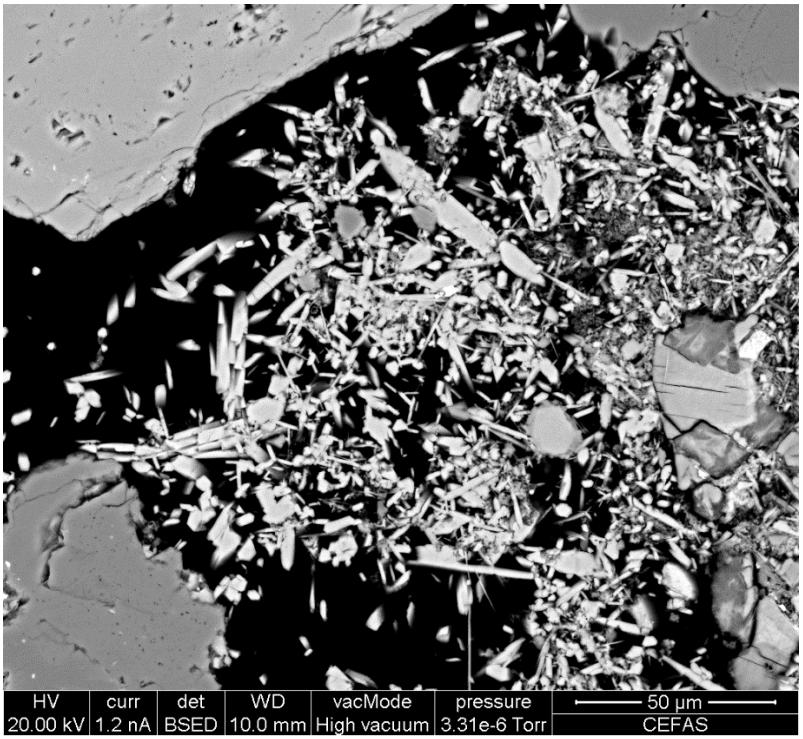

Plate 28. BSEM image of a porous sandstone region dominated by acicular aragonite-cement. Sample GT012.

ED-EPMA analysis of the carbonate cements are presented in Table 8 and are summarised in Figure 8. The micritic magnesian calcite cements span a wide range of compositions, containing between 1 and 23 mole % $MgCO_3$ in solid solution (i.e. the structural formula of the calcite can be represented as $Ca_{0.77\text{-}0.99}Mg_{0.23\text{-}0.01}CO_3$), and are lower in magnesium than some of the other samples studied. Nevertheless, some of the analyses are still at the higher-magnesian calcite end of the calcite ($CaCO_3$)-magnesite ($MgCO_3$) solid-solution series (cf. Deer et al., 1962a, b: Mackenzie et al., 1983).

The acicular aragonite is strontium bearing, with <2 mole % $SrCO_3$ in solid-solution (i.e. the structural formula (i.e. the structural formula of the aragonite can be represented as $Ca_{0.98\text{-}0.99}Sr_{0.02\text{-}0.01}CO_3$). Together with the prismatic morphology, the relatively high Sr content supports the identification of this carbonate cement as aragonite rather than calcite. Strontium is more abundant in aragonite than in calcite (Deer et al., 1962a, b) because it is much more readily incorporated in the orthorhombic crystal structure of aragonite, which can form a partial solid-solution series with the end-member orthorhombic strontianite ($SrCO_3$).

Aragonite cement has been recorded previously by Judd (2005) and Milodowski et al., (2009), in MDAC from the Mid Irish Sea. Needles of aragonite have also been described encrusting sand grains (similar to the pore-filling acicular aragonite described above) by Croker et al., (2005) from SEM observations of recovered from potential MDAC samples recovered in the Western Irish Sea. Similar acicular and "pelleted" aragonite fabrics have been observed in studies of MDAC from other areas (e.g. Hovland and Talbot, 1987; Jensen et al., 1992; Bohrmann et al., 1998; Peckmann et al., 2001; Muralidhar et al., 2006; Milodowski et al., 2013). Peckmann et al. (2001) report the formation of acicular Sr-rich aragonite cement, with between 8300-9500 ppm Sr, in MDAC associated with methane seeps from the Black Sea. The strontium content of the aragonite cements reported by Peckmann et al. (2001), Milodowski et al., (2009) and Milodowski and Sloane (2013) from the Mid Irish Sea and the Braemar Pockmark in the North Sea is also of a similar order of magnitude to those described in this sample.

The sequence of sedimentary and post-depositional diagenetic events recorded from sample GT012 can be summarised as follows:

1. Deposition of medium-grained sandstone sediment.
2. Syndepositional bioturbation.
3. Precipitation of micritic high-magnesian calcite within the near-surface of the sediment, causing lithification.
4. Subsequent precipitation of acicular aragonite cement, in clean, low- to micrite-free intergranular pore space. Some of the aragonite preferentially nucleated on fragments of aragonitic shell detritus. The change from magnesian calcite to aragonite precipitation probably reflects a change in porewater chemistry or geochemical conditions.
5. Oxidation with the precipitation of secondary fine grained iron oxyhydroxide within the fine-grained cements.
6. Subsequent minor colonisation by bryozoan and other marine organisms.

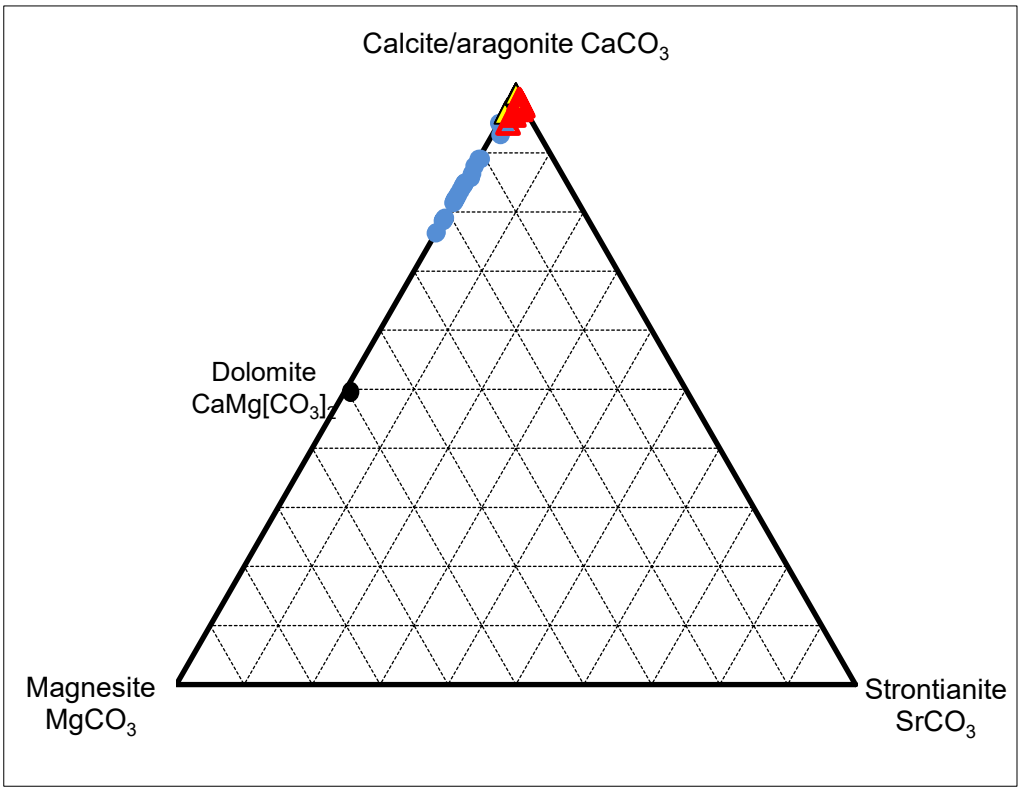

Figure 8. $CaCO_3$-$MgCO_3$-$SrCO_3$ molar ratio plot illustrating the compositions of the high-magnesian calcite micritic cement (solid blue circles), aragonite cement (red open triangles), and shell fragments (solid yellow triangles) from sample GT012.

Table 8. Electron microprobe analyses of carbonate cements and shelly fragments in sample GT012

		Weight % oxide (normalised)							Ionic ratio [normalised to 3 [O]						COMMENTS
SAMPLE	No	MgO	CaO	MnO	FeO	SrO	CO_2 (calc)	*Total wt%	Mg^{2+}	Ca^{2+}	Mn^{2+}	Fe^{2+}	Sr^{2+}	CO_3^{2-}	
GT012	1	0.18	55.83	0.00	0.00	0.00	44.00	100	0.00	1.00	0.00	0.00	0.00	1.00	shelly fragment
GT012	2	0.33	55.64	0.00	0.00	0.00	44.02	100	0.01	0.99	0.00	0.00	0.00	1.00	shelly fragment
GT012	3	0.00	56.04	0.00	0.00	0.00	43.96	100	0.00	1.00	0.00	0.00	0.00	1.00	shelly fragment
GT012	4	0.00	56.04	0.00	0.00	0.00	43.96	100	0.00	1.00	0.00	0.00	0.00	1.00	shelly fragment
GT012	5	1.02	54.60	0.00	0.26	0.00	44.12	100	0.03	0.97	0.00	0.00	0.00	1.00	shelly fragment
GT012	6	1.22	54.60	0.00	0.00	0.00	44.18	100	0.03	0.97	0.00	0.00	0.00	1.00	shelly fragment
GT012	7	0.64	54.71	0.00	0.24	0.44	43.96	100	0.02	0.98	0.00	0.00	0.00	1.00	shelly fragment
GT012	8	1.30	54.26	0.00	0.28	0.00	44.16	100	0.03	0.96	0.00	0.00	0.00	1.00	shelly fragment
GT012	9	0.95	54.70	0.00	0.25	0.00	44.10	100	0.02	0.97	0.00	0.00	0.00	1.00	shelly fragment
GT012	11	0.00	56.04	0.00	0.00	0.00	43.96	100	0.00	1.00	0.00	0.00	0.00	1.00	shelly fragment
GT012	12	0.00	56.04	0.00	0.00	0.00	43.96	100	0.00	1.00	0.00	0.00	0.00	1.00	shelly fragment
GT012	13	0.00	56.04	0.00	0.00	0.00	43.96	100	0.00	1.00	0.00	0.00	0.00	1.00	shelly fragment
GT012	14	0.00	56.04	0.00	0.00	0.00	43.96	100	0.00	1.00	0.00	0.00	0.00	1.00	shelly fragment
GT012	15	0.00	56.04	0.00	0.00	0.00	43.96	100	0.00	1.00	0.00	0.00	0.00	1.00	shelly fragment
GT012	16	0.00	54.29	0.00	0.00	2.19	43.52	100	0.00	0.98	0.00	0.00	0.02	1.00	shelly fragment
GT012	17	0.20	54.37	0.00	0.00	1.79	43.64	100	0.01	0.98	0.00	0.00	0.02	1.00	shelly fragment
GT012	18	0.22	54.05	0.00	0.00	2.17	43.56	100	0.01	0.97	0.00	0.00	0.02	1.00	shelly fragment
GT012	19	6.47	48.24	0.24	0.00	0.00	45.06	100	0.16	0.84	0.00	0.00	0.00	1.00	micrite infill and rim around shell
GT012	20	7.34	47.44	0.00	0.00	0.00	45.23	100	0.18	0.82	0.00	0.00	0.00	1.00	micrite infill and rim around shell
GT012	21	6.36	48.58	0.00	0.00	0.00	45.06	100	0.15	0.85	0.00	0.00	0.00	1.00	micrite infill and rim around shell
GT012	22	6.23	48.74	0.00	0.00	0.00	45.04	100	0.15	0.85	0.00	0.00	0.00	1.00	micrite infill and rim around shell
GT012	23	6.74	48.14	0.00	0.00	0.00	45.12	100	0.16	0.84	0.00	0.00	0.00	1.00	micrite infill and rim around shell
GT012	24	5.41	49.21	0.00	0.26	0.32	44.81	100	0.13	0.86	0.00	0.00	0.00	1.00	micrite infill and rim around shell
GT012	25	6.20	48.76	0.00	0.00	0.00	45.03	100	0.15	0.85	0.00	0.00	0.00	1.00	micrite infill and rim around shell
GT012	26	7.20	47.59	0.00	0.00	0.00	45.20	100	0.17	0.83	0.00	0.00	0.00	1.00	micrite infill and rim around shell
GT012	27	4.35	50.36	0.36	0.00	0.31	44.62	100	0.11	0.89	0.00	0.00	0.00	1.00	micrite infill and rim around shell
GT012	28	7.47	46.90	0.20	0.23	0.00	45.21	100	0.18	0.81	0.00	0.00	0.00	1.00	micrite infill and rim around shell
GT012	29	8.85	45.66	0.00	0.00	0.00	45.49	100	0.21	0.79	0.00	0.00	0.00	1.00	micrite infill and rim around shell
GT012	30	2.31	52.08	0.00	0.26	1.27	44.08	100	0.06	0.93	0.00	0.00	0.01	1.00	micrite cement
GT012	31	0.96	53.71	0.00	0.00	1.49	43.83	100	0.02	0.96	0.00	0.00	0.01	1.00	micrite cement
GT012	32	4.49	50.56	0.00	0.24	0.00	44.71	100	0.11	0.89	0.00	0.00	0.00	1.00	micrite cement
GT012	33	6.99	47.60	0.27	0.00	0.00	45.14	100	0.17	0.83	0.00	0.00	0.00	1.00	micrite cement

		Weight % oxide (normalised)							Ionic ratio [normalised to 3 [O]						COMMENTS
SAMPLE	No	MgO	CaO	MnO	FeO	SrO	CO_2 (calc)	*Total wt%	Mg^{2+}	Ca^{2+}	Mn^{2+}	Fe^{2+}	Sr^{2+}	CO_3^{2-}	
GT012	34	7.45	46.93	0.00	0.42	0.00	45.21	100	0.18	0.81	0.00	0.01	0.00	1.00	micrite cement
GT012	35	9.76	44.41	0.00	0.21	0.00	45.62	100	0.23	0.76	0.00	0.00	0.00	1.00	micrite cement
GT012	36	9.77	44.04	0.00	0.60	0.00	45.59	100	0.23	0.76	0.00	0.01	0.00	1.00	micrite cement
GT012	37	8.73	45.80	0.00	0.00	0.00	45.47	100	0.21	0.79	0.00	0.00	0.00	1.00	micrite cement
GT012	38	0.33	54.29	0.00	0.44	1.21	43.74	100	0.01	0.97	0.00	0.01	0.01	1.00	micrite cement
GT012	39	0.77	53.50	0.00	0.54	1.44	43.76	100	0.02	0.96	0.00	0.01	0.01	1.00	micrite cement
GT012	40	8.85	45.24	0.00	0.47	0.00	45.44	100	0.21	0.78	0.00	0.01	0.00	1.00	micrite cement
GT012	41	7.31	47.18	0.31	0.00	0.00	45.19	100	0.18	0.82	0.00	0.00	0.00	1.00	micrite cement
GT012	42	8.87	45.36	0.00	0.31	0.00	45.46	100	0.21	0.78	0.00	0.00	0.00	1.00	micrite cement
GT012	43	2.01	53.68	0.00	0.00	0.00	44.31	100	0.05	0.95	0.00	0.00	0.00	1.00	micrite cement
GT012	44	7.57	46.67	0.21	0.33	0.00	45.22	100	0.18	0.81	0.00	0.00	0.00	1.00	micrite cement
GT012	45	5.63	48.79	0.00	0.29	0.47	44.81	100	0.14	0.85	0.00	0.00	0.00	1.00	micrite cement
GT012	46	6.29	48.18	0.00	0.53	0.00	45.00	100	0.15	0.84	0.00	0.01	0.00	1.00	micrite cement
GT012	47	4.95	49.53	0.32	0.45	0.00	44.74	100	0.12	0.87	0.00	0.01	0.00	1.00	micrite cement
GT012	48	8.98	45.51	0.00	0.00	0.00	45.51	100	0.22	0.78	0.00	0.00	0.00	1.00	micrite cement
GT012	49	0.36	54.29	0.00	0.00	1.66	43.69	100	0.01	0.97	0.00	0.00	0.02	1.00	acicular shard in micrite
GT012	50	0.23	54.14	0.00	0.00	2.05	43.59	100	0.01	0.97	0.00	0.00	0.02	1.00	acicular shard in micrite
GT012	51	0.34	54.32	0.00	0.00	1.66	43.69	100	0.01	0.98	0.00	0.00	0.02	1.00	acicular shard in micrite
GT012	52	0.82	54.03	0.00	0.00	1.31	43.84	100	0.02	0.97	0.00	0.00	0.01	1.00	acicular shard in micrite
GT012	53	0.00	54.93	0.00	0.00	1.38	43.69	100	0.00	0.99	0.00	0.00	0.01	1.00	acicular aragonite cement
GT012	54	0.17	54.28	0.00	0.53	1.34	43.67	100	0.00	0.98	0.00	0.01	0.01	1.00	acicular aragonite cement
GT012	55	0.30	54.43	0.00	0.21	1.34	43.73	100	0.01	0.98	0.00	0.00	0.01	1.00	acicular aragonite cement
GT012	56	0.00	54.24	0.00	0.52	1.66	43.58	100	0.00	0.98	0.00	0.01	0.02	1.00	acicular aragonite cement
GT012	57	0.00	54.98	0.00	0.00	1.32	43.70	100	0.00	0.99	0.00	0.00	0.01	1.00	acicular aragonite cement
GT012	58	0.00	53.37	0.00	1.34	1.82	43.47	100	0.00	0.96	0.00	0.02	0.02	1.00	acicular aragonite cement
GT012	59	0.20	54.03	0.00	0.38	1.79	43.60	100	0.01	0.97	0.00	0.01	0.02	1.00	acicular aragonite cement
GT012	60	0.27	53.71	0.00	0.75	1.67	43.60	100	0.01	0.97	0.00	0.01	0.02	1.00	acicular aragonite cement
GT012	61	0.15	54.28	0.00	0.33	1.60	43.64	100	0.00	0.98	0.00	0.00	0.02	1.00	acicular aragonite cement
GT012	62	0.83	53.42	0.00	0.49	1.50	43.76	100	0.02	0.96	0.00	0.01	0.01	1.00	acicular aragonite cement
GT012	63	0.32	52.94	0.00	1.47	1.75	43.53	100	0.01	0.95	0.00	0.02	0.02	1.00	acicular aragonite cement
GT012	64	0.00	54.40	0.00	0.64	1.32	43.64	100	0.00	0.98	0.00	0.01	0.01	1.00	acicular aragonite cement
GT012	65	0.00	54.67	0.00	0.00	1.71	43.62	100	0.00	0.98	0.00	0.00	0.02	1.00	acicular aragonite cement
GT012	66	1.44	52.81	0.00	0.50	1.36	43.89	100	0.04	0.94	0.00	0.01	0.01	1.00	acicular aragonite cement
GT012	67	0.31	54.05	0.00	0.65	1.30	43.69	100	0.01	0.97	0.00	0.01	0.01	1.00	acicular aragonite cement

		Weight % oxide (normalised)							Ionic ratio [normalised to 3 [O]						COMMENTS
SAMPLE	No	MgO	CaO	MnO	FeO	SrO	CO_2 (calc)	*Total wt%	Mg^{2+}	Ca^{2+}	Mn^{2+}	Fe^{2+}	Sr^{2+}	CO_3^{2-}	
GT012	68	0.00	55.09	0.00	0.00	1.18	43.73	100	0.00	0.99	0.00	0.00	0.01	1.00	acicular aragonite cement
GT012	69	0.00	55.23	0.00	0.00	1.01	43.76	100	0.00	0.99	0.00	0.00	0.01	1.00	acicular aragonite cement
GT012	70	0.00	54.98	0.00	0.00	1.32	43.70	100	0.00	0.99	0.00	0.00	0.01	1.00	acicular aragonite cement
GT012	71	0.33	53.34	0.00	1.33	1.39	43.61	100	0.01	0.96	0.00	0.02	0.01	1.00	acicular aragonite cement
GT012	72	0.00	55.00	0.00	0.26	1.00	43.74	100	0.00	0.99	0.00	0.00	0.01	1.00	acicular aragonite cement
GT012	73	0.00	54.40	0.00	0.00	2.05	43.55	100	0.00	0.98	0.00	0.00	0.02	1.00	acicular aragonite cement

**Note: Some analytical totals were low (<90%) because of the microporous nature of the cements. Therefore all data were normalised to 100%*

4.6 SAMPLE GT014

This sample comprises three irregular shaped sub-tabular clasts of predominantly very fine to fine (<400 sandstone up to 100 mm in diameter (Plate 29). The clasts show evidence of extensive bioturbation, with exposed burrows visible on the surface and some burrows forming open channels penetrating through the entire clast. Other burrows have been infilled with fine-grained silt and bioclastic debris. The surface is also coated with numerous calcareous serpulid worm encrustations.

Plate 29. Photograph showing sample GT014. This comprises three irregular clasts of differing sizes. Burrows and borings pepper the sample, some penetrating the sample right the way through. Field of view ~180 mm wide.

The polished thin section prepared from one of the clasts is shown in Plate 30. The sample has a very patchy, brown colouration where silty sediment infilling some burrows, and the micrite matrix cement, have been stained by brown iron oxyhydroxides. The sample has an uncompact grain fabric with simple point grain contacts. Detrital grains are sub-angular to rounded (<400 µm), and are dominated by quartz with subordinate lithics, feldspars, detrital carbonate grains and minor bioclastic fragments. Optical petrography shows that the sandstone is strongly bioturbated and poorly-sorted, with a patchily-distributed fine-grained, brown, clay-rich intergranular micritic carbonate matrix or cement (Plate 31). The sandstone varies from grain-supported to matrix-supported. The micrite displays a “clotted” fabric comprised of aggregates of silt-sized rounded micrite pelloids, with coarser-grained micrite to microsparite forming overgrowth rims around these micrite aggregates (Plate 32).

High resolution BSEM-ED observations show that the micrite is high magnesian-calcite, and in general has a high clay and silica content. Cavities can be seen preserved within the micrite-cemented areas (Plate 33), which represent secondary porosity created by the dissolution of unstable detrital grains and shell fragments. However, no evidence was found of the microporous microcellular texture observed in the micrite of some other samples. In the more porous areas, the micrite has formed subidiomorphic to idiomorphic rhombic calcite crystals (Plate 34). Rare acicular aragonite needles are present within the intergranular pores, and grown on top of the micritic magnesian calcite (Plate 35), indicating that the aragonite post-dates the micritic magnesian calcite. Some calcareous bioclasts display acicular aragonite rims (<20 µm), which may be part of the original shell structure, rather than of authigenic origin.

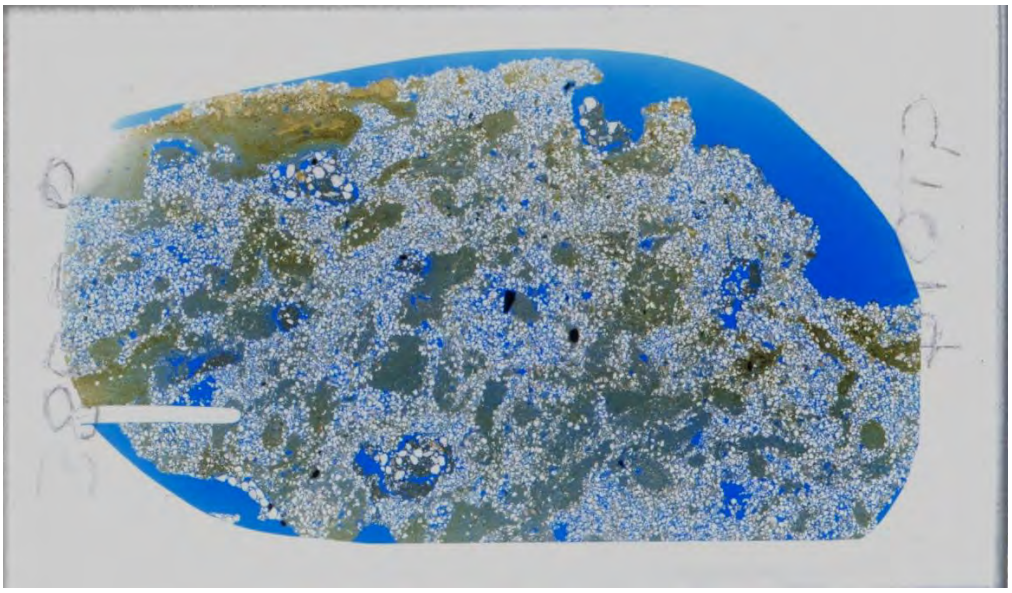

Plate 30. Scanned image of thin section from sample GT014. The clast has an irregular shape and is heavily bioturbated. Some of the burrows are infilled with a dark brown, fine-grained silt. Light orange-brown staining is visible from finely-disseminated iron oxyhydroxides. Field of view = 48 mm wide.

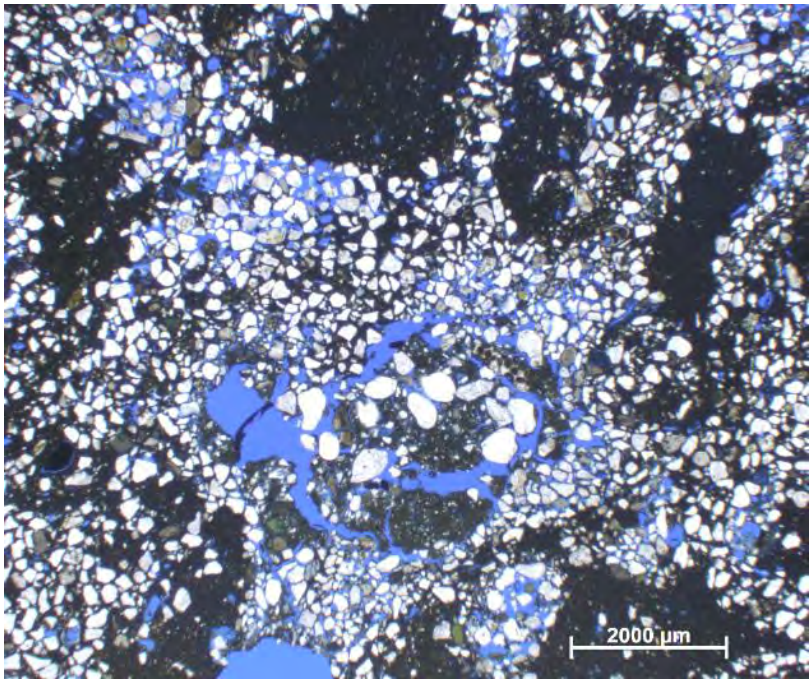

Plate 31. Transmitted light photomicrograph (plain polarised light) showing the highly bioturbated sample. Porosity is variable: some areas are highly cemented or matrix-rich, some have a high porosity. Sample GT014

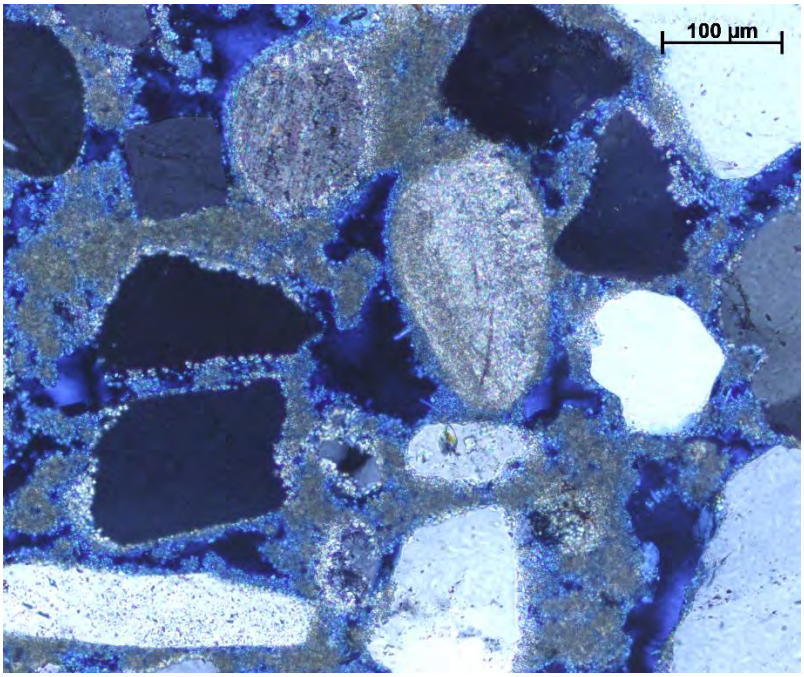

Plate 32. Transmitted light photomicrograph (cross polarised light) showing the globular clots of brown micritic cement surrounded by coarser, lighter coloured rims of high magnesian calcite. Rare acicular aragonite is also present. Sample GT014

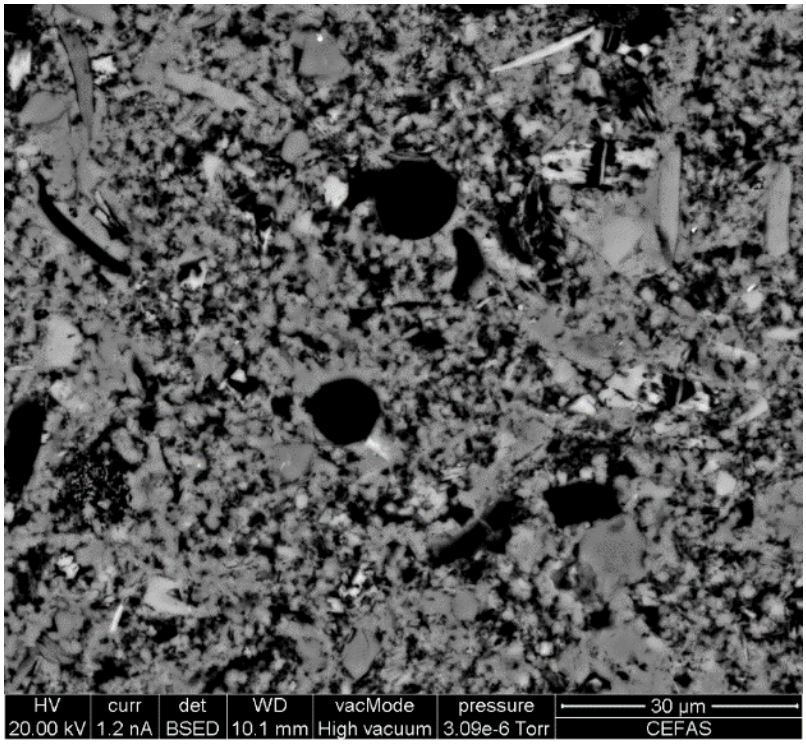

Plate 33. BSEM image showing the micrite cement. There are numerous oversized elongated and round voids which represent secondary porosity produced by the dissolution of unstable bioclastic material. The micrite matrix contains abundant disseminated clay. Sample GT014

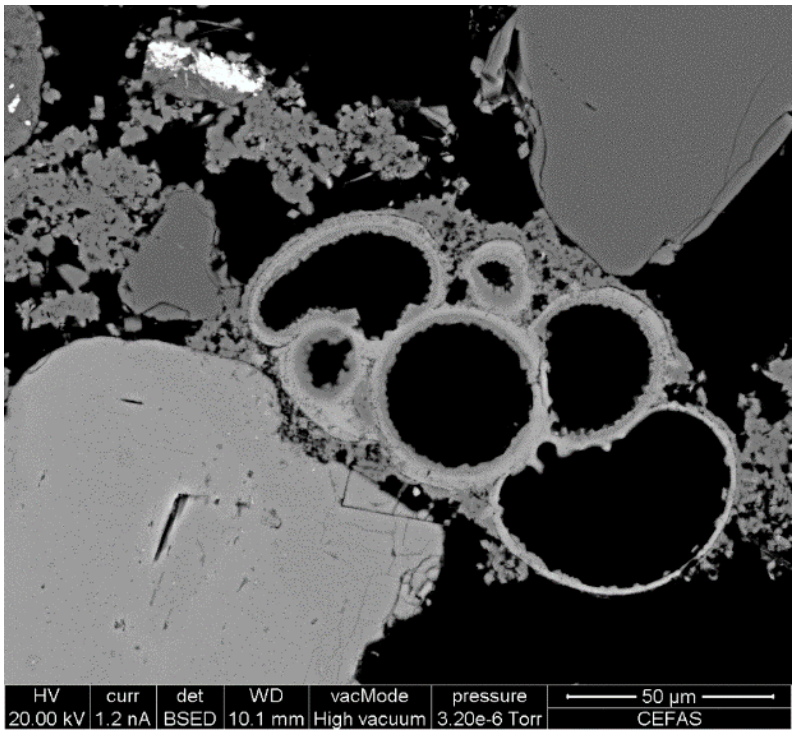

Plate 34. BSEM image detailing the cement from a high porosity area. A rare foraminifera test has been rimmed with blocky micrite both on the inside of the shell chambers as well out the outer surface. Calcite rhombs are idiomorphic to sub-idiomorphic, and very fine acicular crystals are visible (e.g. within the micrite cluster around the bright TiO_2 crystals upper left quadrant). Sample GT014

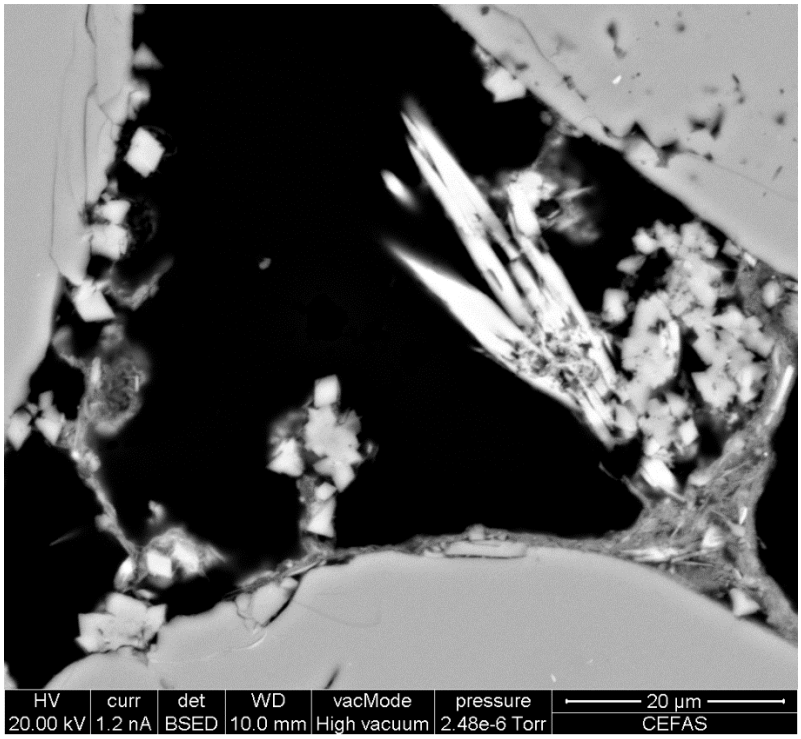

Plate 35. BSEM image showing rate acicular aragonite which has nucleated on top of the micritic cement. Sample GT014.

ED-EPMA analysis of the carbonate cements are presented in Table 9 and are summarised in Figure 9. The micritic magnesian calcite cements contain between 34 and 44 mole % $MgCO_3$ in solid solution within the crystal lattice (i.e. the structural formula of the calcite can be represented as $Ca_{0.56\text{-}0.66}Mg_{0.44\text{-}0.34}CO_3$). The composition of the micrite rims around the inner cavities of the shell debris, is similar to the range of compositions within the micritic intergranular cement (Figure 9). Analyses of the shell fragments range from pure calcite, to a magnesian calcite with up to 10 mole % $MgCO_3$. The high magnesium content may indicate that some of the shell material has been recrystallised and replaced by magnesian calcite. The acicular aragonite contains 1 mole % Sr.

The sequence of sedimentary and post-depositional diagenetic events recorded from sample GT014 can be summarised as follows:

1. Deposition of very fine to fine-grained sand, and silt.
2. Syndepositional bioturbation and subsequent burrow infill with fine-grained, muddy material.
3. Precipitation of micritic high-magnesian calcite within the near-surface of the sediment, causing lithification.
4. Precipitation of minor late acicular aragonite in open pores on top the early micritic cement.
5. Oxidation with the precipitation of fine grained iron oxyhydroxide within the fine-grained micrite and burrow infill material.
6. Colonisation by marine organisms, evidenced by calcareous serpulid worm encrustations, on the lithified surface of the clast.

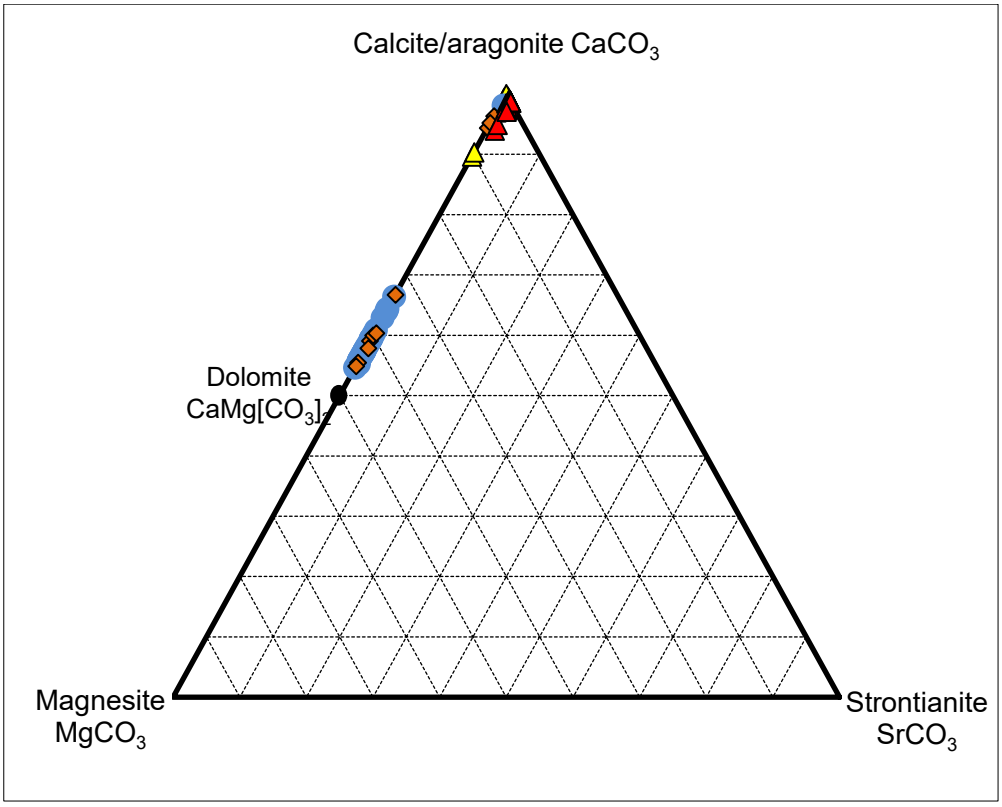

Figure 9. $CaCO_3$-$MgCO_3$-$SrCO_3$ molar ratio plot illustrating the compositions of the high-magnesian calcite micritic cement (solid blue circles), shelly bioclastic fragments (solid yellow triangles) and blocky micrite/calcite rims on inner and outer shell surfaces (solid orange diamonds), and isopachous aragonite fringes around detrital bioclasts and acicular aragonite cement (solid red triangles) from sample GT014.

Table 9. Electron microprobe analyses of carbonate cements and bioclast fragments in sample GT014

		Weight % oxide (normalised)							Ionic ratio [normalised to 3 [O]						COMMENTS
SAMPLE	No	MgO	CaO	MnO	FeO	SrO	CO_2 (calc)	*Total wt%	Mg^{2+}	Ca^{2+}	Mn^{2+}	Fe^{2+}	Sr^{2+}	CO_3^{2-}	
GT014	1	16.99	35.76	0.00	0.41	0.00	46.85	100	0.40	0.60	0.00	0.01	0.00	1.00	micrite
GT014	2	15.80	37.29	0.00	0.25	0.00	46.66	100	0.37	0.63	0.00	0.00	0.00	1.00	micrite
GT014	3	17.39	35.45	0.00	0.23	0.00	46.93	100	0.40	0.59	0.00	0.00	0.00	1.00	micrite
GT014	4	18.28	34.36	0.00	0.27	0.00	47.08	100	0.42	0.57	0.00	0.00	0.00	1.00	micrite
GT014	5	17.51	35.22	0.00	0.33	0.00	46.95	100	0.41	0.59	0.00	0.00	0.00	1.00	micrite
GT014	6	18.40	34.47	0.00	0.00	0.00	47.13	100	0.43	0.57	0.00	0.00	0.00	1.00	micrite
GT014	27	17.52	35.50	0.00	0.00	0.00	46.98	100	0.41	0.59	0.00	0.00	0.00	1.00	micrite
GT014	28	15.31	37.86	0.00	0.26	0.00	46.57	100	0.36	0.64	0.00	0.00	0.00	1.00	micrite
GT014	29	17.38	35.33	0.00	0.37	0.00	46.92	100	0.40	0.59	0.00	0.00	0.00	1.00	micrite
GT014	30	19.00	33.77	0.00	0.00	0.00	47.23	100	0.44	0.56	0.00	0.00	0.00	1.00	micrite
GT014	32	18.33	34.26	0.00	0.33	0.00	47.09	100	0.42	0.57	0.00	0.00	0.00	1.00	micrite
GT014	33	18.12	34.80	0.00	0.00	0.00	47.08	100	0.42	0.58	0.00	0.00	0.00	1.00	micrite
GT014	39	18.62	34.01	0.00	0.22	0.00	47.15	100	0.43	0.57	0.00	0.00	0.00	1.00	micrite
GT014	40	17.31	35.49	0.00	0.29	0.00	46.91	100	0.40	0.59	0.00	0.00	0.00	1.00	micrite
GT014	41	16.66	36.09	0.00	0.47	0.00	46.78	100	0.39	0.61	0.00	0.01	0.00	1.00	micrite
GT014	42	19.20	33.53	0.00	0.00	0.00	47.27	100	0.44	0.56	0.00	0.00	0.00	1.00	micrite
GT014	43	17.92	35.03	0.00	0.00	0.00	47.05	100	0.42	0.58	0.00	0.00	0.00	1.00	micrite
GT014	44	18.54	34.30	0.00	0.00	0.00	47.15	100	0.43	0.57	0.00	0.00	0.00	1.00	micrite
GT014	44	19.25	33.24	0.00	0.00	0.30	47.21	100	0.44	0.55	0.00	0.00	0.00	1.00	micrite
GT014	45	19.70	32.95	0.00	0.00	0.00	47.35	100	0.45	0.55	0.00	0.00	0.00	1.00	micrite
GT014	46	19.24	33.48	0.00	0.00	0.00	47.27	100	0.44	0.56	0.00	0.00	0.00	1.00	micrite
GT014	47	0.54	54.93	0.00	0.00	0.59	43.94	100	0.01	0.98	0.00	0.00	0.01	1.00	micrite
GT014	48	19.02	33.53	0.00	0.24	0.00	47.21	100	0.44	0.56	0.00	0.00	0.00	1.00	micrite
GT014	49	18.96	33.58	0.00	0.26	0.00	47.20	100	0.44	0.56	0.00	0.00	0.00	1.00	micrite
GT014	50	18.73	34.09	0.00	0.00	0.00	47.19	100	0.43	0.57	0.00	0.00	0.00	1.00	micrite
GT014	51	15.21	38.21	0.00	0.00	0.00	46.58	100	0.36	0.64	0.00	0.00	0.00	1.00	micrite
GT014	57	14.30	39.28	0.00	0.00	0.00	46.42	100	0.34	0.66	0.00	0.00	0.00	1.00	micrite
GT014	58	18.36	34.52	0.00	0.00	0.00	47.12	100	0.43	0.57	0.00	0.00	0.00	1.00	micrite
GT014	45	2.29	53.35	0.00	0.00	0.00	44.36	100	0.06	0.94	0.00	0.00	0.00	1.00	calcite rim on shell edge (outer)
GT014	46	1.48	54.09	0.00	0.22	0.00	44.20	100	0.04	0.96	0.00	0.00	0.00	1.00	calcite rim on shell edge (outer)
GT014	47	1.95	53.75	0.00	0.00	0.00	44.30	100	0.05	0.95	0.00	0.00	0.00	1.00	calcite rim on shell edge (outer)
GT014	7	17.62	35.39	0.00	0.00	0.00	46.99	100	0.41	0.59	0.00	0.00	0.00	1.00	micrite rim on shell (inner)

		Weight % oxide (normalised)							Ionic ratio [normalised to 3 [O]						COMMENTS
SAMPLE	No	MgO	CaO	MnO	FeO	SrO	CO_2 (calc)	*Total wt%	Mg^{2+}	Ca^{2+}	Mn^{2+}	Fe^{2+}	Sr^{2+}	CO_3^{2-}	
GT014	8	19.30	33.42	0.00	0.00	0.00	47.28	100	0.45	0.55	0.00	0.00	0.00	1.00	micrite rim on shell (inner)
GT014	9	19.57	33.10	0.00	0.00	0.00	47.33	100	0.45	0.55	0.00	0.00	0.00	1.00	micrite rim on shell (inner)
GT014	10	18.00	34.64	0.00	0.00	0.38	46.98	100	0.42	0.58	0.00	0.00	0.00	1.00	micrite rim on shell (inner)
GT014	11	17.22	35.86	0.00	0.00	0.00	46.93	100	0.40	0.60	0.00	0.00	0.00	1.00	micrite rim on shell (inner)
GT014	12	16.86	36.01	0.00	0.00	0.33	46.80	100	0.39	0.60	0.00	0.00	0.00	1.00	micrite rim on shell (inner)
GT014	13	14.15	39.45	0.00	0.00	0.00	46.40	100	0.33	0.67	0.00	0.00	0.00	1.00	micrite rim on shell (inner)
GT014	31	0.00	55.11	0.00	0.00	1.15	43.73	100	0.00	0.99	0.00	0.00	0.01	1.00	shell fragment
GT014	34	0.00	55.64	0.00	0.00	0.49	43.87	100	0.00	1.00	0.00	0.00	0.00	1.00	shell fragment
GT014	14	0.41	55.55	0.00	0.00	0.00	44.04	100	0.01	0.99	0.00	0.00	0.00	1.00	shell fragment
GT014	15	1.23	54.59	0.00	0.00	0.00	44.18	100	0.03	0.97	0.00	0.00	0.00	1.00	shell fragment
GT014	16	4.24	51.06	0.00	0.00	0.00	44.69	100	0.10	0.90	0.00	0.00	0.00	1.00	shell fragment
GT014	17	3.95	51.41	0.00	0.00	0.00	44.64	100	0.10	0.90	0.00	0.00	0.00	1.00	shell fragment
GT014	18	1.78	53.95	0.00	0.00	0.00	44.27	100	0.04	0.96	0.00	0.00	0.00	1.00	shell fragment
GT014	48	0.22	55.59	0.00	0.21	0.00	43.98	100	0.01	0.99	0.00	0.00	0.00	1.00	shell fragment
GT014	49	0.33	55.38	0.00	0.30	0.00	43.99	100	0.01	0.99	0.00	0.00	0.00	1.00	shell fragment
GT014	50	0.29	55.69	0.00	0.00	0.00	44.02	100	0.01	0.99	0.00	0.00	0.00	1.00	shell fragment
GT014	19	0.00	55.07	0.00	0.00	1.21	43.72	100	0.00	0.99	0.00	0.00	0.01	1.00	aragonite rim
GT014	20	0.26	54.51	0.00	0.00	1.53	43.70	100	0.01	0.98	0.00	0.00	0.01	1.00	aragonite rim
GT014	21	0.33	55.03	0.00	0.00	0.78	43.86	100	0.01	0.98	0.00	0.00	0.01	1.00	aragonite rim
GT014	22	0.46	54.24	0.00	0.00	1.57	43.73	100	0.01	0.97	0.00	0.00	0.02	1.00	aragonite rim
GT014	23	0.00	55.26	0.00	0.00	0.97	43.77	100	0.00	0.99	0.00	0.00	0.01	1.00	aragonite rim
GT014	24	0.00	55.13	0.00	0.00	1.13	43.74	100	0.00	0.99	0.00	0.00	0.01	1.00	aragonite rim
GT014	25	0.00	55.28	0.00	0.00	0.95	43.77	100	0.00	0.99	0.00	0.00	0.01	1.00	aragonite rim
GT014	26	0.36	54.39	0.00	0.27	1.21	43.76	100	0.01	0.98	0.00	0.00	0.01	1.00	aragonite rim
GT014	41	1.93	52.49	0.00	0.25	1.33	44.00	100	0.05	0.94	0.00	0.00	0.01	1.00	acicular aragonite
GT014	42	1.56	53.18	0.00	0.00	1.28	43.98	100	0.04	0.95	0.00	0.00	0.01	1.00	acicular aragonite
GT014	52	0.00	54.59	0.00	0.43	1.33	43.66	100	0.00	0.98	0.00	0.01	0.01	1.00	acicular aragonite
GT014	53	0.52	54.20	0.00	0.43	1.05	43.80	100	0.01	0.97	0.00	0.01	0.01	1.00	acicular aragonite
GT014	54	0.00	54.83	0.00	0.00	1.51	43.66	100	0.00	0.99	0.00	0.00	0.01	1.00	acicular aragonite
GT014	55	0.00	55.14	0.00	0.00	1.12	43.74	100	0.00	0.99	0.00	0.00	0.01	1.00	acicular aragonite
GT014	56	0.00	54.94	0.00	0.00	1.38	43.69	100	0.00	0.99	0.00	0.00	0.01	1.00	acicular aragonite
GT014	59	0.58	54.15	0.00	0.00	1.52	43.76	100	0.01	0.97	0.00	0.00	0.01	1.00	acicular aragonite
GT014	35	0.00	55.70	0.00	0.00	0.42	43.88	100	0.00	1.00	0.00	0.00	0.00	1.00	thin calcic band in bioclast
GT014	36	0.00	56.04	0.00	0.00	0.00	43.96	100	0.00	1.00	0.00	0.00	0.00	1.00	thin calcic band in bioclast

		Weight % oxide (normalised)							Ionic ratio [normalised to 3 [O]						COMMENTS
SAMPLE	No	MgO	CaO	MnO	FeO	SrO	CO_2 (calc)	*Total wt%	Mg^{2+}	Ca^{2+}	Mn^{2+}	Fe^{2+}	Sr^{2+}	CO_3^{2-}	
GT014	37	0.00	55.35	0.00	0.00	0.86	43.79	100	0.00	0.99	0.00	0.00	0.01	1.00	thin calcic band in bioclast
GT014	38	0.00	55.35	0.00	0.00	0.86	43.79	100	0.00	0.99	0.00	0.00	0.01	1.00	thin calcic band in bioclast

**Note: Some analytical totals were low (<90%) because of the microporous nature of the cements. Therefore all data were normalised to 100%*

4.7 SAMPLE GT015

This sample is buff-coloured, massive, fine-medium grained sandstone, with a patchy orange-brown staining due to iron oxidation (Plate 36). The sample comprises two irregular shaped clasts up to 140 mm diameter, with very uneven and pock-marked surfaces. The sandstone has been heavily bioturbated and evidence of burrows and borings are visible on the surfaces of the clasts. Some of the burrows / borings have been infilled with fine-grained muddy sediment and detrital bioclastic debris. Very minor encrustation by bryozoa is present.

Plate 36. Photograph of sample GT015. These are irregular shaped clasts which have been heavily bored by marine organisms. Field of view ~220 mm wide.

The polished thin section prepared from sample GT015 is shown in Plate 37. The sample is a predominantly fine sandstone, with patchy carbonate cementation. Numerous elliptical patches of fine-grained, dark brown, silty material are visible within the section, and represent cross-sections through silt-filled burrows. Detrital grains are angular to sub-angular, and dominated by quartz. The rock has an uncompacted, grain-supported fabric with long-edge edge and simple point grain contacts. Several rounded, detrital glauconite ("glauconie" *sensu lato*) grains are present. Detrital bioclasts were rarely observed in thin section, and where present are usually small foraminifera (<30 µm). There is little evidence of secondary porosity due to the dissolution of detrital grains or shell fragments in this sample.

The micritic cement comprises fine-grained magnesian calcite, and forms brownish, globular aggregates or "clots". A coarser halo of more crystalline micrite or microsparite lines the intergranular pore spaces around the grains and the micritic clots (Plate 38). Rare, acicular crystals of possible aragonite are occasionally present in the open pore spaces (although no aragonite was detected by XRD).

High resolution BSEM shows that the micrite cement is microporous, with a 'lacy' texture, which can also be seen in the micrite rims around detrital grains (Plate 39). This texture is similar to the

cellular microfabrics noted within sample GT112. These voids or cavities are about the size of bacterial cells (<2 µm), and may represent preserved bacterial cells around which the carbonate may have nucleated. These well-developed cellular microfabrics very closely resemble fossilised and mineralised bacterial cells described from experimental studies and other environments in the literature (c.f. Martill and Wilby, 1994; Wilby and Whyte, 1995).

Plate 37. Scanned image of sample GT015. Numerous cross sections of burrows, some infilled are visible. The sample has a patchy orange-brown staining due to finely disseminated iron oxyhydroxides. Field of view = 48 mm wide.

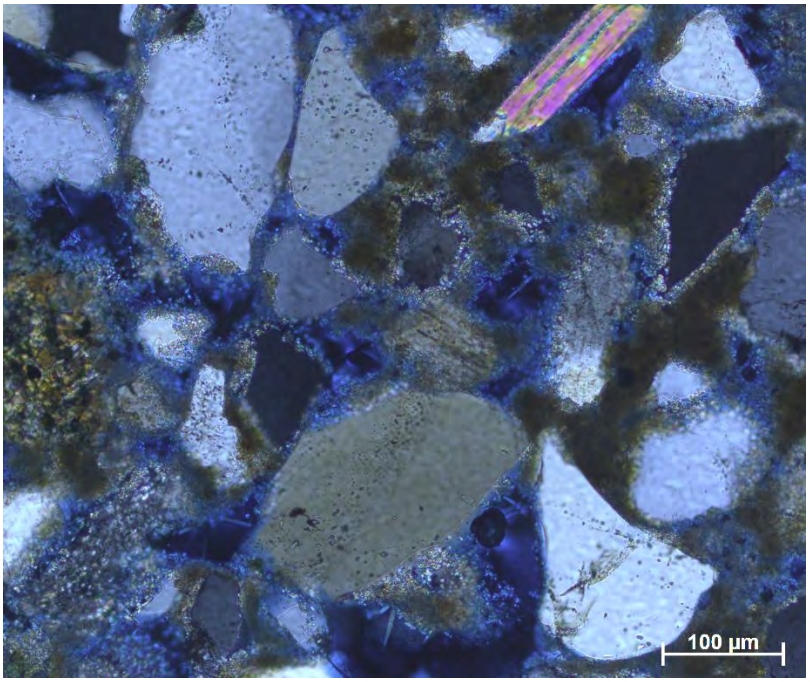

Plate 38. Transmitted light micrograph (crossed polarised light) showing halos of cement around grains and fine-grained micritic cement. Note the rare, acicular crystals within the cement (bottom centre of image). Sample GT015

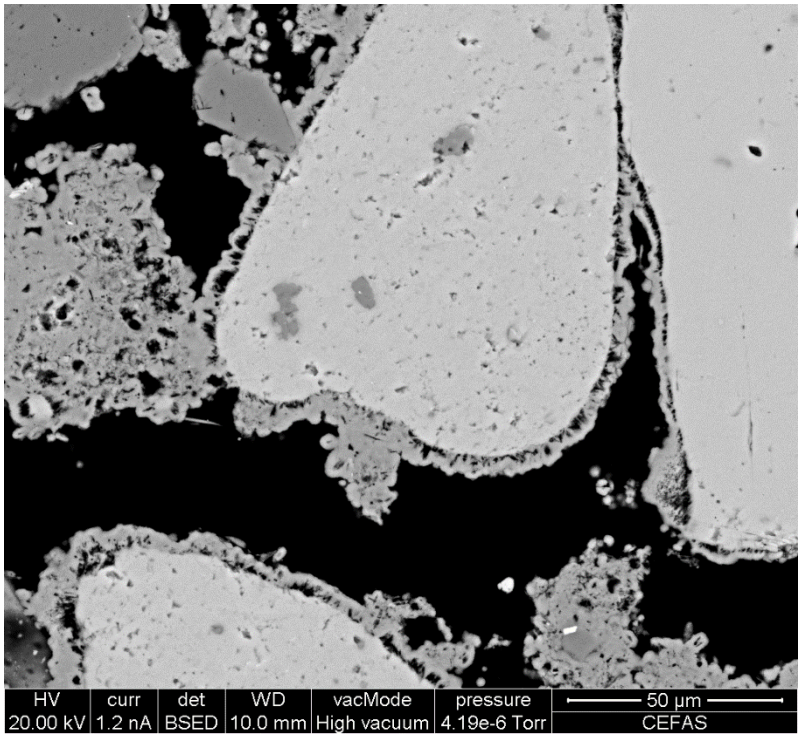

Plate 39. BSEM image showing the porous nature of the micrite. Note the rare acicular crystal protruding from the main micritic clot in the left of the image. Sample GT015

ED-EPMA analysis of the carbonate cements are presented in Table 10 and are summarised in Figure 10. The micritic magnesian calcite cements are very similar in composition and contain between 28 and 39 mole % $MgCO_3$ in solid solution (i.e. the structural formula of the calcite can be represented as $Ca_{0.61\text{-}0.72}Mg_{0.39\text{-}0.28}CO_3$). The rare acicular needles proved difficult to analyse due to their fine size: their analyses probably reflect contamination by surrounding matrix material. However, they are probably late stage aragonite (both analysis indicate the presence of Sr), and may represent the very early stages of an aragonite pore-filling cement such as observed in sample GT012 (e.g. Plate 25).

The sequence of sedimentary and post-depositional diagenetic events recorded from sample GT015 can be summarised as follows:

1. Deposition of medium-grained sand.
2. Syndepositional bioturbation and subsequent infill of burrows with silt.
3. Precipitation of micritic high-magnesian calcite within the near-surface of the sediment, causing lithification.
4. Late-stage, limited nucleation of aragonite cement in larger open pores.
5. Oxidation and staining by fine secondary iron oxyhydroxide.
6. Colonisation by bryozoa on the lithified surfaces.

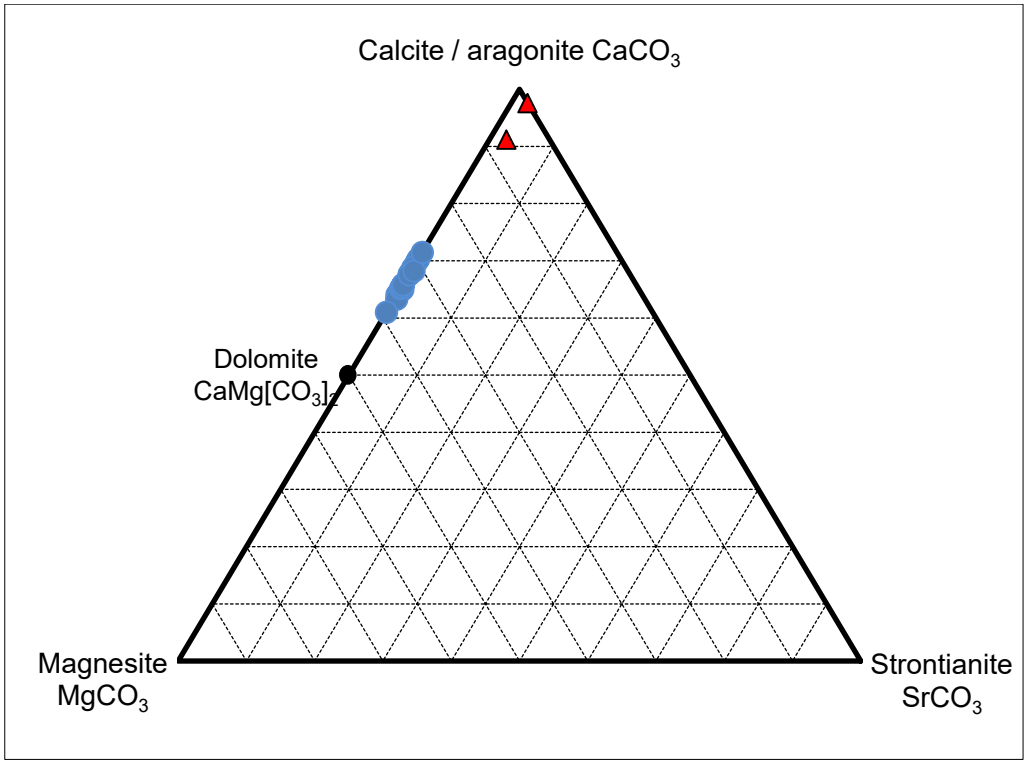

Figure 10. $CaCO_3$-$MgCO_3$-$SrCO_3$ molar ratio plot illustrating the compositions of the high-magnesian calcite micritic cement (solid blue circles), rare acicular crystals (solid red triangles) from sample GT015.

Table 10. Electron microprobe analyses of carbonate cements within sample GT015.

		Weight % oxide (normalised)							Ionic ratio [normalised to 3 [O]						COMMENTS
SAMPLE	No	MgO	CaO	MnO	FeO	SrO	CO_2 (calc)	*Total wt%	Mg^{2+}	Ca^{2+}	Mn^{2+}	Fe^{2+}	Sr^{2+}	CO_3^{2-}	
GT015	1	14.45	38.80	0.00	0.34	0.00	46.42	100	0.34	0.66	0.00	0.00	0.00	1.00	micrite
GT015	2	14.59	38.18	0.00	0.47	0.42	46.34	100	0.34	0.65	0.00	0.01	0.00	1.00	micrite
GT015	3	14.24	38.42	0.00	1.03	0.00	46.32	100	0.34	0.65	0.00	0.01	0.00	1.00	micrite
GT015	4	14.48	38.79	0.00	0.31	0.00	46.43	100	0.34	0.66	0.00	0.00	0.00	1.00	micrite
GT015	5	15.22	37.83	0.00	0.40	0.00	46.54	100	0.36	0.64	0.00	0.01	0.00	1.00	micrite
GT015	6	13.20	40.24	0.00	0.35	0.00	46.20	100	0.31	0.68	0.00	0.00	0.00	1.00	micrite
GT015	7	13.50	39.37	0.00	0.94	0.00	46.20	100	0.32	0.67	0.00	0.01	0.00	1.00	micrite
GT015	8	13.56	39.45	0.00	0.76	0.00	46.22	100	0.32	0.67	0.00	0.01	0.00	1.00	micrite
GT015	9	13.27	40.49	0.00	0.00	0.00	46.25	100	0.31	0.69	0.00	0.00	0.00	1.00	micrite
GT015	10	15.50	37.60	0.00	0.00	0.34	46.56	100	0.36	0.63	0.00	0.00	0.00	1.00	micrite
GT015	11	16.54	36.05	0.00	0.66	0.00	46.75	100	0.39	0.61	0.00	0.01	0.00	1.00	micrite
GT015	12	14.62	38.60	0.00	0.33	0.00	46.45	100	0.34	0.65	0.00	0.00	0.00	1.00	micrite
GT015	13	13.17	40.60	0.00	0.00	0.00	46.23	100	0.31	0.69	0.00	0.00	0.00	1.00	micrite
GT015	14	12.56	41.02	0.00	0.33	0.00	46.09	100	0.30	0.70	0.00	0.00	0.00	1.00	micrite
GT015	15	12.70	40.91	0.00	0.27	0.00	46.12	100	0.30	0.70	0.00	0.00	0.00	1.00	micrite
GT015	16	14.85	38.63	0.00	0.00	0.00	46.52	100	0.35	0.65	0.00	0.00	0.00	1.00	micrite
GT015	17	13.40	39.58	0.00	0.83	0.00	46.19	100	0.32	0.67	0.00	0.01	0.00	1.00	micrite
GT015	18	14.62	38.58	0.00	0.36	0.00	46.44	100	0.34	0.65	0.00	0.00	0.00	1.00	micrite
GT015	19	12.46	41.20	0.00	0.27	0.00	46.08	100	0.30	0.70	0.00	0.00	0.00	1.00	micrite
GT015	20	14.49	38.83	0.00	0.25	0.00	46.43	100	0.34	0.66	0.00	0.00	0.00	1.00	micrite
GT015	21	12.48	41.21	0.00	0.22	0.00	46.09	100	0.30	0.70	0.00	0.00	0.00	1.00	micrite
GT015	22	13.03	40.10	0.00	0.73	0.00	46.14	100	0.31	0.68	0.00	0.01	0.00	1.00	micrite
GT015	23	13.58	39.45	0.00	0.74	0.00	46.23	100	0.32	0.67	0.00	0.01	0.00	1.00	micrite
GT015	24	13.12	39.80	0.00	0.58	0.42	46.08	100	0.31	0.68	0.00	0.01	0.00	1.00	micrite
GT015	25	11.95	41.75	0.00	0.31	0.00	45.99	100	0.28	0.71	0.00	0.00	0.00	1.00	micrite
GT015	26	0.00	53.66	0.00	0.47	2.44	43.43	100	0.00	0.97	0.00	0.01	0.02	1.00	cross section of acicular crystal
GT015	27	2.47	49.85	0.00	1.41	2.52	43.75	100	0.06	0.89	0.00	0.02	0.02	1.00	thin acicular crystal

**Note: Some analytical totals were low (<90%) because of the microporous nature of the cements. Therefore all data were normalised to 100%*

4.8 SAMPLE GT024

This sample comprises two irregular shaped, buff coloured clasts (<60 mm diameter), of fine-grained sandstone (Plate 40). Minor orange-brown staining caused by the presence of iron oxyhydroxides. There are no obvious laminations or sedimentary structures within the clasts. The surfaces have an irregular topography with some borings infilled with loosely cemented, slightly coarser sandstone. Some minor bioclastic debris is present on the surface.

Plate 40. Photograph of sample GT024 which comprises two buff coloured, irregular shaped clasts up to 60 mm diameter. Field of view ~140 mm wide.

The polished thin section prepared from sample GT024 is shown in Plate 24. The sample is relatively dense and compacted compared to previous samples. The sample is moderately well-sorted, very fine sandstone, with sub-angular to sub-rounded detrital grains. The sand is quartz dominated, with minor feldspar (<10%). Evidence of secondary porosity is rare, although there are traces of oversized pores where detrital grains have been dissolved out. The intergranular micritic matrix cement has a patchy, dark brown appearance where it has been stained by iron oxyhydroxides, and in transmitted light some of the matrix cement displays a “polka-dot” or “frogspawn-like” appearance imparted by the presence of very fine spherical opaque minerals (Plate 42). The micrite is generally finer grained adjacent to the detrital grain surfaces and with a brown colouration. However, it may be overgrown by a thin film or rim of more birefringent and slightly coarser micrite or microsparite cement (Plate 43).

High resolution BSEM observations show that the micritic high magnesian calcite matrix or cement, corresponding to the fine-grained brown-coloured micrite observed in optical microscopy, is mixed with patches of clay and silica-rich material (Plate 44). This “patchy” or fabric is typical of heterogeneity caused by bioturbation. In cleaner areas of sand, the micrite has formed as coarser euhedral calcite rhombs (Plate 45: corresponding to the brighter birefringence observed in Plate 43). The idiomorphic rhombic calcite may result from the recrystallization and coarsening up of finer micrite particles. There is some evidence for the preservation of well-developed cellular

microfabrics, (as discussed in other samples, e.g.: GT004, GT007). Numerous framboidal clusters and discrete spheroidal crystals of iron oxyhydroxide are present throughout the sample, particularly within the clay-rich micrite. These may represent pseudomorphs formed after the oxidation of early diagenetic framboidal pyrite (which has a similar morphology). The framboidal pyrite would originally have formed under reducing conditions, and is commonly associate with early diagenetic microbial breakdown of organic material (cf. Berner, 1969, 1980). Pyrite formation would indicate that the authigenic magnesian calcite also formed under reducing porewater conditions.

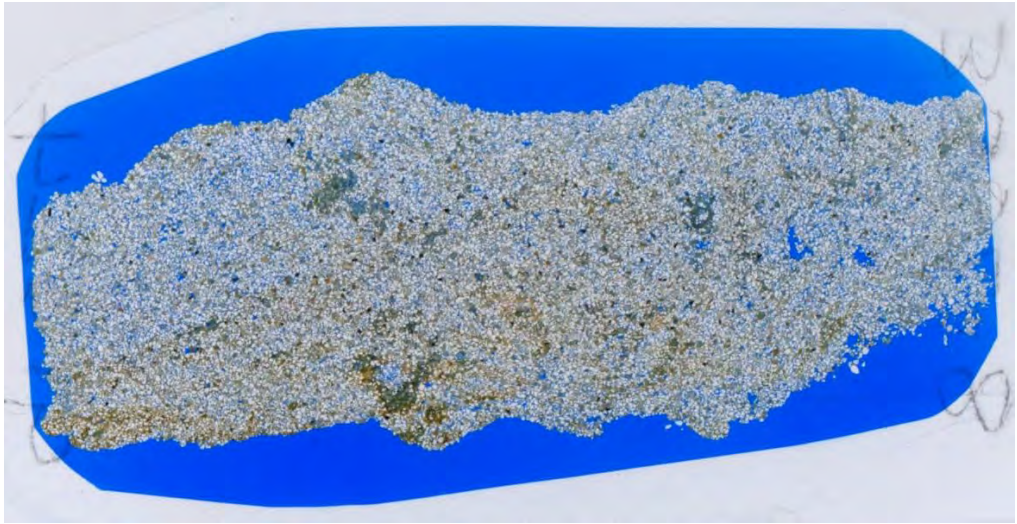

Plate 41. Scan of the thin section prepared from sample GT024. Field of view = 48 mm wide.

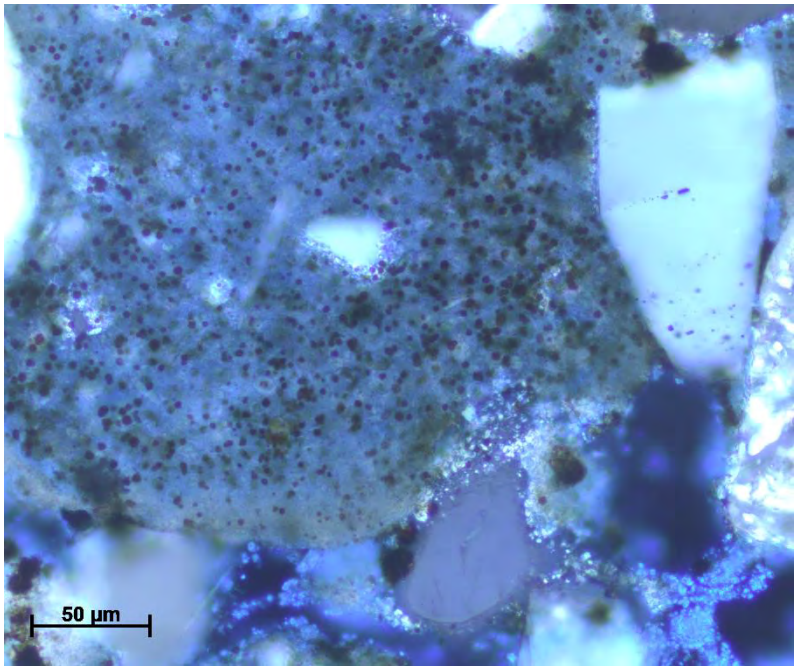

Plate 42. Transmitted light photomicrograph (cross polarised light) showing the polka-dot texture in the micritic magnesian calcite cement from the inclusion of abundant opaque iron oxyhydroxides possibly pseudomorphing earlier diagenetic pyrite. GT024

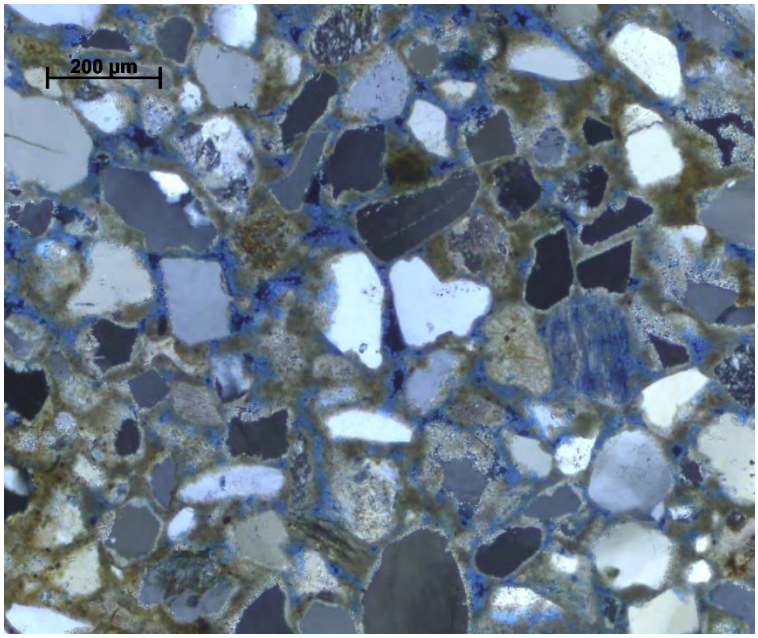

Plate 43. Transmitted light photomicrograph (cross polarised light) showing the fine-grained, brown coloured micrite around the grains and the halo of cement with brighter birefringence. GT024

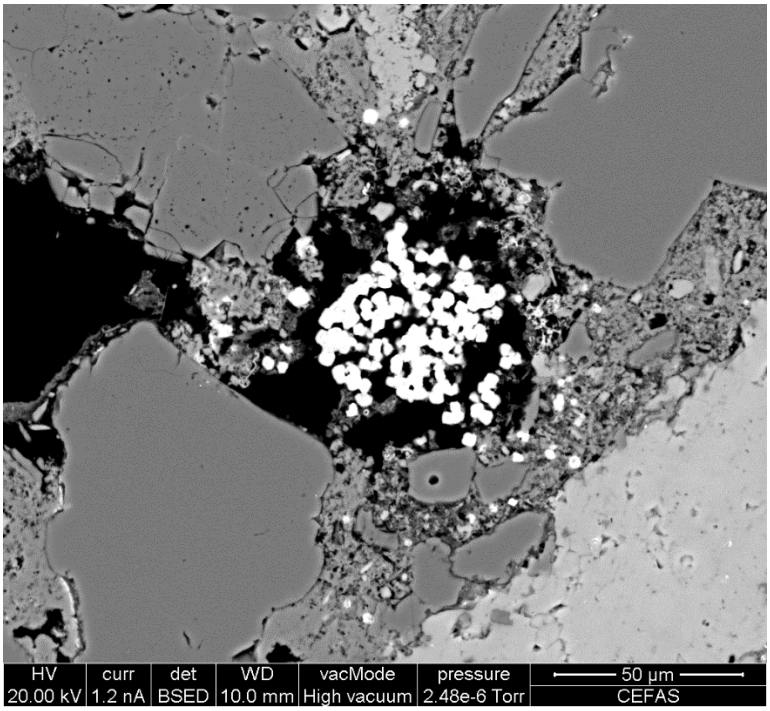

Plate 44. BSEM image showing framboidal iron oxide (bright) within a pore space. These are probably pseudomorphs after early diagenetic pyrite. The micrite in this image is clay/silica rich. GT024

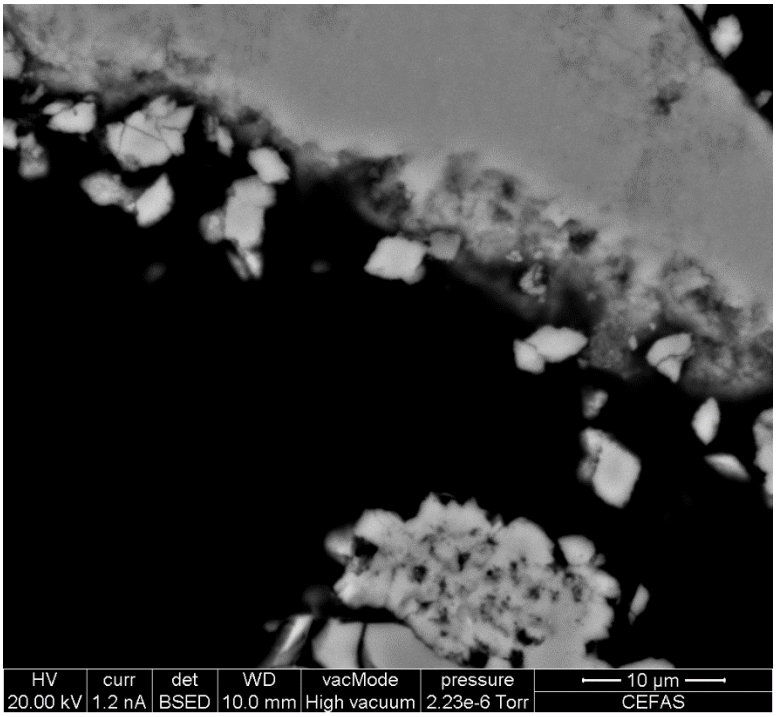

Plate 45. BSEM image showing an area of 'cleaner' cement, i.e. low clay portion. Here the micrite has formed euhedral rhombs of high magnesian calcite. GT024

ED-EPMA analysis of the carbonate cements are presented in Table 11 and are summarised in Figure 11. The micritic and coarser microsparite magnesian calcite cements are very similar in composition, and contain between 33 and 43 mole % $MgCO_3$ in solid solution (i.e. the structural formula of the calcite can be represented as $Ca_{0.57-0.67}Mg_{0.43-0.33}CO_3$).

XRD analysis definitively identified the presence of significant dolomite (14.7%) in this sample (Table 2). However, pure end member dolomite was not identified by ED-EPMA (Figure 11). It is likely that at least some of the euhedral rhombs identified by BSEM imaging may be "excess-calcium dolomites" but that such dolomite and very highly-magnesium-substituted calcite may be indistinguishable by BSEM (see further detailed discussion in Section 3).

Shell fragments were also analysed by ED-EPMA and have <2 mole % $MgCO_3$ in solid solution, with no detectable Sr.

The sequence of sedimentary and post-depositional diagenetic events recorded from sample GT024 can be summarised as follows:

1. Deposition of fine sand.
2. Some syndepositional bioturbation.
3. Microbial precipitation of micritic high-magnesian calcite within the near-surface of the sediment, causing lithification.
4. Precipitation of framboidal pyrite coeval with high-magnesian calcite.
5. Oxidation of framboidal pyrite and precipitation of secondary iron oxyhydroxide.

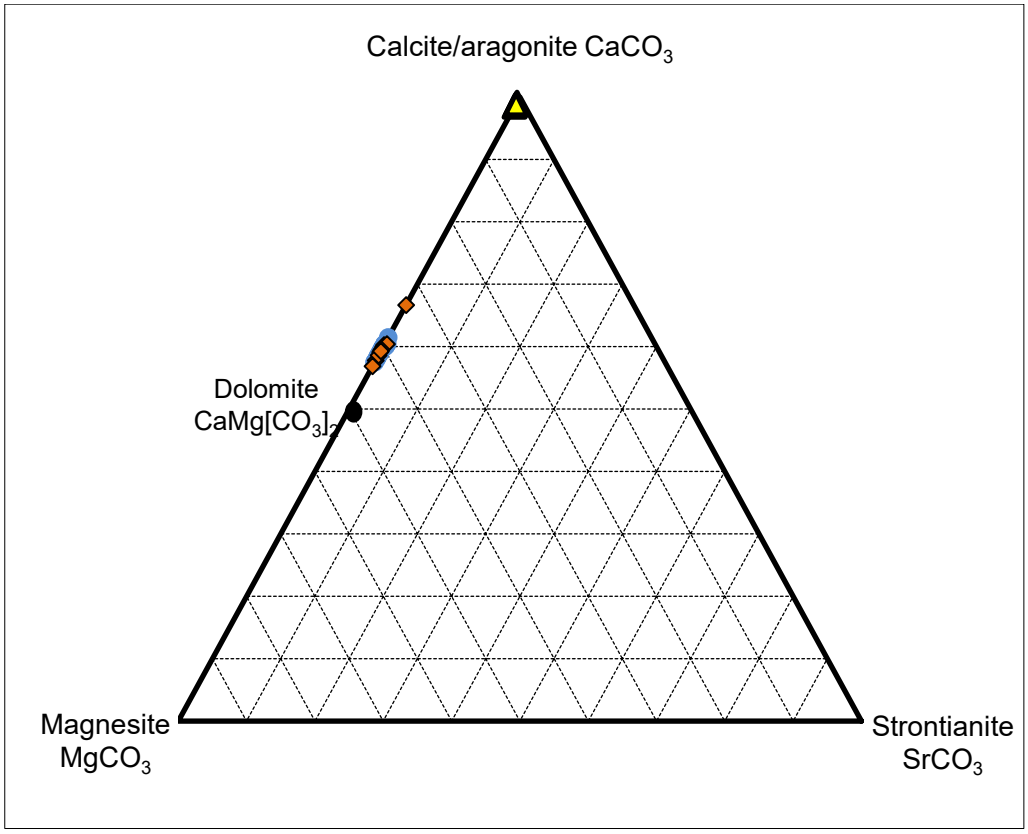

Figure 11. $CaCO_3$-$MgCO_3$-$SrCO_3$ molar ratio plot illustrating the compositions of some shell fragments (yellow triangles), the high-magnesian calcite micritic cement (solid blue circles), and a micritic lining from the inside of shell cavities (orange diamonds) from sample GT024.

Table 11. Electron microprobe analyses of shelly fragments and micritic cements in sample GT024.

		Weight % oxide (normalised)							Ionic ratio [normalised to 3 [O]						COMMENTS
SAMPLE	No	MgO	CaO	MnO	FeO	SrO	CO_2 (calc)	*Total wt%	Mg^{2+}	Ca^{2+}	Mn^{2+}	Fe^{2+}	Sr^{2+}	CO_3^{2-}	
GT024	1	0.62	54.69	0.00	0.68	0.00	44.01	100	0.02	0.98	0.00	0.01	0.00	1.00	shell
GT024	2	0.55	54.95	0.00	0.48	0.00	44.01	100	0.01	0.98	0.00	0.01	0.00	1.00	shell
GT024	3	0.34	55.35	0.00	0.32	0.00	43.99	100	0.01	0.99	0.00	0.00	0.00	1.00	shell
GT024	4	0.44	55.11	0.00	0.45	0.00	44.00	100	0.01	0.98	0.00	0.01	0.00	1.00	shell
GT024	5	0.45	55.50	0.00	0.00	0.00	44.04	100	0.01	0.99	0.00	0.00	0.00	1.00	shell
GT024	6	17.58	35.43	0.00	0.00	0.00	46.99	100	0.41	0.59	0.00	0.00	0.00	1.00	micritic lining of shell (inner)
GT024	7	17.20	35.87	0.00	0.00	0.00	46.92	100	0.40	0.60	0.00	0.00	0.00	1.00	micritic lining of shell (inner)
GT024	8	14.16	39.44	0.00	0.00	0.00	46.40	100	0.33	0.67	0.00	0.00	0.00	1.00	micritic lining of shell (inner)
GT024	9	17.07	36.03	0.00	0.00	0.00	46.90	100	0.40	0.60	0.00	0.00	0.00	1.00	micritic lining of shell (inner)
GT024	10	18.20	34.71	0.00	0.00	0.00	47.09	100	0.42	0.58	0.00	0.00	0.00	1.00	micritic lining of shell (inner)
GT024	11	18.64	34.19	0.00	0.00	0.00	47.17	100	0.43	0.57	0.00	0.00	0.00	1.00	micritic lining of shell (inner)
GT024	12	16.82	36.05	0.00	0.00	0.35	46.79	100	0.39	0.60	0.00	0.00	0.00	1.00	micritic lining of shell (inner)
GT024	13	17.41	35.63	0.00	0.00	0.00	46.96	100	0.40	0.60	0.00	0.00	0.00	1.00	micritic lining of shell (inner)
GT024	14	17.82	35.15	0.00	0.00	0.00	47.03	100	0.41	0.59	0.00	0.00	0.00	1.00	micritic lining of shell (inner)
GT024	15	17.45	35.35	0.00	0.26	0.00	46.94	100	0.41	0.59	0.00	0.00	0.00	1.00	micritic lining of shell (inner)
GT024	16	17.56	35.45	0.00	0.00	0.00	46.99	100	0.41	0.59	0.00	0.00	0.00	1.00	micrite
GT024	17	16.99	36.12	0.00	0.00	0.00	46.89	100	0.40	0.60	0.00	0.00	0.00	1.00	micrite
GT024	18	17.60	35.41	0.00	0.00	0.00	46.99	100	0.41	0.59	0.00	0.00	0.00	1.00	micrite
GT024	19	17.35	35.70	0.00	0.00	0.00	46.95	100	0.40	0.60	0.00	0.00	0.00	1.00	micrite
GT024	20	16.90	35.85	0.00	0.42	0.00	46.83	100	0.39	0.60	0.00	0.01	0.00	1.00	micrite
GT024	21	17.29	35.78	0.00	0.00	0.00	46.94	100	0.40	0.60	0.00	0.00	0.00	1.00	micrite
GT024	22	17.32	35.73	0.00	0.00	0.00	46.94	100	0.40	0.60	0.00	0.00	0.00	1.00	micrite
GT024	23	17.37	35.47	0.00	0.23	0.00	46.93	100	0.40	0.59	0.00	0.00	0.00	1.00	micrite
GT024	24	17.29	35.77	0.00	0.00	0.00	46.94	100	0.40	0.60	0.00	0.00	0.00	1.00	micrite
GT024	25	17.97	34.60	0.20	0.22	0.00	47.01	100	0.42	0.58	0.00	0.00	0.00	1.00	micrite
GT024	26	16.91	35.96	0.00	0.29	0.00	46.84	100	0.39	0.60	0.00	0.00	0.00	1.00	micrite
GT024	27	16.99	35.84	0.00	0.00	0.36	46.81	100	0.40	0.60	0.00	0.00	0.00	1.00	micrite
GT024	28	16.77	36.05	0.00	0.00	0.42	46.76	100	0.39	0.60	0.00	0.00	0.00	1.00	micrite
GT024	29	17.89	33.66	0.26	1.30	0.00	46.89	100	0.42	0.56	0.00	0.02	0.00	1.00	micrite
GT024	30	17.75	35.23	0.00	0.00	0.00	47.02	100	0.41	0.59	0.00	0.00	0.00	1.00	micrite
GT024	31	17.08	36.02	0.00	0.00	0.00	46.90	100	0.40	0.60	0.00	0.00	0.00	1.00	micrite
GT024	32	17.93	35.03	0.00	0.00	0.00	47.05	100	0.42	0.58	0.00	0.00	0.00	1.00	micrite

		Weight % oxide (normalised)							Ionic ratio [normalised to 3 [O]						COMMENTS
SAMPLE	No	MgO	CaO	MnO	FeO	SrO	CO_2 (calc)	*Total wt%	Mg^{2+}	Ca^{2+}	Mn^{2+}	Fe^{2+}	Sr^{2+}	CO_3^{2-}	
GT024	33	17.59	35.24	0.00	0.20	0.00	46.97	100	0.41	0.59	0.00	0.00	0.00	1.00	micrite
GT024	34	17.89	35.07	0.00	0.00	0.00	47.04	100	0.42	0.58	0.00	0.00	0.00	1.00	micrite
GT024	35	18.21	34.49	0.00	0.22	0.00	47.08	100	0.42	0.57	0.00	0.00	0.00	1.00	micrite
GT024	36	16.40	36.47	0.00	0.38	0.00	46.75	100	0.38	0.61	0.00	0.01	0.00	1.00	micrite

**Note: Some analytical totals were low (<90%) because of the microporous nature of the cements. Therefore all data were normalised to 100%*

4.9 SAMPLE GT025.

This sample comprised eight, highly irregular and angular clasts up to 120 mm in diameter (Plate 46). They are buff coloured, fine to medium grained sandstone that has been heavily bioturbated. Numerous shell fragments have been incorporated into the sample, and calcareous serpulid worm encrustations are visible on the surfaces (Plate 47).

Plate 46. Photograph showing the highly bioturbated, irregular shaped clasts which comprise sample GT025. Numerous encrustations of bryozoan and calcareous serpulid casts are visible. Field of view ~240 mm wide.

Plate 47. Optical micrograph detailing some calcareous serpulid worm encrustations on the surface of a clast from sample GT025.

The polished thin section prepared through one of the clasts of sample GT025 is shown in Plate 48. Part of the sample has a strong orange-brown colouration where the cement and grain surfaces have been stained orange-brown by iron oxyhydroxides. The thin section displays several elliptical voids that represent cross-sections through burrows both within the sample and exposed on the surface. The sand grains around the walls of the "surface burrows" are only weakly cemented, and thus have a higher intergranular porosity than the underlying sediment. These structures are unaffected by the orange-brown colouration, indicating these features were constructed after the oxidative alteration of the matrix in the underlying sandstone. Very fine and delicate calcareous "barb-like" structures are present around the edge of the sample (Plate 49) and appear to have some internal structure that is just discernable in transmitted light. These enigmatic structures may be a type of marine flora which has colonised the surface of the clast but it could not be identified here.

The sample is dominated by detrital quartz sand grains. The grains are angular to sub-angular, ranging from fine to medium grained (<450 µm) sand, and are close-packed but with little compactional deformation. Several rounded, detrital glauconite ("glauconie" *sensu lato*) are present (<250 µm). Minor secondary framework grain dissolution porosity has developed where former unstable detrital minerals have dissolved away. The sample is well-cemented with a fine-grained, brown coloured semi-opaque patchy micritic carbonate cement (Plate 48). Rounded micritic pelloids (<500 µm) are common (Plate 50) and probably represent faecal pellets.

High resolution BSEM show that the matrix of the sandstone is a microporous micritic high-magnesian cement, comprising spherical to micro-boytryoidal aggregates of micro- to nanocrystalline calcite (Plate 51). Light/dark zoning backscattered contrast is visible under BSEM within some of the micrite, indicating the micrite becomes progressively more Mg-rich away from the grain surface and towards the adjacent pore space (Plate 52). Aragonite "dog-tooth" rims are present as a minor cement around some grains within the more open porosity (Plate 52). It has grown on top of the micritic magnesian calcite and is therefore paragenetically later.

An iron oxyhydroxide cement has infilled some of the pore spaces (Plate 51) and formed after the precipitation of the micrite, which it encloses. Colloform, fibrous manganese oxyhydroxide precipitates are also found in this section (Plate 53).

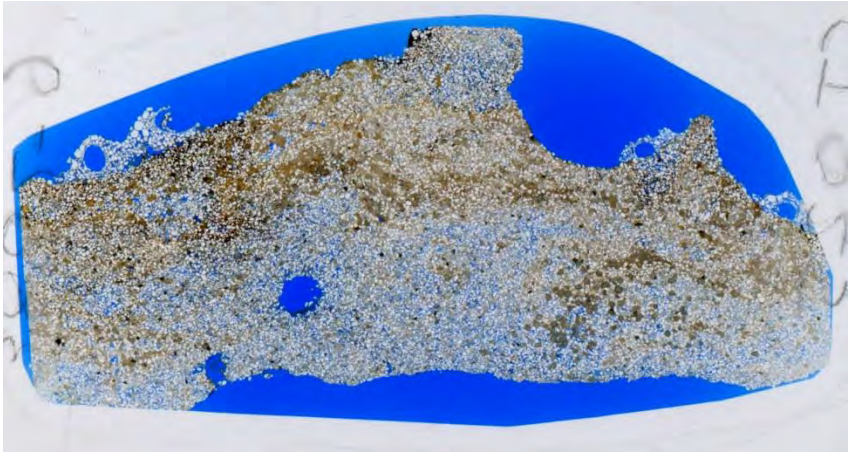

Plate 48. Scanned image of the thin section prepared from one of the clasts comprising sample GT025. Elliptical cross-sections of exposed burrows are visible, both within and on the surface of the sample. In the image above, the upper part of the sample has a strong orange-brown colouration from Fe-oxyhydroxide staining. Field of view = 48 mm wide.

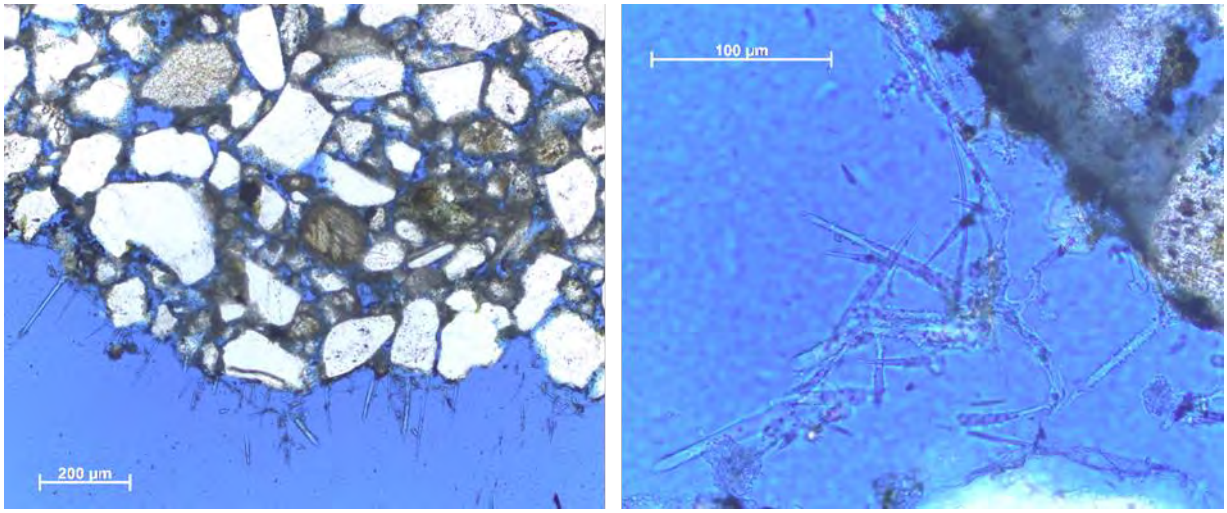

Plate 49. Transmitted light photomicrographs (plain polarised light) showing of calcareous barbs or thorn-type structures coating the edge of the sample. GT025

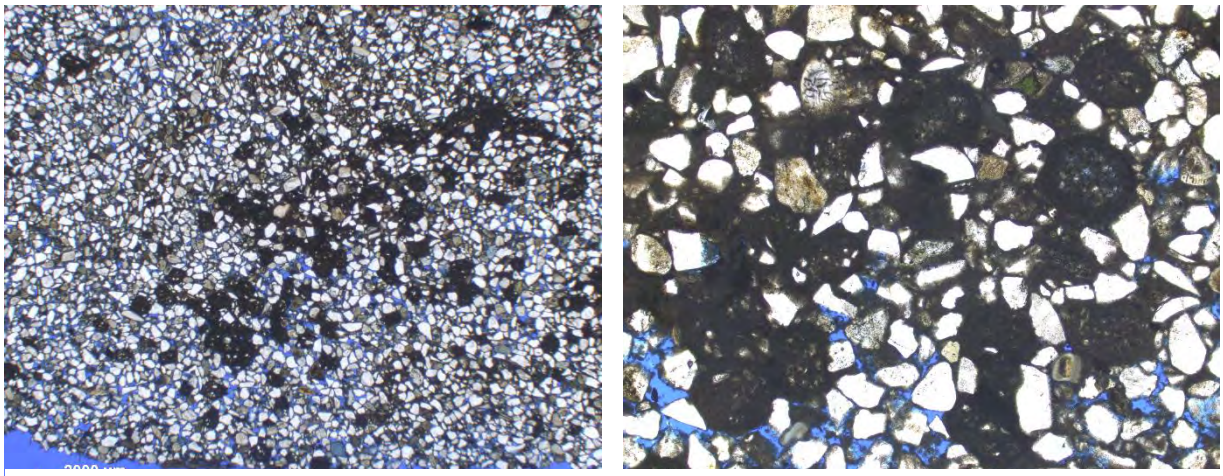

Plate 50. Transmitted light photomicrographs (plain polarised light) showing numerous micrite pelloids within the sample. GT025.

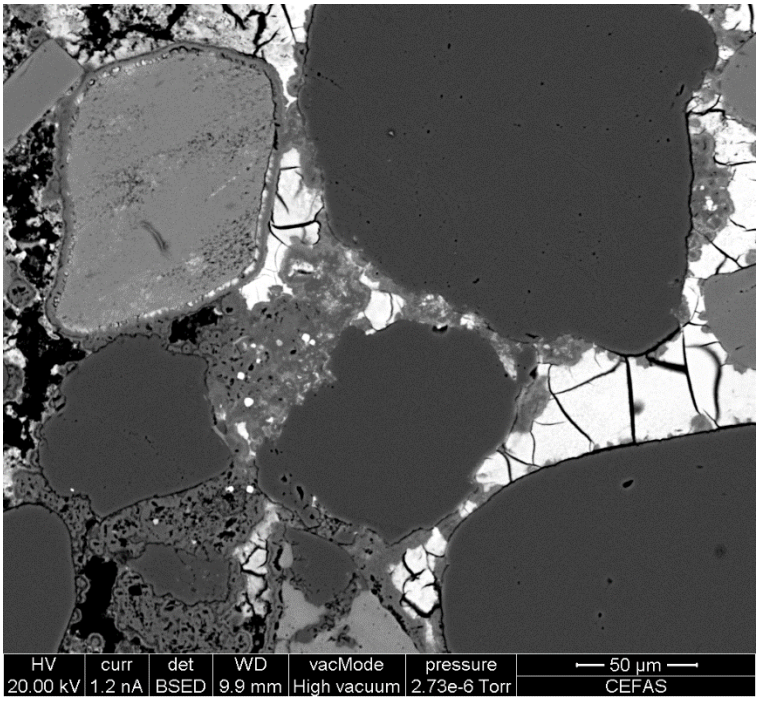

Plate 51. BSEM image showing the microporous and globular aggregates of micritic high-magnesian calcite (mid-grey), and a late-stage, pore-infilling, iron oxyhydroxide cement (white) with desiccation cracks. Sample GT025

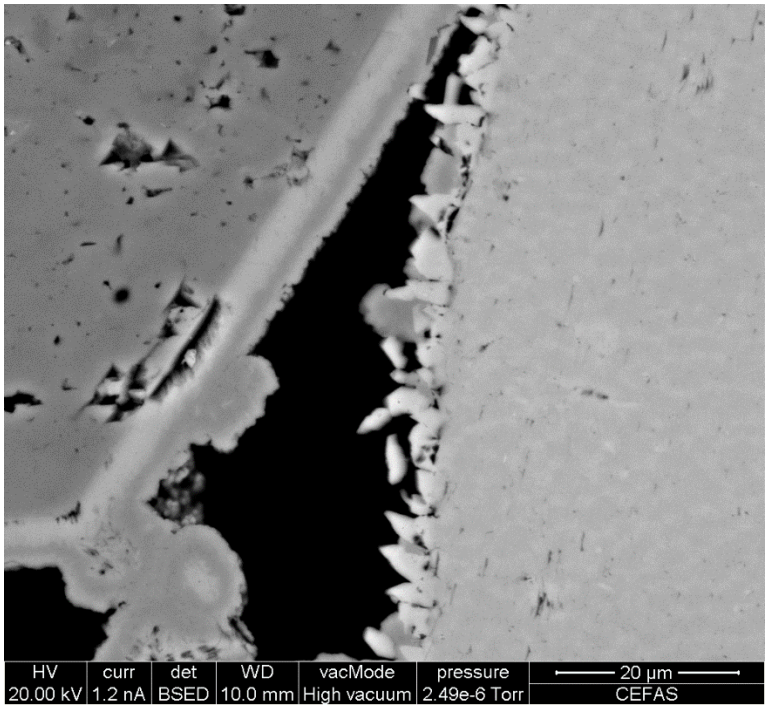

Plate 52. BSEM image detailing on the left a relict, high-magnesian calcite grain (possible clast of earlier-formed MDAC) with a banded micritic magnesian calcite rim (mid-grey): the inner rim is more Ca-rich, and the outer rim has a higher Mg content. The grain on the right-hand side of the image has a "dog-tooth" rim of aragonite (white). Sample GT025

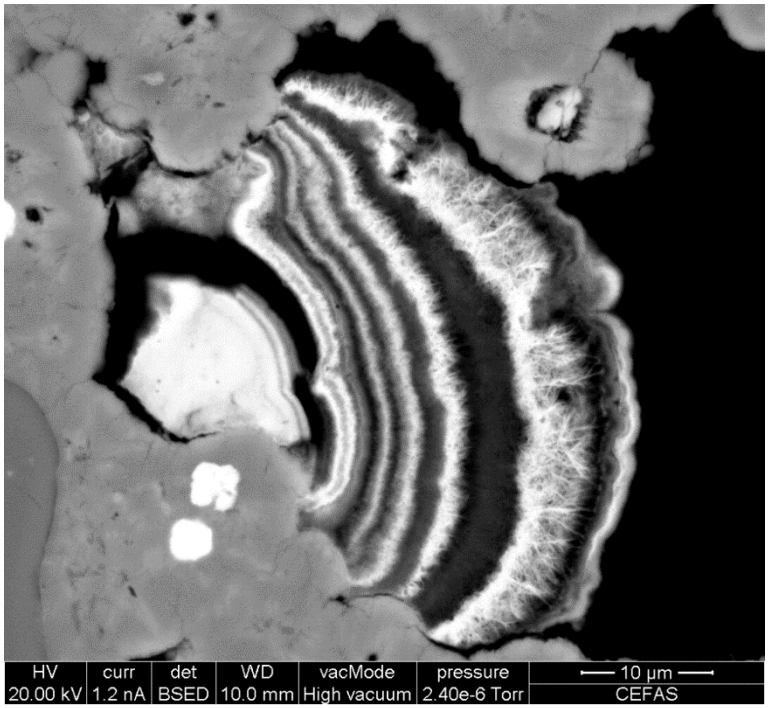

Plate 53. BSEM image showing colloform manganese oxyhydroxide precipitated on top of micritic high magnesian calcite cement. Sample GT025.

ED-EPMA analysis of the carbonate cements are presented in Table 12 and are summarised in Figure 12 and Figure 13. The micritic magnesian calcite cements (Figure 12) show a wide-range in composition and contain between 12 and 38 mole % $MgCO_3$ in solid solution (i.e. the structural formula of the calcite can be represented as $Ca_{0.88-0.62}Mg_{0.12-0.38}CO_3$). This is consistent with the XRD results (Table 2). The zoned micrite rims show a distinct difference in composition (Figure 13): the darker micrite containing between 30 to 39 mole % $MgCO_3$, and the lighter micrite rim containing 11 and 12 mole % $MgCO_3$ in solid solution. A relict high-magnesian calcite lithic grain was found to contain 38-46 mole % $MgCO_3$, placing the analyses with the highest Mg content very close to the ideal dolomite end-member. However, no dolomite was detected in this sample by XRD (Table 2). This lithic clast may be a relict lithic fragment derived from reworking of earlier MDAC material.

The aragonite dog-tooth rims are strontium bearing, with 1-2 mole % $SrCO_3$ in solid-solution (Figure 13) (i.e. the structural formula of the aragonite can be represented as $Ca_{0.98-1.00}Sr_{0.02-0.00}CO_3$). As discussed previously (see Section 4.5), the prismatic morphology, the relatively high Sr content suggests that this carbonate rim is aragonite rather than calcite

The sequence of sedimentary and post-depositional diagenetic events recorded from sample GT025 can be summarised as follows:

1. Deposition of fine to medium grained sandy sediment, detrital marine biota debris and faecal pellets.
2. Syndepositional bioturbation.
3. Precipitation of micritic high-magnesian calcite cement causing lithification.
4. Precipitation of traces of later aragonite cement.
5. Erosion and abrasion of the sample. Boring of the clast surfaces by marine biota.
6. Oxidative alteration and precipitation of colloidal manganese and iron oxyhydroxides.
7. Further colonisation of the clast surfaces by marine fauna and flora, and calcareous worm/serpulid encrustations on the lithified surface of the clast.

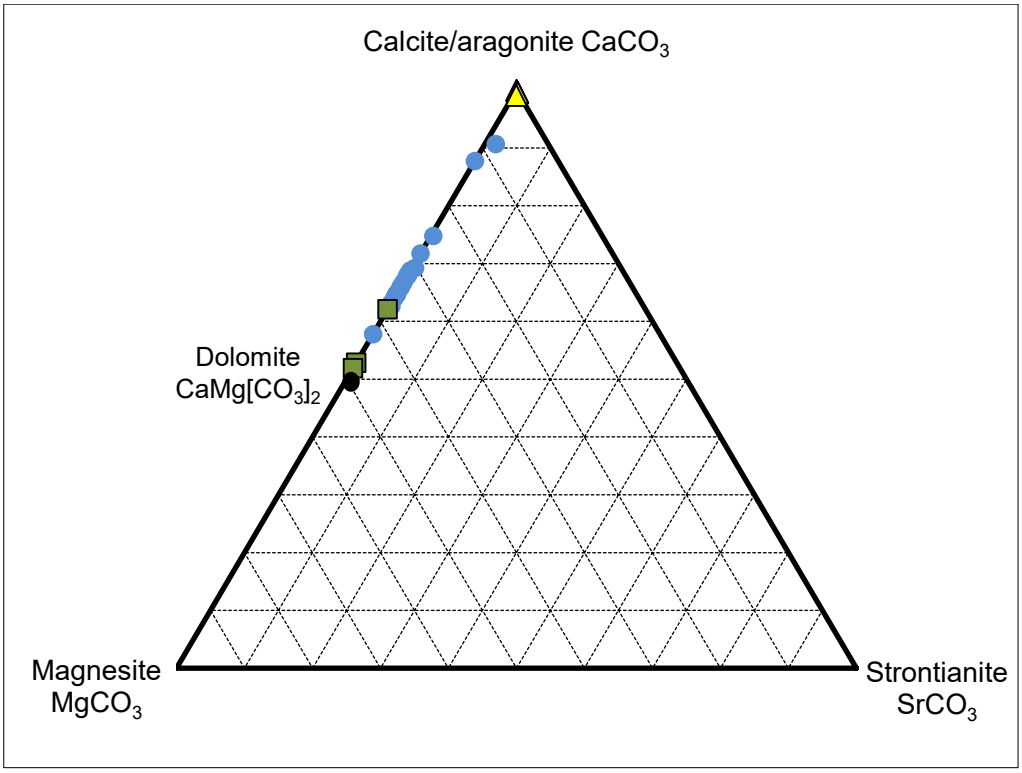

Figure 12. $CaCO_3$-$MgCO_3$-$SrCO_3$ molar ratio plot illustrating the compositions of the high-magnesian calcite micritic cement (solid blue circles), the high-Mg relict grain (green squares), and shell fragments (yellow triangles) from sample GT025.

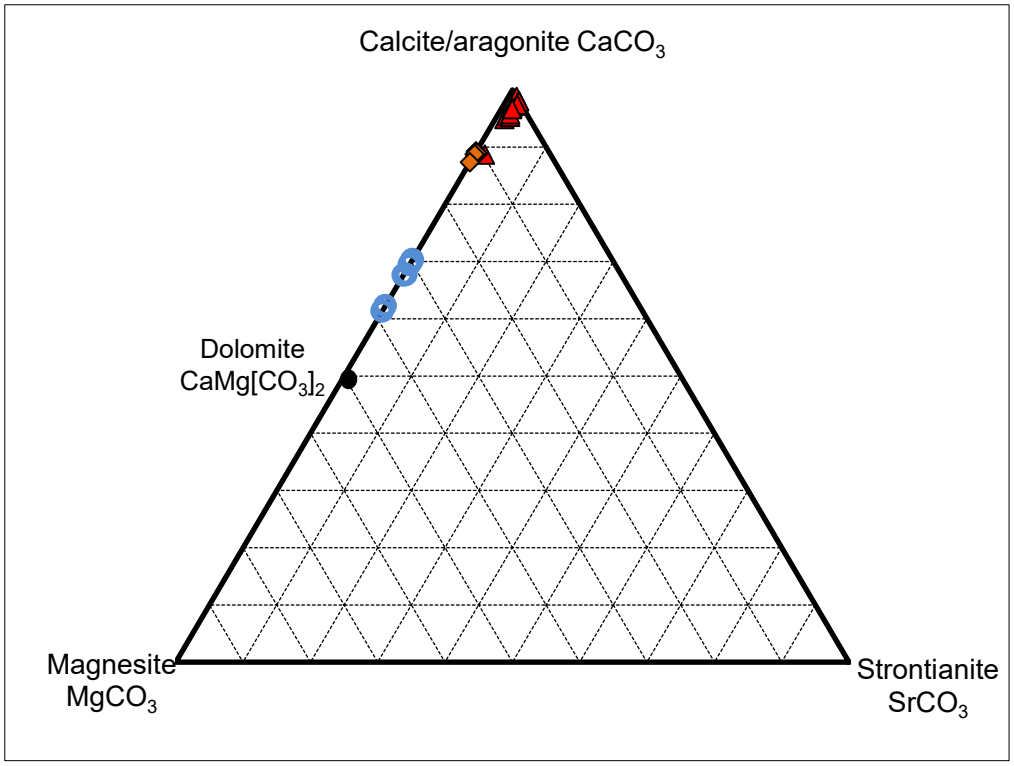

Figure 13. $CaCO_3$-$MgCO_3$-$SrCO_3$ molar ratio plot illustrating the compositions of the outer rim of high-magnesian calcite micritic cement (open blue circles), the lower-Mg, inner micrite rim (orange diamonds), and aragonite dog-tooth rims (red triangles) from sample GT025.

Table 12. Electron microprobe analyses of carbonate cements and grains from sample GT025.

		Weight % oxide (normalised)							Ionic ratio [normalised to 3 [O]						COMMENTS
SAMPLE	No	MgO	CaO	MnO	FeO	SrO	CO_2 (calc)	*Total wt%	Mg^{2+}	Ca^{2+}	Mn^{2+}	Fe^{2+}	Sr^{2+}	CO_3^{2-}	
GT025	1	4.35	49.98	0.64	0.00	0.48	44.56	100	0.11	0.88	0.01	0.00	0.00	1.00	bright rim along crystal edge
GT025	2	4.35	50.16	0.63	0.23	0.00	44.63	100	0.11	0.88	0.01	0.00	0.00	1.00	bright rim along crystal edge
GT025	3	4.34	50.07	0.70	0.00	0.30	44.59	100	0.11	0.88	0.01	0.00	0.00	1.00	bright rim along crystal edge
GT025	4	4.55	49.98	0.80	0.00	0.00	44.67	100	0.11	0.88	0.01	0.00	0.00	1.00	bright rim along crystal edge
GT025	5	5.10	49.13	0.74	0.28	0.00	44.75	100	0.12	0.86	0.01	0.00	0.00	1.00	bright rim along crystal edge
GT025	6	12.91	40.91	0.00	0.00	0.00	46.18	100	0.31	0.69	0.00	0.00	0.00	1.00	dark outer rim along crystal edge
GT025	7	13.73	39.95	0.00	0.00	0.00	46.33	100	0.32	0.68	0.00	0.00	0.00	1.00	dark outer rim along crystal edge
GT025	8	12.55	41.33	0.00	0.00	0.00	46.12	100	0.30	0.70	0.00	0.00	0.00	1.00	dark outer rim along crystal edge
GT025	9	13.52	39.90	0.00	0.00	0.36	46.22	100	0.32	0.68	0.00	0.00	0.00	1.00	dark outer rim along crystal edge
GT025	10	12.64	41.22	0.00	0.00	0.00	46.14	100	0.30	0.70	0.00	0.00	0.00	1.00	dark outer rim along crystal edge
GT025	11	16.16	37.10	0.00	0.00	0.00	46.74	100	0.38	0.62	0.00	0.00	0.00	1.00	dark outer rim along crystal edge
GT025	12	16.57	36.62	0.00	0.00	0.00	46.81	100	0.39	0.61	0.00	0.00	0.00	1.00	dark outer rim along crystal edge
GT025	13	16.23	37.01	0.00	0.00	0.00	46.76	100	0.38	0.62	0.00	0.00	0.00	1.00	grain (relict MDAC?)
GT025	14	19.59	30.58	0.41	2.35	0.00	47.07	100	0.45	0.51	0.01	0.03	0.00	1.00	grain (relict MDAC?)
GT025	15	20.05	30.12	0.42	2.25	0.00	47.16	100	0.46	0.50	0.01	0.03	0.00	1.00	grain (relict MDAC?)
GT025	16	15.86	37.45	0.00	0.00	0.00	46.69	100	0.37	0.63	0.00	0.00	0.00	1.00	micrite
GT025	17	15.06	38.38	0.00	0.00	0.00	46.56	100	0.35	0.65	0.00	0.00	0.00	1.00	micrite
GT025	18	10.39	43.53	0.00	0.00	0.42	45.67	100	0.25	0.75	0.00	0.00	0.00	1.00	micrite
GT025	19	13.66	40.03	0.00	0.00	0.00	46.31	100	0.32	0.68	0.00	0.00	0.00	1.00	micrite
GT025	20	13.47	40.24	0.00	0.00	0.00	46.28	100	0.32	0.68	0.00	0.00	0.00	1.00	micrite
GT025	21	5.01	49.85	0.35	0.00	0.00	44.79	100	0.12	0.87	0.00	0.00	0.00	1.00	micrite
GT025	22	14.97	38.49	0.00	0.00	0.00	46.54	100	0.35	0.65	0.00	0.00	0.00	1.00	micrite
GT025	23	18.21	34.69	0.00	0.00	0.00	47.10	100	0.42	0.58	0.00	0.00	0.00	1.00	micrite
GT025	24	14.50	39.04	0.00	0.00	0.00	46.46	100	0.34	0.66	0.00	0.00	0.00	1.00	micrite
GT025	25	15.07	38.10	0.00	0.31	0.00	46.53	100	0.35	0.64	0.00	0.00	0.00	1.00	micrite
GT025	26	15.70	37.43	0.00	0.22	0.00	46.64	100	0.37	0.63	0.00	0.00	0.00	1.00	micrite
GT025	27	14.43	38.89	0.00	0.26	0.00	46.42	100	0.34	0.66	0.00	0.00	0.00	1.00	micrite
GT025	28	13.46	40.07	0.00	0.21	0.00	46.26	100	0.32	0.68	0.00	0.00	0.00	1.00	micrite
GT025	29	14.96	38.32	0.00	0.20	0.00	46.52	100	0.35	0.65	0.00	0.00	0.00	1.00	micrite
GT025	30	15.85	37.20	0.00	0.00	0.34	46.62	100	0.37	0.63	0.00	0.00	0.00	1.00	micrite
GT025	31	14.06	39.55	0.00	0.00	0.00	46.38	100	0.33	0.67	0.00	0.00	0.00	1.00	micrite
GT025	32	14.95	38.09	0.00	0.46	0.00	46.49	100	0.35	0.64	0.00	0.01	0.00	1.00	micrite

		Weight % oxide (normalised)							Ionic ratio [normalised to 3 [O]						COMMENTS
SAMPLE	No	MgO	CaO	MnO	FeO	SrO	CO_2 (calc)	*Total wt%	Mg^{2+}	Ca^{2+}	Mn^{2+}	Fe^{2+}	Sr^{2+}	CO_3^{2-}	
GT025	33	13.22	40.54	0.00	0.00	0.00	46.24	100	0.31	0.69	0.00	0.00	0.00	1.00	micrite
GT025	34	15.80	37.24	0.00	0.31	0.00	46.65	100	0.37	0.63	0.00	0.00	0.00	1.00	micrite
GT025	35	15.16	38.27	0.00	0.00	0.00	46.57	100	0.36	0.64	0.00	0.00	0.00	1.00	micrite
GT025	36	15.36	38.04	0.00	0.00	0.00	46.61	100	0.36	0.64	0.00	0.00	0.00	1.00	micrite
GT025	37	12.71	40.45	0.35	0.00	0.46	46.03	100	0.30	0.69	0.00	0.00	0.00	1.00	micrite
GT025	38	13.66	40.03	0.00	0.00	0.00	46.31	100	0.32	0.68	0.00	0.00	0.00	1.00	micrite
GT025	39	11.90	42.09	0.00	0.00	0.00	46.01	100	0.28	0.72	0.00	0.00	0.00	1.00	micrite
GT025	40	14.98	38.48	0.00	0.00	0.00	46.54	100	0.35	0.65	0.00	0.00	0.00	1.00	micrite
GT025	41	14.33	39.24	0.00	0.00	0.00	46.43	100	0.34	0.66	0.00	0.00	0.00	1.00	micrite
GT025	42	15.04	38.41	0.00	0.00	0.00	46.55	100	0.35	0.65	0.00	0.00	0.00	1.00	micrite
GT025	43	0.00	55.76	0.00	0.00	0.34	43.90	100	0.00	1.00	0.00	0.00	0.00	1.00	shell
GT025	44	0.00	56.04	0.00	0.00	0.00	43.96	100	0.00	1.00	0.00	0.00	0.00	1.00	shell
GT025	45	0.00	55.78	0.00	0.00	0.32	43.90	100	0.00	1.00	0.00	0.00	0.00	1.00	shell
GT025	46	0.00	55.67	0.00	0.00	0.45	43.87	100	0.00	1.00	0.00	0.00	0.00	1.00	shell
GT025	47	0.20	55.47	0.00	0.00	0.40	43.92	100	0.01	0.99	0.00	0.00	0.00	1.00	shell
GT025	48	0.22	54.04	0.00	0.00	2.17	43.56	100	0.01	0.97	0.00	0.00	0.02	1.00	aragonite dog-tooth rim
GT025	49	0.25	54.01	0.00	0.00	2.17	43.57	100	0.01	0.97	0.00	0.00	0.02	1.00	aragonite dog-tooth rim
GT025	50	3.95	50.09	0.00	0.00	1.64	44.31	100	0.10	0.89	0.00	0.00	0.02	1.00	aragonite dog-tooth rim
GT025	51	1.07	53.11	0.00	0.00	2.09	43.73	100	0.03	0.95	0.00	0.00	0.02	1.00	aragonite dog-tooth rim
GT025	52	0.00	54.47	0.00	0.00	1.96	43.57	100	0.00	0.98	0.00	0.00	0.02	1.00	aragonite dog-tooth rim
GT025	53	0.00	54.37	0.00	0.00	2.09	43.54	100	0.00	0.98	0.00	0.00	0.02	1.00	aragonite dog-tooth rim
GT025	54	0.24	54.12	0.00	0.00	2.06	43.59	100	0.01	0.97	0.00	0.00	0.02	1.00	aragonite dog-tooth rim
GT025	55	0.99	53.38	0.00	0.00	1.87	43.76	100	0.02	0.96	0.00	0.00	0.02	1.00	aragonite dog-tooth rim
GT025	56	0.62	54.01	0.00	0.00	1.62	43.75	100	0.02	0.97	0.00	0.00	0.02	1.00	aragonite dog-tooth rim
GT025	57	3.09	50.85	0.25	0.00	1.66	44.14	100	0.08	0.90	0.00	0.00	0.02	1.00	aragonite dog-tooth rim
GT025	58	1.50	53.13	0.00	0.00	1.43	43.93	100	0.04	0.95	0.00	0.00	0.01	1.00	aragonite dog-tooth rim
GT025	59	0.00	54.92	0.00	0.00	1.40	43.68	100	0.00	0.99	0.00	0.00	0.01	1.00	aragonite dog-tooth rim
GT025	60	0.00	55.01	0.00	0.00	1.28	43.71	100	0.00	0.99	0.00	0.00	0.01	1.00	aragonite dog-tooth rim
GT025	61	1.25	53.42	0.00	0.00	1.44	43.89	100	0.03	0.95	0.00	0.00	0.01	1.00	aragonite dog-tooth rim
GT025	62	0.69	53.89	0.00	0.00	1.66	43.75	100	0.02	0.97	0.00	0.00	0.02	1.00	aragonite dog-tooth rim

**Note: Some analytical totals were low (<90%) because of the microporous nature of the cements. Therefore all data were normalised to 100%*

4.10 SAMPLE GT039

This sample comprises four angular to sub-angular clasts up to 70 mm diameter, of a fine to medium-grained, reasonably well sorted, massive, buff coloured sandstone (Plate 54). Some evidence of bioturbation and boring by micro marine organisms is visible, with burrows and borings that have been infilled by coarser-grained, winnowed detritus (Plate 55). Some orange-brown staining from iron oxyhydroxides is present. Minor bryozoan encrustations are present on the surfaces.

Plate 54. Photograph of sample GT039. The largest clast is <70 mm diameter. These are angular to sub-angular clasts, which show some orange-brown colouration from iron oxyhydroxide staining. Field of view ~200 mm wide.

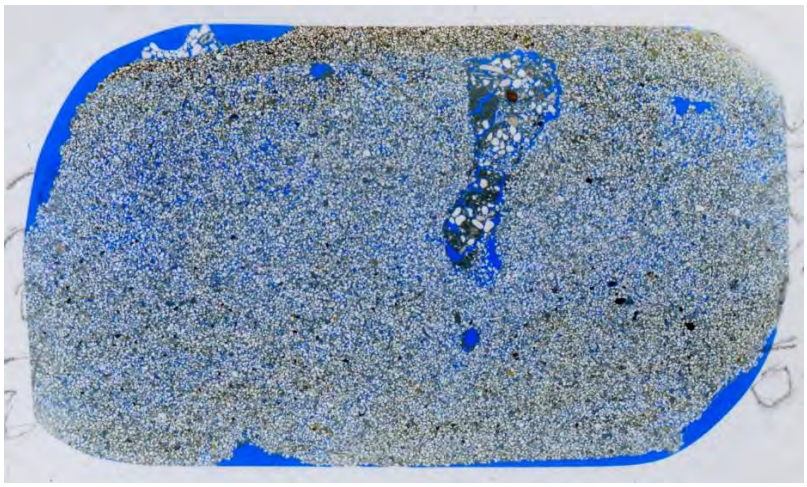

Plate 55. Scanned image of thin section prepared from sample GT039. A cross-section of a large burrow is visible. The sample is well sorted, but shows evidence of orange-brown staining by iron oxyhydroxides, particularly around the edges. Field of view = 48 mm wide.

The polished thin section prepared from one of the clasts of sample GT039 is shown in Plate 55. The sandstone comprises reasonably well sorted, fine to medium-grained sand (<300 µm), with angular to sub-angular grains. The detrital sand grains are dominantly quartz, with numerous bioclastic fragments and some glauconite grains ("glauconie" *sensu lato*). The sample displays patchy distribution of cementation and porosity, with some larger intergranular pores that are oversized relative to the detrital grain size (Plate 56). These oversized pores represent framework grain dissolution sites, but this may also have been enhanced by some dissolution of the original cement (cf. Schmidt and McDonald, 1979). In the cemented areas, the matrix is micritic high-magnesian calcite that has formed as clusters of globular masses or clots. Some staining by very fine iron oxyhydroxide was noted, particularly within the micritic cement and around grain margins close to the outer edges of the sample but no pyrite precursor was observed (Plate 57).

High-resolution BSEM observations show that the micritic high-magnesian calcite cement is extremely microporous, comprising spherical to micro-botryoidal aggregates (Plate 58). Unlike those observed in sample GT004, the aggregates in GT039 are not rimed by coarser subidiomorphic or idiomorphic rhombic calcite crystals. The micrite in this sample has formed thin rims around a very small residual central cavity (<2 µm) creating a "cellular" microfabric. The size of these microscopic cavities is of a similar magnitude to that of bacterial cells (e.g. Konhauser, 2007) an. They may therefore represent bacterial cells that have been preserved within the carbonate cement, and around which the carbonate may have nucleated. This cellular microfabric closely resemble fossilised and mineralised bacterial cells described from experimental studies and other environments in the literature (c.f. Martill and Wilby, 1994; Wilby and Whyte, 1995).

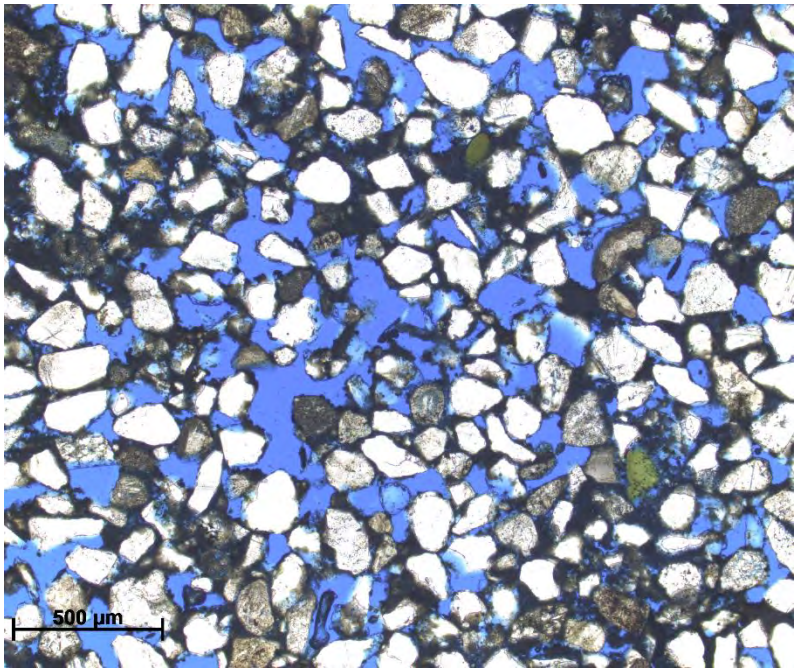

Plate 56. Transmitted light photomicrograph of sample GT039. This image shows the patchy cementation and oversized pore spaces. Some glauconite grains are present in this image.

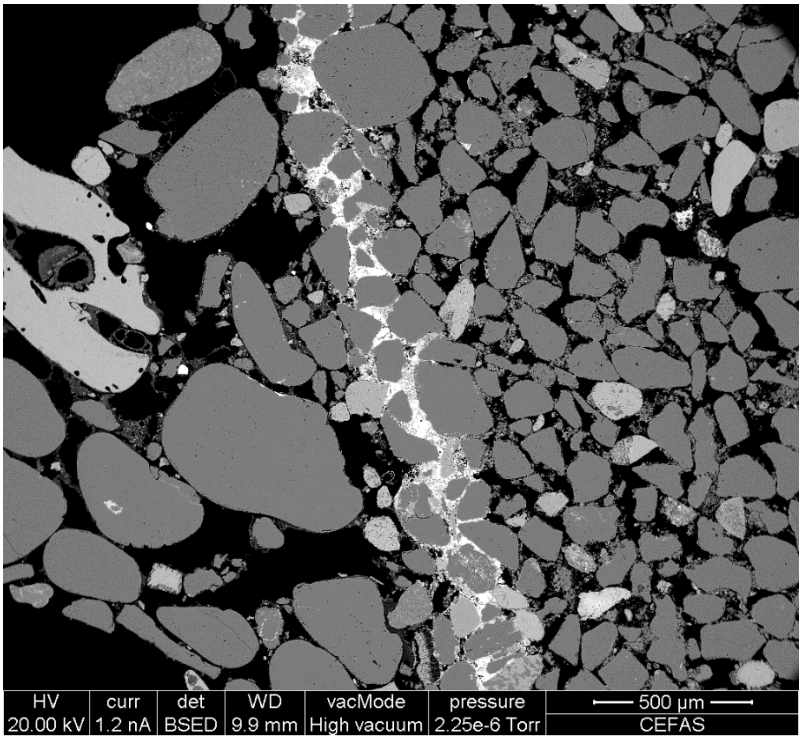

Plate 57. BSEM image showing the iron oxidation around the edge of the sample. The coarser material on the left side of the image is accreted material forming part of a worm cast / burrow. Sample GT039

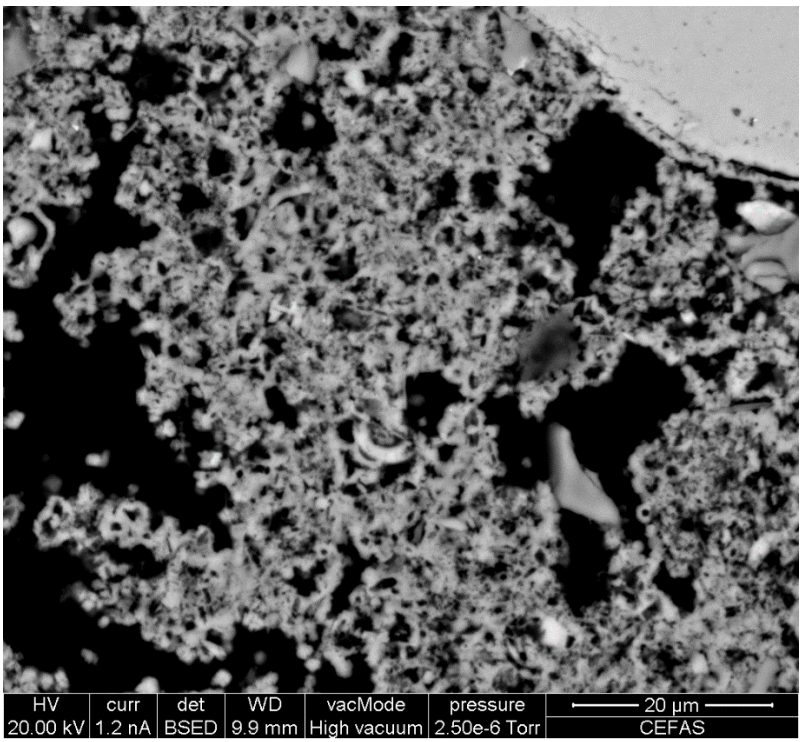

Plate 58. BSEM image showing the microporous, micritic high-magnesian calcite cement. Sample GT039.

ED-EPMA analysis of the carbonate cements are presented in Table 13 and are summarised in Figure 14. The micritic magnesian calcite cements range between 27 and 42 mole % $MgCO_3$ in solid solution (i.e. the structural formula of the calcite can be represented as $Ca_{0.58\text{-}0.73}Mg_{0.42\text{-}0.27}CO_3$). The shell fragments analysed are calcite with no detectable Sr.

The sequence of sedimentary and post-depositional diagenetic events recorded from sample GT039 can be summarised as follows:

1. Deposition of sandy sediment.
2. Syndepositional bioturbation.
3. Microbial precipitation of micritic high-magnesian calcite within the near-surface of the sediment, causing lithification.
4. Minor oxidation within the cement and around some grains, particularly around the outer surfaces of the clasts.
5. Some colonisation of bryozoans on the lithified surface of the clast.

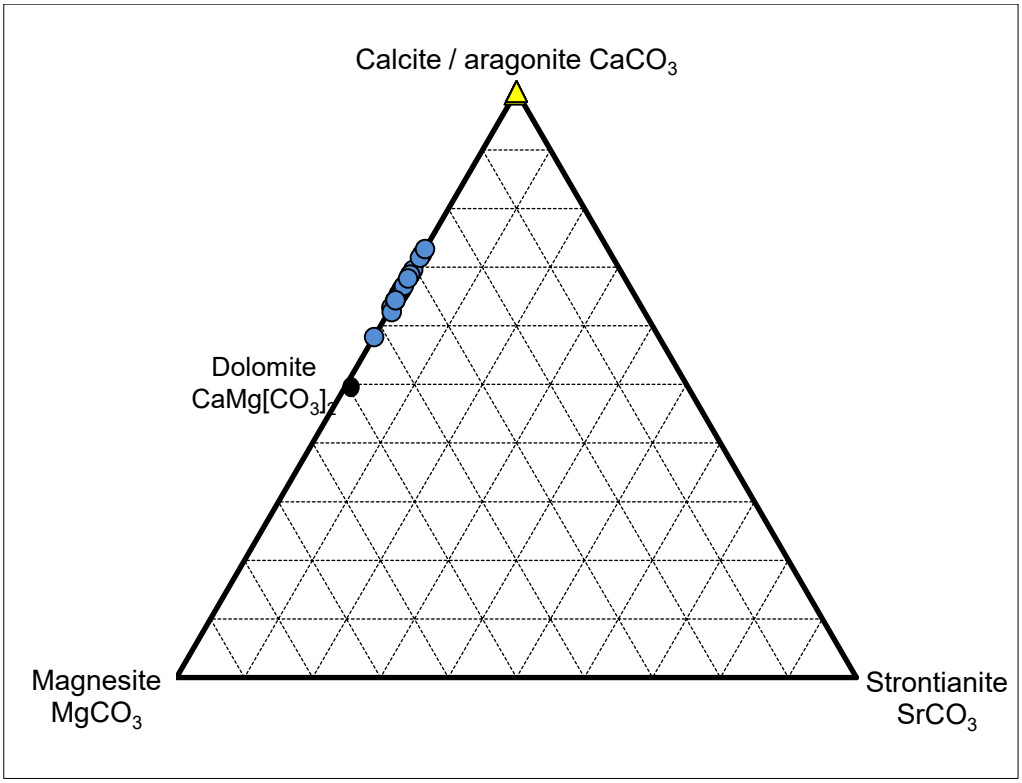

Figure 14. $CaCO_3$-$MgCO_3$-$SrCO_3$ molar ratio plot illustrating the compositions of the high-magnesian calcite micritic cement (solid blue circles) and shell fragments (yellow triangles) from sample GT039.

Table 13. Electron microprobe carbonate cements in sample GT039

		Weight % oxide (normalised)							Ionic ratio [normalised to 3 [O]						COMMENTS
SAMPLE	No	MgO	CaO	MnO	FeO	SrO	CO_2 (calc)	*Total wt%	Mg^{2+}	Ca^{2+}	Mn^{2+}	Fe^{2+}	Sr^{2+}	CO_3^{2-}	
GT039	1	12.80	40.70	0.00	0.37	0.00	46.13	100	0.30	0.69	0.00	0.00	0.00	1.00	microcellular micrite
GT039	2	14.58	38.33	0.00	0.68	0.00	46.41	100	0.34	0.65	0.00	0.01	0.00	1.00	microcellular micrite
GT039	3	14.31	38.71	0.00	0.60	0.00	46.37	100	0.34	0.66	0.00	0.01	0.00	1.00	microcellular micrite
GT039	4	15.05	37.66	0.00	0.81	0.00	46.48	100	0.35	0.64	0.00	0.01	0.00	1.00	microcellular micrite
GT039	5	15.52	37.09	0.00	0.83	0.00	46.56	100	0.36	0.63	0.00	0.01	0.00	1.00	microcellular micrite
GT039	6	17.90	34.51	0.00	0.61	0.00	46.98	100	0.42	0.58	0.00	0.01	0.00	1.00	microcellular micrite
GT039	7	14.12	38.84	0.00	0.71	0.00	46.33	100	0.33	0.66	0.00	0.01	0.00	1.00	microcellular micrite
GT039	8	12.99	39.63	0.00	1.31	0.00	46.07	100	0.31	0.67	0.00	0.02	0.00	1.00	microcellular micrite
GT039	9	15.12	37.91	0.00	0.45	0.00	46.52	100	0.35	0.64	0.00	0.01	0.00	1.00	microcellular micrite
GT039	10	15.58	36.34	0.00	1.15	0.49	46.44	100	0.37	0.61	0.00	0.02	0.00	1.00	microcellular micrite
GT039	11	14.02	39.35	0.00	0.27	0.00	46.35	100	0.33	0.67	0.00	0.00	0.00	1.00	microcellular micrite
GT039	12	15.20	38.22	0.00	0.00	0.00	46.58	100	0.36	0.64	0.00	0.00	0.00	1.00	microcellular micrite
GT039	18	11.64	42.14	0.00	0.28	0.00	45.94	100	0.28	0.72	0.00	0.00	0.00	1.00	microcellular micrite
GT039	19	11.23	39.45	1.06	2.73	0.00	45.54	100	0.27	0.68	0.01	0.04	0.00	1.00	microcellular micrite
GT039	20	13.19	40.33	0.00	0.28	0.00	46.21	100	0.31	0.68	0.00	0.00	0.00	1.00	microcellular micrite
GT039	21	13.43	39.90	0.00	0.44	0.00	46.23	100	0.32	0.68	0.00	0.01	0.00	1.00	microcellular micrite
GT039	22	11.30	42.79	0.00	0.00	0.00	45.91	100	0.27	0.73	0.00	0.00	0.00	1.00	microcellular micrite
GT039	13	0.00	56.04	0.00	0.00	0.00	43.96	100	0.00	1.00	0.00	0.00	0.00	1.00	shell
GT039	14	0.18	55.62	0.00	0.23	0.00	43.97	100	0.00	0.99	0.00	0.00	0.00	1.00	shell
GT039	15	0.00	55.84	0.21	0.00	0.00	43.95	100	0.00	1.00	0.00	0.00	0.00	1.00	shell
GT039	16	0.00	55.73	0.00	0.33	0.00	43.93	100	0.00	1.00	0.00	0.00	0.00	1.00	shell
GT039	17	0.00	56.04	0.00	0.00	0.00	43.96	100	0.00	1.00	0.00	0.00	0.00	1.00	shell

**Note: Some analytical totals were low (<90%) because of the microporous nature of the cements. Therefore all data were normalised to 100%*

4.11 SAMPLE GT050

This sample comprises a single clast, approximately 70 mm in diameter, which has been heavily bioturbated (Plate 59). The sample comprises buff-coloured sandstone and light-grey siltstone layers. Numerous burrows, and borings by marine organisms are present and the surface has evidence of some calcareous serpulid worm encrustations.

Plate 59. Photograph of sample GT050 showing a highly bioturbated surface. Field of view ~150 mm wide.

A scanned image of the polished thin section prepared from sample GT050 is shown in Plate 60. It consists of interlaminated fine sandstone and siltstone, with discontinuous laminae. The fabric is highly heterogeneous and the broadly sub-horizontal layering between the sandstone and siltstone laminae has been disrupted by extensive bioturbation. Some of the burrows themselves are infilled by winnowed sand that forms lenses of material that cross-cut the finer-grained siltstone layers. The siltstone component contains numerous clusters of authigenic framboidal pyrite. The sandstone component is poorly sorted, and comprises angular to sub-angular, fine to medium (<400 µm) sand, dominated by quartz, with subordinate feldspars, lithics and carbonate grains. The fabric is uncompacted, but heterogeneous, with some areas being matrix-supported, and other areas being grain-supported. Some secondary porosity is present. The sediment matrix comprises a brown-coloured micrite cement.

High-resolution BSEM observations show the micritic carbonate cement to be intimately mixed with clay and silica rich sediment. As observed in other samples such as: GT007 and GT112, the cement is a high-magnesian calcite cement, which is microporous, comprising spherical to micro-boytryoidal aggregates. However, as in sample GT039, the coarsening-up of the micrite observed in some of the other samples was not observed here. Rare acicular needles of aragonite are observed growing on top of some of the micritic clots. Quantitative ED-EPMA analysis could not be obtained from these needles due to their very fine size, and the presence of silicate material in intimate association compromised the analyses.

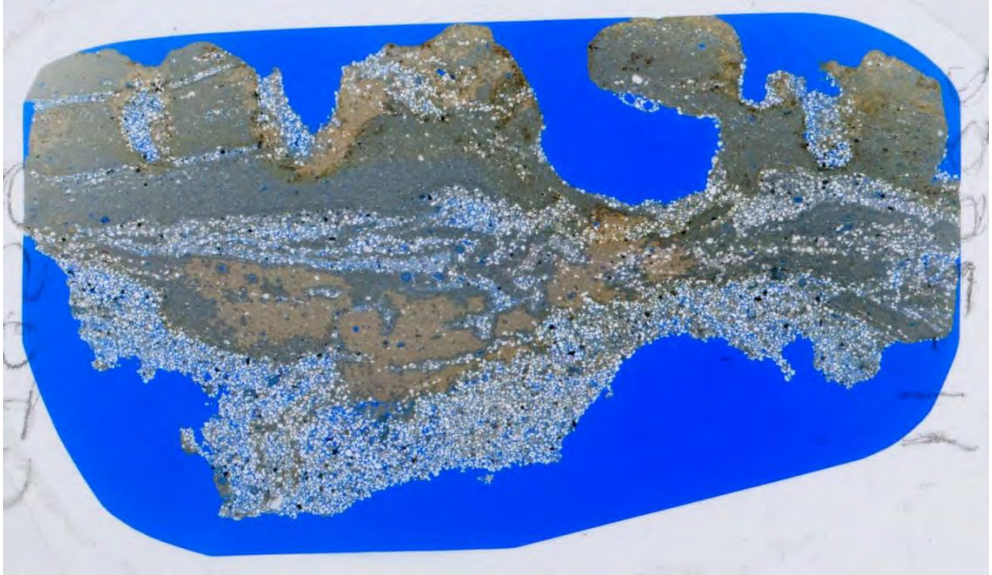

Plate 60. Scan of the thin section prepared from sample GT050. Field of view = 48 mm wide.

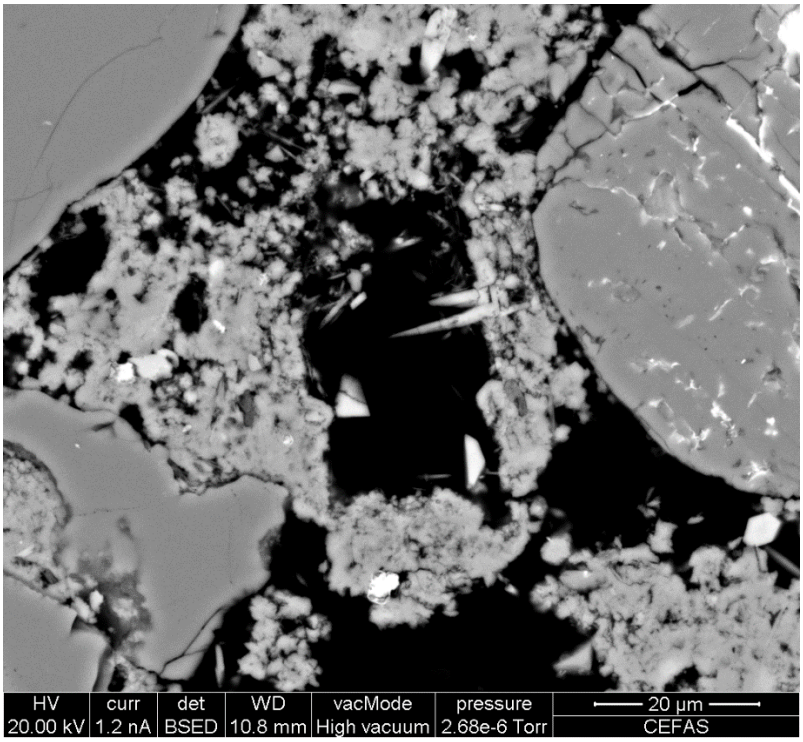

Plate 61. BSEM image showing the globular aggregates of, microporous, high-magnesian calcite micrite and the rare acicular aragonite (see centre of image). GT050

ED-EPMA analysis of the carbonate cements are presented in Table 14 and are summarised in Figure 15. The micritic magnesian calcite cements display a wide range of compositions between 2 and 34 mole % $MgCO_3$ in solid solution (i.e. the structural formula of the calcite can be represented as $Ca_{0.66\text{-}0.98}Mg_{0.34\text{-}0.02}CO_3$). As such, these cements range from moderately low magnesian calcite to at the higher-magnesian calcite at the extreme end of the calcite ($CaCO_3$)-magnesite ($MgCO_3$) solid-solution series (cf. Deer et al., 1962a, b: Mackenzie et al., 1983). The shell fragments analysed are composed of calcite with no detectable Sr, but the dog-tooth rims of aragonite nucleated on the surface of some shells contained 2 mole % Sr.

The sequence of sedimentary and post-depositional diagenetic events recorded from sample GT050 can be summarised as follows:

1. Deposition of fine silt and fine to medium-grained sandy sediment.
2. Extensive syndepositional bioturbation
3. Precipitation of micritic high-magnesian calcite causing lithification.
4. Limited formation of a later stage aragonite cement.
5. Boring by marine organisms and colonisation by serpulid worms on the upper lithified surface of the clast.

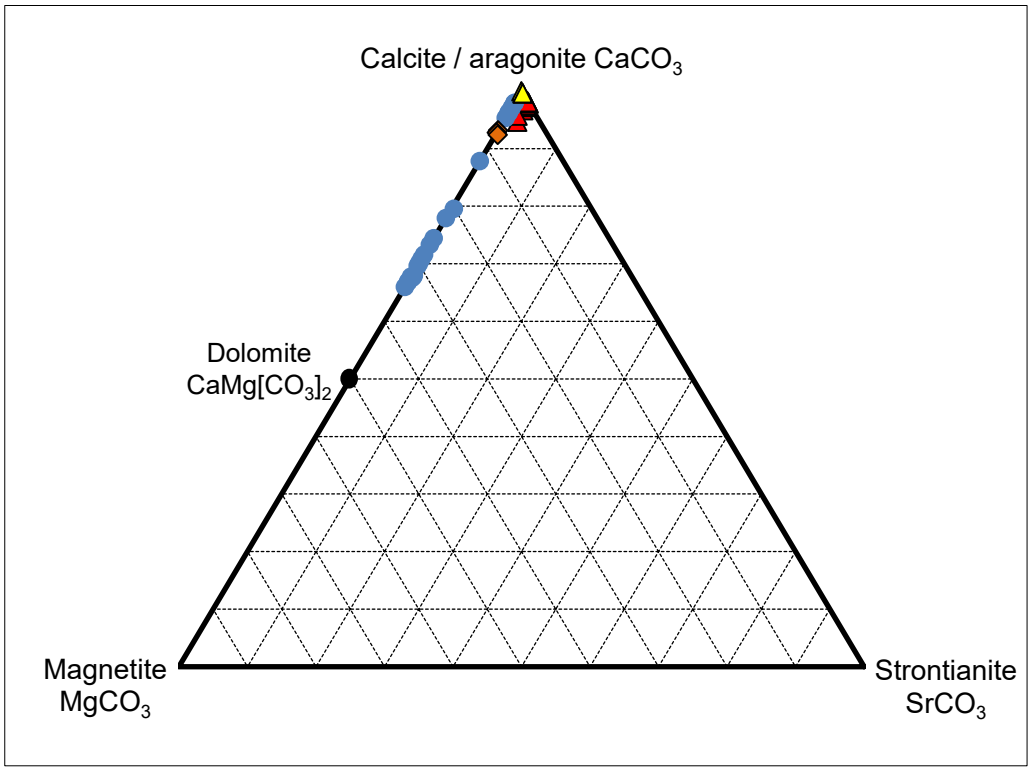

Figure 15. $CaCO_3$-$MgCO_3$-$SrCO_3$ molar ratio plot illustrating the compositions of the high-magnesian calcite micritic cement (solid blue circles) and shell fragments (yellow triangles), calcite grain (orange diamonds) and aragonite dog-tooth rim around a shell fragment from sample GT050.

Table 14. Electron microprobe analyses of carbonate cements and shell fragments in sample GT050

		Weight % oxide (normalised)							Ionic ratio [normalised to 3 [O]						COMMENTS
SAMPLE	No	MgO	CaO	MnO	FeO	SrO	CO_2 (calc)	*Total wt%	Mg^{2+}	Ca^{2+}	Mn^{2+}	Fe^{2+}	Sr^{2+}	CO_3^{2-}	
GT050	1	11.21	42.89	0.00	0.00	0.00	45.89	100	0.27	0.73	0.00	0.00	0.00	1.00	micrite rim
GT050	2	13.42	40.00	0.00	0.00	0.39	46.20	100	0.32	0.68	0.00	0.00	0.00	1.00	micrite rim
GT050	3	12.81	41.02	0.00	0.00	0.00	46.17	100	0.30	0.70	0.00	0.00	0.00	1.00	micrite rim
GT050	4	1.14	54.50	0.00	0.22	0.00	44.14	100	0.03	0.97	0.00	0.00	0.00	1.00	micrite
GT050	5	1.43	54.17	0.20	0.00	0.00	44.19	100	0.04	0.96	0.00	0.00	0.00	1.00	micrite
GT050	6	0.83	55.07	0.00	0.00	0.00	44.11	100	0.02	0.98	0.00	0.00	0.00	1.00	micrite
GT050	7	1.56	54.20	0.00	0.00	0.00	44.23	100	0.04	0.96	0.00	0.00	0.00	1.00	micrite
GT050	8	0.81	55.09	0.00	0.00	0.00	44.10	100	0.02	0.98	0.00	0.00	0.00	1.00	micrite
GT050	9	4.95	49.91	0.00	0.36	0.00	44.78	100	0.12	0.87	0.00	0.00	0.00	1.00	micrite
GT050	10	1.86	53.59	0.00	0.29	0.00	44.26	100	0.05	0.95	0.00	0.00	0.00	1.00	micrite
GT050	11	10.66	43.20	0.00	0.38	0.00	45.76	100	0.25	0.74	0.00	0.01	0.00	1.00	micrite
GT050	12	13.57	39.83	0.00	0.00	0.37	46.23	100	0.32	0.68	0.00	0.00	0.00	1.00	micrite
GT050	13	13.66	40.02	0.00	0.00	0.00	46.31	100	0.32	0.68	0.00	0.00	0.00	1.00	micrite
GT050	14	9.15	45.10	0.00	0.24	0.00	45.52	100	0.22	0.78	0.00	0.00	0.00	1.00	micrite
GT050	15	14.38	38.85	0.00	0.37	0.00	46.40	100	0.34	0.66	0.00	0.00	0.00	1.00	micrite
GT050	16	8.28	45.69	0.00	0.35	0.40	45.27	100	0.20	0.79	0.00	0.00	0.00	1.00	micrite
GT050	17	12.20	41.32	0.00	0.47	0.00	46.02	100	0.29	0.70	0.00	0.01	0.00	1.00	micrite
GT050	18	11.96	42.02	0.00	0.00	0.00	46.02	100	0.28	0.72	0.00	0.00	0.00	1.00	micrite
GT050	19	14.11	39.50	0.00	0.00	0.00	46.39	100	0.33	0.67	0.00	0.00	0.00	1.00	micrite
GT050	20	13.90	39.32	0.00	0.47	0.00	46.31	100	0.33	0.67	0.00	0.01	0.00	1.00	micrite
GT050	21	12.54	41.09	0.00	0.28	0.00	46.09	100	0.30	0.70	0.00	0.00	0.00	1.00	micrite
GT050	22	0.55	53.81	0.00	0.00	1.98	43.66	100	0.01	0.97	0.00	0.00	0.02	1.00	dog tooth rim around shell
GT050	23	0.30	54.08	0.00	0.00	2.01	43.61	100	0.01	0.97	0.00	0.00	0.02	1.00	dog tooth rim around shell
GT050	24	0.00	54.54	0.00	0.00	1.87	43.59	100	0.00	0.98	0.00	0.00	0.02	1.00	dog tooth rim around shell
GT050	25	0.00	54.67	0.00	0.00	1.71	43.62	100	0.00	0.98	0.00	0.00	0.02	1.00	dog tooth rim around shell
GT050	26	0.00	54.46	0.00	0.00	1.98	43.57	100	0.00	0.98	0.00	0.00	0.02	1.00	dog tooth rim around shell
GT050	27	0.19	54.14	0.00	0.00	2.09	43.58	100	0.00	0.97	0.00	0.00	0.02	1.00	dog tooth rim around shell
GT050	28	1.29	52.83	0.00	0.00	2.12	43.76	100	0.03	0.95	0.00	0.00	0.02	1.00	dog tooth rim around shell
GT050	29	0.00	54.30	0.00	0.00	2.17	43.53	100	0.00	0.98	0.00	0.00	0.02	1.00	dog tooth rim around shell
GT050	30	1.07	53.48	0.00	0.00	1.63	43.82	100	0.03	0.96	0.00	0.00	0.02	1.00	dog tooth rim around shell
GT050	31	0.00	54.50	0.00	0.00	1.93	43.58	100	0.00	0.98	0.00	0.00	0.02	1.00	dog tooth rim around shell
GT050	32	0.00	55.73	0.00	0.00	0.38	43.89	100	0.00	1.00	0.00	0.00	0.00	1.00	shell

		Weight % oxide (normalised)							Ionic ratio [normalised to 3 [O]						COMMENTS
SAMPLE	No	MgO	CaO	MnO	FeO	SrO	CO_2 (calc)	*Total wt%	Mg^{2+}	Ca^{2+}	Mn^{2+}	Fe^{2+}	Sr^{2+}	CO_3^{2-}	
GT050	33	0.00	56.04	0.00	0.00	0.00	43.96	100	0.00	1.00	0.00	0.00	0.00	1.00	shell
GT050	34	0.00	55.74	0.00	0.00	0.37	43.89	100	0.00	1.00	0.00	0.00	0.00	1.00	shell
GT050	35	2.76	52.80	0.00	0.00	0.00	44.44	100	0.07	0.93	0.00	0.00	0.00	1.00	calcite grain
GT050	36	2.93	52.60	0.00	0.00	0.00	44.47	100	0.07	0.93	0.00	0.00	0.00	1.00	calcite grain
GT050	37	2.93	52.32	0.00	0.00	0.36	44.40	100	0.07	0.92	0.00	0.00	0.00	1.00	calcite grain

Note: Some analytical totals were low (<90%) because of the microporous nature of the cements. Therefore all data were normalised to 100%

4.12 SAMPLE GT055

This sample comprises two irregular shaped, broadly tabular, sandstone clasts (<60 mm diameter) (Plate 62). The grey-buff coloured sandstone has been heavily bioturbated and shows orange-brown, iron oxyhydroxides staining. Several bryozoan encrustations are visible on the surfaces.

Plate 62. Photograph of sample GT055 which comprises two irregular shaped clasts. Field of view ~145 mm wide.

The polished thin section prepared through a fragment of GT055 is shown in Plate 63. The sample has a marked orange-brown colouration where the sample is well cemented, and the cement and detrital grain surfaces have been stained by iron oxyhydroxides, particularly around the edges of the sample. The centre of the sample has higher porosity shown by the blue-dyed resin impregnation of the thin section (Plate 63). Within this central area some intergranular pores are oversized, possibly as a result of the dissolution unstable detrital components (cf. criteria for the recognition secondary porosity defined by Schmidt and McDonald, 1979), or alternatively, this may be part of a burrow that was subsequently infilled with winnowed sand grains. The more porous sandstone is grain supported with simple-point grain contacts. The well cemented areas are matrix supported (Plate 64). Detrital grains are dominated by angular to sub-angular quartz (<400 µm), with subordinate rounded calcite grains and rare, glauconite grains ("glauconie" *sensu lato*). The matrix of the sandstone is a muddy micrite cement, which is microporous and forms globular aggregates or clots of microcrystalline magnesian calcite (Plate 65 and Plate 66). Some of the micrite cement preserves a cellular microfabric, described previously in some of the other samples (refer to sample GT004 for more detail). The cement comprises blocky rhombs of calcite (Plate 66) enclosing spherical voids (<2 µm), which may represent included and preserved bacterial cells.

Plate 63. Scanned of the thin section prepared from sample GT055. The iron oxyhydroxide staining is clearly visible. More porous areas of sandstone are revealed by the blue-dyed resin impregnation. Field of view = 48 mm wide.

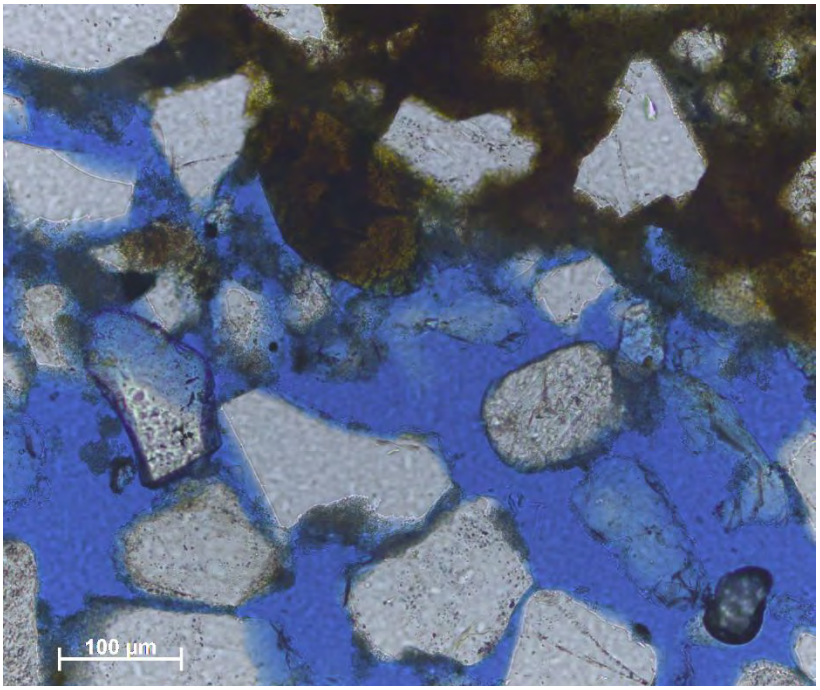

Plate 64. Transmitted light photomicrograph (plain polarised light) showing the contrast between the well cemented outer part of the sample, and the more porous central area. The central area is grain supported but with oversized pores. The well cemented area is matrix supported. Sample GT055

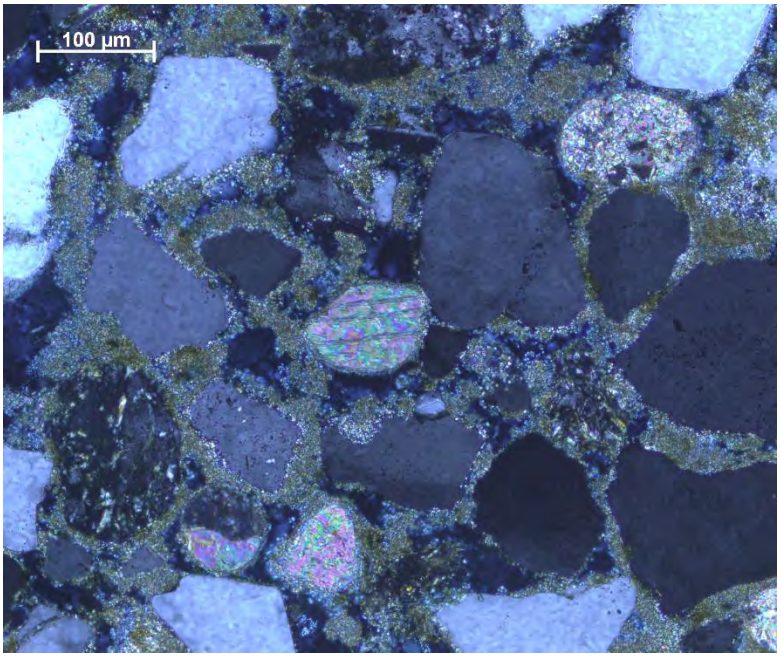

Plate 65. Transmitted light photomicrograph (cross-polarised light) showing the micritic cement. Note the number of rounded calcite grains. Sample GT055

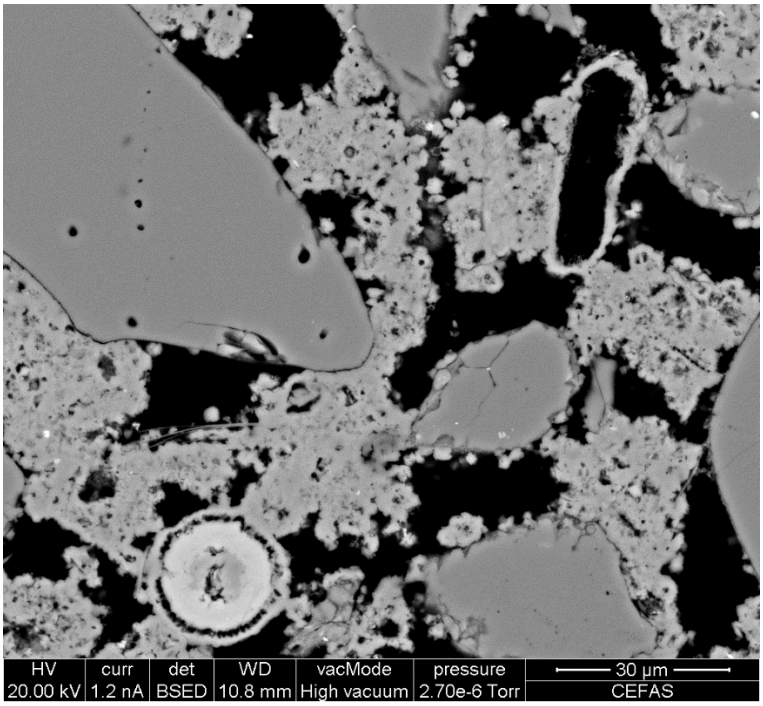

Plate 66. BSEM image showing the microporous, micritic cement. The small voids (<2 µm) may represent bacterial cells around which the carbonate nucleated. Sample GT055

ED-EPMA analysis of the carbonate cements are presented in Table 15 and are summarised in Figure 16. The micritic magnesian calcite cements range in composition between 28 and 40 mole % $MgCO_3$ in solid solution (i.e. the structural formula of the calcite can be represented as $Ca_{0.60-0.72}Mg_{0.40-0.28}CO_3$). One of the analysed detrital calcite grains also contained up to 26 mole % $MgCO_3$, suggesting this may be a detrital clast derived from reworking of older or penecontemporaneous MDAC.

Neither the shell fragments, nor the calcite grains contain any trace levels of Sr.

The sequence of sedimentary and post-depositional diagenetic events recorded from sample GT055 can be summarised as follows:

1. Deposition of medium grained, sandy sediment.
2. Syndepositional bioturbation
3. Precipitation of micritic high-magnesian calcite, causing lithification.
4. Colonisation of bryozoans on the lithified surface of the clast.

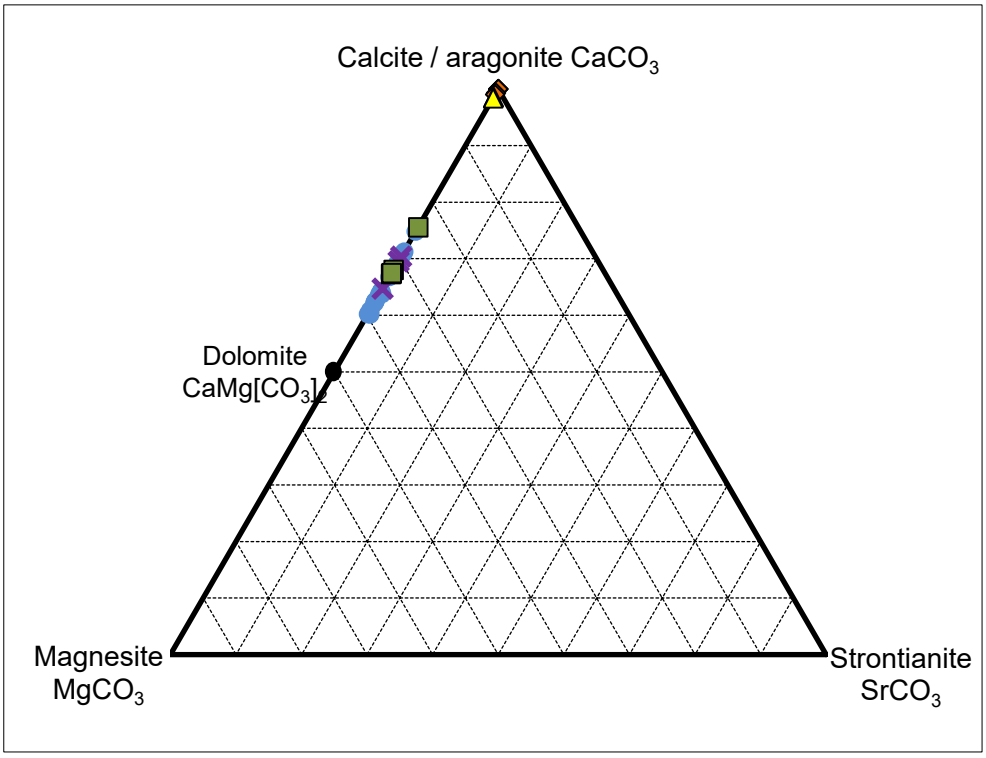

Figure 16. $CaCO_3$-$MgCO_3$-$SrCO_3$ molar ratio plot illustrating the compositions of the carbonate grains (orange diamonds), foraminifera and shell fragments (yellow triangles), high-magnesian calcite micritic cement (solid blue circles), micrite from around some shell fragments (purple crosses), and a relict magnesian-calcite grain (green squares) from sample GT055.

Table 15. Electron microprobe analyses of carbonate cements, grains and bioclastic fragments from GT055

		Weight % oxide (normalised)							Ionic ratio [normalised to 3 [O]						COMMENTS
SAMPLE	No	MgO	CaO	MnO	FeO	SrO	CO_2 (calc)	*Total wt%	Mg^{2+}	Ca^{2+}	Mn^{2+}	Fe^{2+}	Sr^{2+}	CO_3^{2-}	
GT055	1	0.00	56.04	0.00	0.00	0.00	43.96	100	0.00	1.00	0.00	0.00	0.00	1.00	carbonate grain
GT055	2	0.00	55.82	0.00	0.24	0.00	43.94	100	0.00	1.00	0.00	0.00	0.00	1.00	carbonate grain
GT055	3	0.00	56.04	0.00	0.00	0.00	43.96	100	0.00	1.00	0.00	0.00	0.00	1.00	carbonate grain
GT055	4	0.27	55.72	0.00	0.00	0.00	44.01	100	0.01	0.99	0.00	0.00	0.00	1.00	carbonate grain
GT055	5	0.39	55.19	0.00	0.44	0.00	43.99	100	0.01	0.98	0.00	0.01	0.00	1.00	carbonate grain
GT055	6	10.54	30.36	0.41	14.34	0.00	44.36	100	0.26	0.54	0.01	0.20	0.00	1.00	carbonate grain 2
GT055	7	8.43	36.29	0.32	10.61	0.00	44.36	100	0.21	0.64	0.00	0.15	0.00	1.00	carbonate grain 3
GT055	8	10.61	30.34	0.47	14.20	0.00	44.38	100	0.26	0.54	0.01	0.20	0.00	1.00	carbonate grain 4
GT055	9	10.25	30.35	0.48	14.65	0.00	44.27	100	0.25	0.54	0.01	0.20	0.00	1.00	carbonate grain 5
GT055	10	10.39	29.99	0.39	14.96	0.00	44.27	100	0.26	0.53	0.01	0.21	0.00	1.00	carbonate grain 6
GT055	11	12.44	41.14	0.00	0.35	0.00	46.07	100	0.29	0.70	0.00	0.00	0.00	1.00	dark micrite core of shell
GT055	12	12.81	40.68	0.00	0.38	0.00	46.13	100	0.30	0.69	0.00	0.01	0.00	1.00	dark micrite core of shell
GT055	13	13.87	35.36	0.00	4.89	0.00	45.88	100	0.33	0.60	0.00	0.07	0.00	1.00	dark micrite core of shell
GT055	14	0.58	55.36	0.00	0.00	0.00	44.06	100	0.01	0.99	0.00	0.00	0.00	1.00	Foraminifera tests / shell
GT055	15	0.62	55.09	0.00	0.25	0.00	44.05	100	0.02	0.98	0.00	0.00	0.00	1.00	foraminifera tests / shell
GT055	16	0.66	55.27	0.00	0.00	0.00	44.08	100	0.02	0.98	0.00	0.00	0.00	1.00	foraminifera tests / shell
GT055	17	12.07	41.23	0.00	0.73	0.00	45.97	100	0.29	0.70	0.00	0.01	0.00	1.00	micrite
GT055	18	10.24	42.31	0.51	1.39	0.00	45.54	100	0.25	0.73	0.01	0.02	0.00	1.00	micrite
GT055	19	16.77	35.61	0.00	0.51	0.39	46.72	100	0.39	0.60	0.00	0.01	0.00	1.00	micrite
GT055	20	15.18	37.59	0.00	0.38	0.38	46.46	100	0.36	0.63	0.00	0.01	0.00	1.00	micrite
GT055	21	15.97	36.89	0.00	0.48	0.00	46.66	100	0.37	0.62	0.00	0.01	0.00	1.00	micrite
GT055	22	16.06	36.72	0.00	0.55	0.00	46.67	100	0.38	0.62	0.00	0.01	0.00	1.00	micrite
GT055	23	15.16	37.87	0.00	0.44	0.00	46.53	100	0.36	0.64	0.00	0.01	0.00	1.00	micrite
GT055	24	13.00	40.54	0.00	0.28	0.00	46.17	100	0.31	0.69	0.00	0.00	0.00	1.00	micrite
GT055	25	15.93	37.09	0.00	0.29	0.00	46.68	100	0.37	0.62	0.00	0.00	0.00	1.00	micrite
GT055	26	17.01	35.81	0.00	0.32	0.00	46.86	100	0.40	0.60	0.00	0.00	0.00	1.00	micrite
GT055	27	12.83	38.52	0.00	2.75	0.00	45.91	100	0.30	0.66	0.00	0.04	0.00	1.00	micrite rim
GT055	28	14.87	36.25	0.00	2.61	0.00	46.27	100	0.35	0.61	0.00	0.03	0.00	1.00	micrite rim
GT055	29	15.08	37.71	0.00	0.72	0.00	46.49	100	0.35	0.64	0.00	0.01	0.00	1.00	micrite rim
GT055	30	12.16	40.79	0.00	1.10	0.00	45.95	100	0.29	0.70	0.00	0.01	0.00	1.00	micrite rim
GT055	31	13.09	37.09	0.00	3.99	0.00	45.83	100	0.31	0.63	0.00	0.05	0.00	1.00	micrite rim
GT055	32	11.90	41.03	0.00	1.17	0.00	45.90	100	0.28	0.70	0.00	0.02	0.00	1.00	micrite rim

		Weight % oxide (normalised)							Ionic ratio [normalised to 3 [O]						COMMENTS
SAMPLE	No	MgO	CaO	MnO	FeO	SrO	CO_2 (calc)	*Total wt%	Mg^{2+}	Ca^{2+}	Mn^{2+}	Fe^{2+}	Sr^{2+}	CO_3^{2-}	
GT055	33	13.76	38.49	0.00	1.57	0.00	46.18	100	0.33	0.65	0.00	0.02	0.00	1.00	micrite rim
GT055	34	16.43	35.59	0.00	1.32	0.00	46.66	100	0.38	0.60	0.00	0.02	0.00	1.00	micrite rim

**Note: Some analytical totals were low (<90%) because of the microporous nature of the cements. Therefore all data were normalised to 100%*

4.13 SAMPLE GT066

Two sub-rounded, knobbly clasts (100 mm) of grey, poorly sorted, matrix-rich shelly sandstone comprise sample GT066 (Plate 67). Numerous fragments of bioclastic debris have been incorporated within the sample, together with fine siltstone, and fine to coarse grained sandstone.

Plate 67. Photograph of sample GT066. Field of view ~190 mm wide.

The polished thin section prepared from the larger of the two sandstone clasts in sample GT066, is shown in Plate 68. The sand grains are subrounded to rounded, up to 1000 µm in diameter, and dominated by quartz. Part of a coarse igneous lithic (<6 mm) clast containing feldspars and hornblende, which has been incorporated into the sample, is visible in Plate 68,. The sample contains abundant coarse shell fragments dominated by bivalve shells. Microporous, micritic clay forms the matrix of the rock. It has a globular appearance, and lines many of the intergranular pore spaces (Plate 70). It is also present as well-rounded, medium-grained (<300 µm), fine-grained, micritic clay pelloids, which probably originated as faecal pellets. The pelloids often contain abundant framboidal pyrite.

Fibrous aragonite cement has nucleated on and around the grains (Plate 70 and Plate 71), on top of the micritic cement and on top of, and partially replacing, micritic faecal pellets (Plate 71 and Plate 72). The aragonite cement is characterised by the growth of acicular (needle-like) prismatic crystals up to 500 µm long (Plate 73). Often the aragonite forms 'sheaf-like crystal aggregates with radiating 'sprays' of needles: there are thick coatings within some large cavities within the sample (Plate 71). Some of these aragonite sprays have bands of more porous material imparting a banded or colloform texture to them. This texture probably results from repeated periods of growth followed by hiatus. An isopachous fringe of acicular aragonite is often present around the margins of calcareous bioclasts, growing into the adjacent open pore space. Some of these bioclasts may

themselves be aragonitic and may therefore have acted as sites for preferential nucleation of aragonite cement.

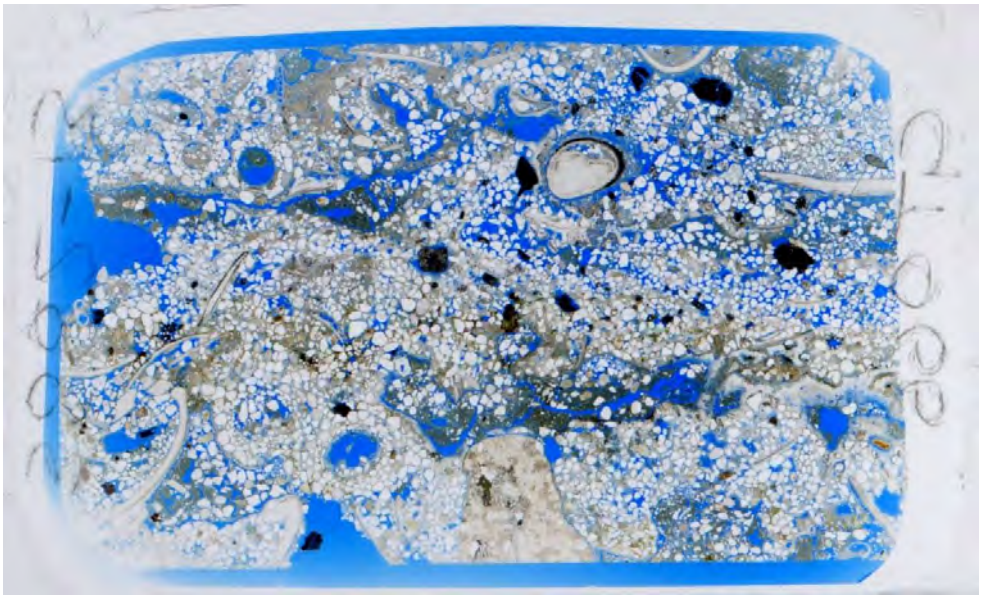

Plate 68. Scanned image of the polished thin section prepared from sample GT066 showing the bioclastic debris incorporated into the sample, as well as the agglutinating foraminifera tests (e.g. lower left quadrant). At the bottom centre of the image, part of a coarse igneous lithic is visible which contains feldspars and hornblende. Field of view = 48 mm wide.

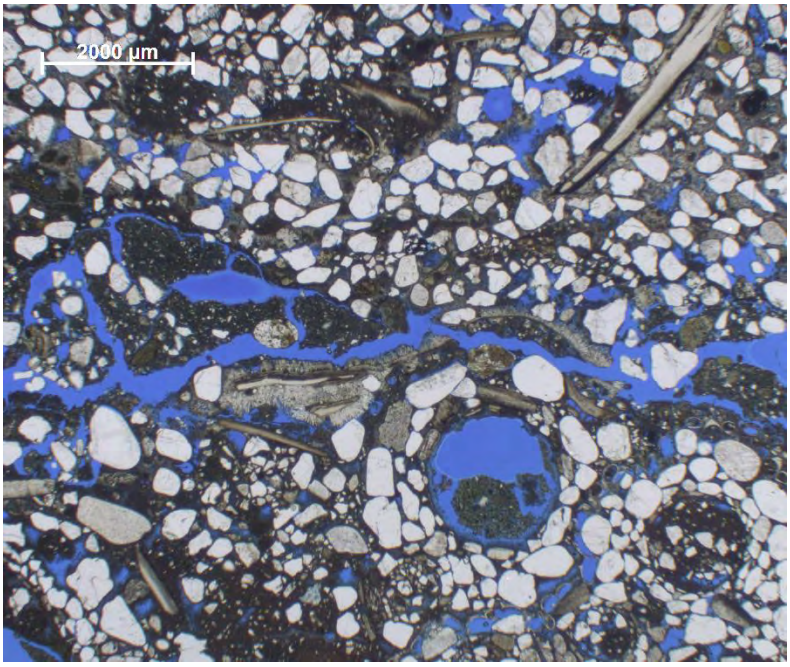

Plate 69. Transmitted light photomicrograph (plain polarised light) showing the poorly sorted packstone texture. The silty sediment, and fine-coarse grained sand are clearly visible. Bioclastic fragments have been incorporated into the sample, as well as agglutinating foraminifera (bottom right quadrant). Sample GT066

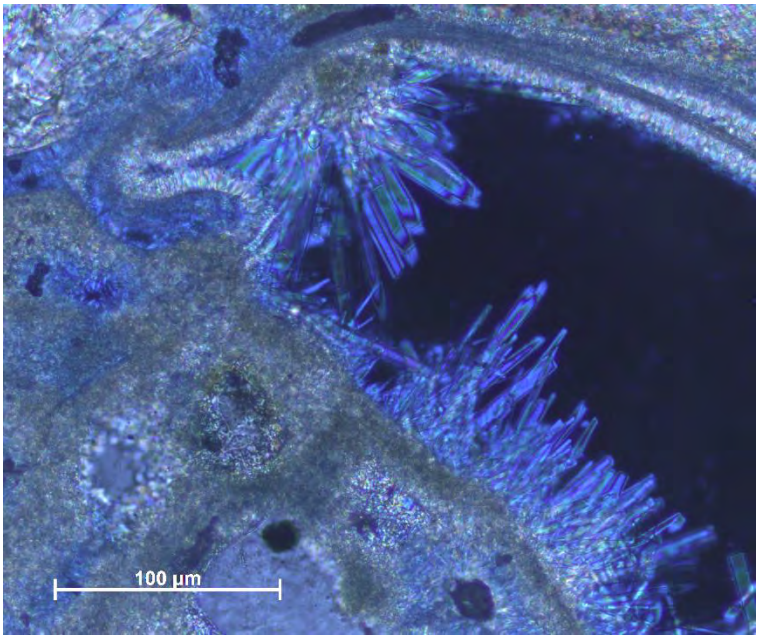

Plate 70. Transmitted light photomicrograph (cross polarised light) showing acicular aragonite growing into intergranular pore space. This has nucleated on earlier micritic cement. Sample GT066

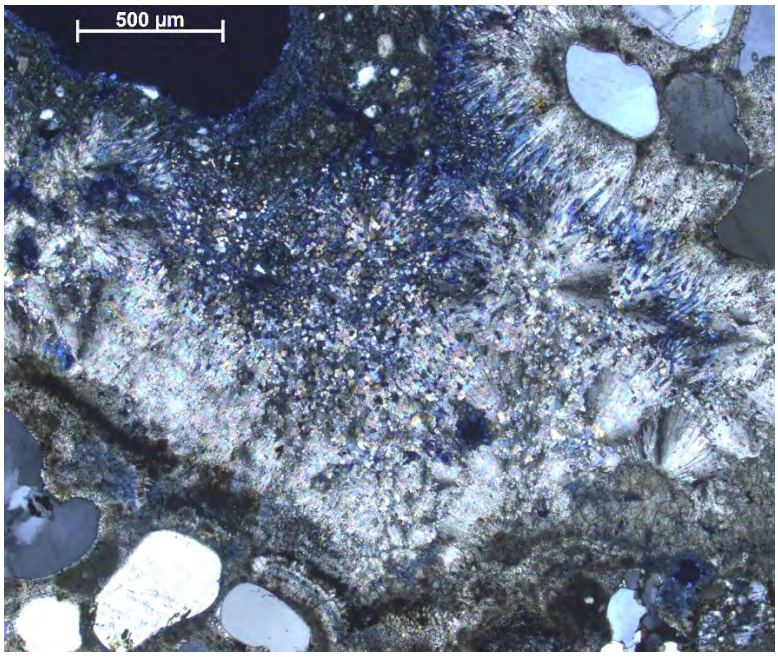

Plate 71. Transmitted light photomicrograph (cross polarised light) showing a thick fringe of acicular aragonite. These thick fringes are infilling large cavities and voids within the sample. Sample GT066

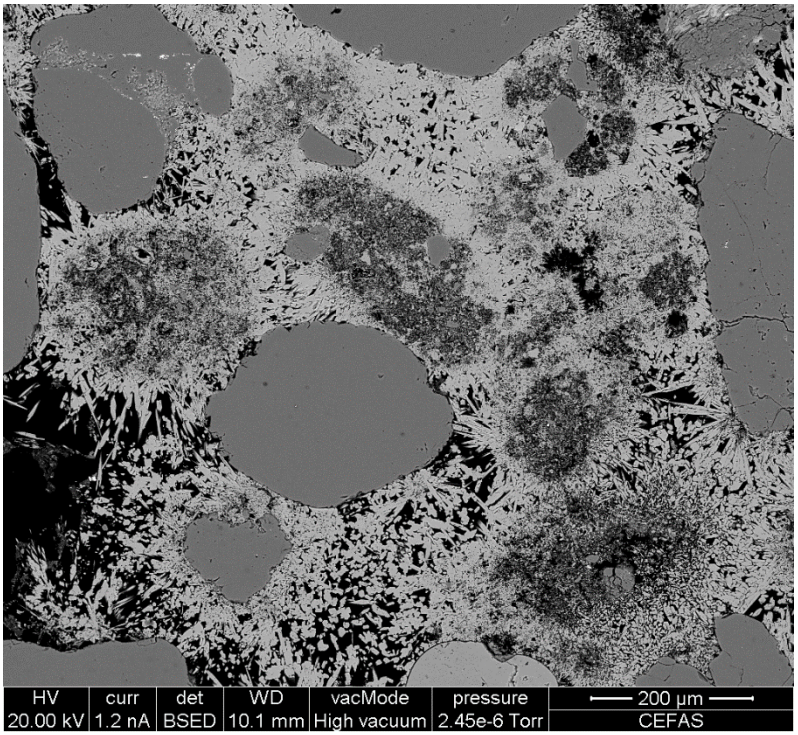

Plate 72. BSEM image of the cements showing the pelleted micrite pelleted fabric which are probably detrital faecal pellets, coated in acicular aragonite. Sample GT066

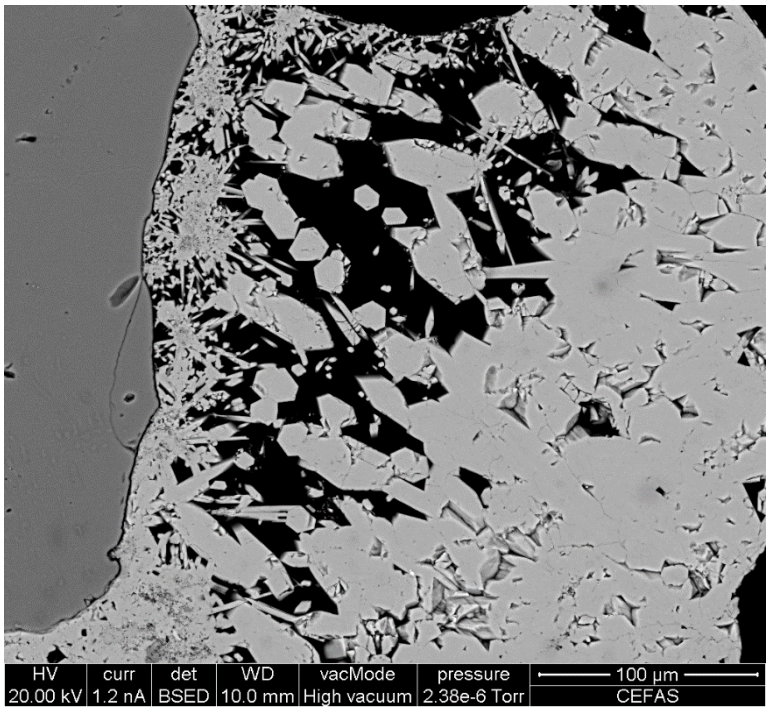

Plate 73. BSEM image detailing the acicular aragonite. Note the typical six-sided cross-sections through some of the crystals. The range in needle thickness observed in this sample is well illustrated in this image. Sample GT066.

ED-EPMA major element compositional data for the aragonite cements and examples of shelly fragments are given in Table 16. Their compositional variation, expressed in terms of molar proportions of CaO_3-$MgCO_3$ and $SrCO_3$, is summarised in Figure 17.

The aragonite is strontium bearing, with <1 mole % $SrCO_3$ in solid-solution (Table 16) (i.e. the structural formula (i.e. the structural formula of the aragonite can be represented as $Ca_{0.99-1.00}Sr_{0.01-0.00}CO_3$). The identification of aragonite during petrographic analysis is based on its prismatic morphology and the relatively high Sr content (cf. sample GT012 for further discussion).

The micritic magnesian calcite cements contain between 1 and 16 mole % $MgCO_3$ in solid solution (i.e. the structural formula of the calcite can be represented as $Ca_{0.57-0.64}Mg_{0.43-0.36}CO_3$). This is the lower end of the Mg values obtained from most of the micritic cements analysed in these Croker Carbonate Slab samples, and the analyses are likely to have been influenced by the incorporation of some intimately associated aragonite.

The sequence of sedimentary and post-depositional diagenetic events recorded from sample GT066 can be summarised as follows:

1. Deposition of shell-rich sand.
2. Precipitation of globular micrite, resulting in lithification of the sediment. There is evidence that this occurred in reducing environment, with the precipitation of framboidal pyrite closely associated with the micrite cement
3. Precipitation of a later stage acicular aragonite cement.

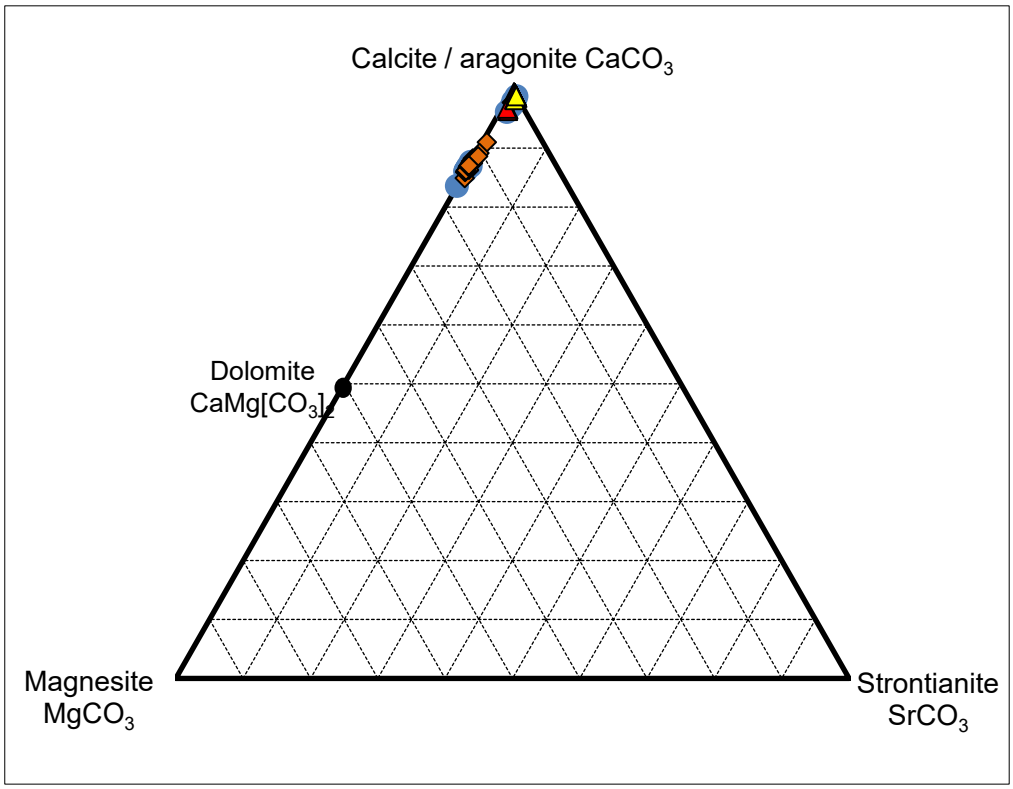

Figure 17. $CaCO_3$-$MgCO_3$-$SrCO_3$ molar ratio plot illustrating the compositions of the high-magnesian calcite micritic cement (solid blue circles), bioclastic debris (orange diamonds), aragonite (red triangles) and a shell (yellow triangles) from sample GT066.

Table 16. Electron microprobe analyses of carbonate cements and bioclastic fragments in sample GT066

		Weight % oxide (normalised)							Ionic ratio [normalised to 3 [O]						COMMENTS
SAMPLE	No	MgO	CaO	MnO	FeO	SrO	CO_2 (calc)	*Total wt%	Mg^{2+}	Ca^{2+}	Mn^{2+}	Fe^{2+}	Sr^{2+}	CO_3^{2-}	
GT066	1	5.25	48.51	1.24	0.27	0.00	44.73	100	0.13	0.85	0.02	0.00	0.00	1.00	micrite
GT066	2	5.58	48.30	1.00	0.32	0.00	44.80	100	0.14	0.85	0.01	0.00	0.00	1.00	micrite
GT066	3	5.52	48.04	1.39	0.28	0.00	44.76	100	0.13	0.84	0.02	0.00	0.00	1.00	micrite
GT066	4	5.59	47.93	1.28	0.43	0.00	44.77	100	0.14	0.84	0.02	0.01	0.00	1.00	micrite
GT066	5	5.10	48.66	1.20	0.00	0.39	44.65	100	0.12	0.85	0.02	0.00	0.00	1.00	micrite
GT066	6	5.44	48.59	1.19	0.00	0.00	44.79	100	0.13	0.85	0.02	0.00	0.00	1.00	micrite
GT066	7	6.61	46.84	1.59	0.00	0.00	44.96	100	0.16	0.82	0.02	0.00	0.00	1.00	micrite
GT066	8	4.97	49.01	1.32	0.00	0.00	44.70	100	0.12	0.86	0.02	0.00	0.00	1.00	micrite
GT066	9	0.20	54.26	0.00	0.42	1.44	43.67	100	0.01	0.97	0.00	0.01	0.01	1.00	micrite
GT066	10	0.00	55.03	0.00	0.00	1.26	43.71	100	0.00	0.99	0.00	0.00	0.01	1.00	micrite
GT066	11	0.33	54.44	0.00	0.25	1.22	43.75	100	0.01	0.98	0.00	0.00	0.01	1.00	micrite
GT066	12	0.59	53.93	0.00	0.35	1.38	43.75	100	0.01	0.97	0.00	0.00	0.01	1.00	micrite
GT066	13	1.06	51.37	0.00	2.81	1.11	43.65	100	0.03	0.92	0.00	0.04	0.01	1.00	micrite
GT066	14	0.00	55.10	0.00	0.00	1.17	43.73	100	0.00	0.99	0.00	0.00	0.01	1.00	shell
GT066	15	0.23	54.85	0.00	0.00	1.15	43.77	100	0.01	0.98	0.00	0.00	0.01	1.00	shell
GT066	16	0.22	54.74	0.00	0.00	1.30	43.74	100	0.01	0.98	0.00	0.00	0.01	1.00	shell
GT066	17	0.00	55.26	0.00	0.00	0.97	43.77	100	0.00	0.99	0.00	0.00	0.01	1.00	shell
GT066	18	0.00	55.08	0.00	0.00	1.20	43.72	100	0.00	0.99	0.00	0.00	0.01	1.00	shell
GT066	19	0.00	55.07	0.00	0.00	1.21	43.72	100	0.00	0.99	0.00	0.00	0.01	1.00	aragonite
GT066	20	0.00	55.08	0.00	0.00	1.20	43.72	100	0.00	0.99	0.00	0.00	0.01	1.00	aragonite
GT066	21	0.00	55.12	0.00	0.00	1.15	43.73	100	0.00	0.99	0.00	0.00	0.01	1.00	aragonite
GT066	22	0.00	55.03	0.00	0.00	1.26	43.71	100	0.00	0.99	0.00	0.00	0.01	1.00	aragonite
GT066	23	0.00	54.84	0.00	0.00	1.50	43.66	100	0.00	0.99	0.00	0.00	0.01	1.00	aragonite
GT066	24	0.18	54.94	0.00	0.00	1.11	43.77	100	0.00	0.98	0.00	0.00	0.01	1.00	aragonite
GT066	25	0.00	55.23	0.00	0.00	1.01	43.76	100	0.00	0.99	0.00	0.00	0.01	1.00	aragonite
GT066	26	0.00	55.17	0.00	0.00	1.08	43.75	100	0.00	0.99	0.00	0.00	0.01	1.00	aragonite
GT066	27	0.00	55.14	0.00	0.00	1.12	43.74	100	0.00	0.99	0.00	0.00	0.01	1.00	aragonite
GT066	28	0.00	55.19	0.00	0.00	1.06	43.75	100	0.00	0.99	0.00	0.00	0.01	1.00	aragonite
GT066	29	0.00	55.49	0.00	0.00	0.69	43.83	100	0.00	0.99	0.00	0.00	0.01	1.00	aragonite
GT066	30	0.00	55.54	0.00	0.00	0.62	43.84	100	0.00	0.99	0.00	0.00	0.01	1.00	aragonite
GT066	31	0.00	55.25	0.00	0.24	0.71	43.80	100	0.00	0.99	0.00	0.00	0.01	1.00	aragonite
GT066	32	0.00	55.36	0.00	0.00	0.84	43.80	100	0.00	0.99	0.00	0.00	0.01	1.00	aragonite

		Weight % oxide (normalised)							Ionic ratio [normalised to 3 [O]						COMMENTS
SAMPLE	No	MgO	CaO	MnO	FeO	SrO	CO_2 (calc)	*Total wt%	Mg^{2+}	Ca^{2+}	Mn^{2+}	Fe^{2+}	Sr^{2+}	CO_3^{2-}	
GT066	33	0.00	55.64	0.00	0.00	0.50	43.86	100	0.00	1.00	0.00	0.00	0.00	1.00	aragonite
GT066	34	0.00	55.45	0.00	0.00	0.73	43.82	100	0.00	0.99	0.00	0.00	0.01	1.00	aragonite
GT066	35	0.00	55.42	0.00	0.00	0.77	43.81	100	0.00	0.99	0.00	0.00	0.01	1.00	aragonite
GT066	36	0.00	55.44	0.00	0.00	0.74	43.82	100	0.00	0.99	0.00	0.00	0.01	1.00	aragonite
GT066	37	0.89	52.46	0.00	1.82	1.11	43.72	100	0.02	0.94	0.00	0.03	0.01	1.00	aragonite
GT066	38	0.99	53.16	0.00	0.83	1.20	43.81	100	0.02	0.95	0.00	0.01	0.01	1.00	aragonite
GT066	39	0.00	55.41	0.00	0.00	0.79	43.81	100	0.00	0.99	0.00	0.00	0.01	1.00	aragonite
GT066	40	0.00	55.46	0.00	0.00	0.71	43.82	100	0.00	0.99	0.00	0.00	0.01	1.00	aragonite
GT066	41	0.97	53.63	0.00	0.63	0.89	43.89	100	0.02	0.96	0.00	0.01	0.01	1.00	aragonite
GT066	42	5.47	49.27	0.00	0.00	0.44	44.82	100	0.13	0.86	0.00	0.00	0.00	1.00	acicular material, possibly shelly debris
GT066	43	4.70	50.21	0.00	0.00	0.39	44.69	100	0.11	0.88	0.00	0.00	0.00	1.00	acicular material, possibly shelly debris
GT066	44	5.23	49.91	0.00	0.00	0.00	44.86	100	0.13	0.87	0.00	0.00	0.00	1.00	acicular material, possibly shelly debris
GT066	45	5.12	50.03	0.00	0.00	0.00	44.85	100	0.12	0.88	0.00	0.00	0.00	1.00	acicular material, possibly shelly debris
GT066	46	5.03	50.14	0.00	0.00	0.00	44.83	100	0.12	0.88	0.00	0.00	0.00	1.00	acicular material, possibly shelly debris
GT066	47	4.82	50.39	0.00	0.00	0.00	44.79	100	0.12	0.88	0.00	0.00	0.00	1.00	acicular material, possibly shelly debris
GT066	48	5.37	49.74	0.00	0.00	0.00	44.89	100	0.13	0.87	0.00	0.00	0.00	1.00	acicular material, possibly shelly debris
GT066	49	4.95	49.88	0.00	0.00	0.45	44.72	100	0.12	0.87	0.00	0.00	0.00	1.00	acicular material, possibly shelly debris
GT066	50	5.91	47.85	0.97	0.00	0.46	44.80	100	0.14	0.84	0.01	0.00	0.00	1.00	acicular material, possibly shelly debris
GT066	51	5.37	48.76	1.08	0.00	0.00	44.79	100	0.13	0.85	0.01	0.00	0.00	1.00	acicular material, possibly shelly debris
GT066	52	5.37	48.56	0.96	0.00	0.38	44.72	100	0.13	0.85	0.01	0.00	0.00	1.00	acicular material, possibly shelly debris
GT066	53	5.65	48.20	0.99	0.35	0.00	44.81	100	0.14	0.84	0.01	0.00	0.00	1.00	acicular material, possibly shelly debris
GT066	54	3.33	50.82	0.83	0.00	0.70	44.32	100	0.08	0.90	0.01	0.00	0.01	1.00	acicular material, possibly shelly debris
GT066	55	4.84	48.67	1.41	0.45	0.00	44.62	100	0.12	0.86	0.02	0.01	0.00	1.00	acicular material, possibly shelly debris
GT066	56	4.14	49.83	1.01	0.00	0.54	44.48	100	0.10	0.88	0.01	0.00	0.01	1.00	acicular material, possibly shelly debris
GT066	57	5.54	48.07	1.27	0.35	0.00	44.77	100	0.14	0.84	0.02	0.00	0.00	1.00	acicular material, possibly shelly debris
GT066	58	0.48	54.62	0.00	0.00	1.08	43.83	100	0.01	0.98	0.00	0.00	0.01	1.00	acicular material, possibly shelly debris
GT066	59	4.32	49.57	0.97	0.00	0.66	44.49	100	0.11	0.87	0.01	0.00	0.01	1.00	acicular material, possibly shelly debris
GT066	60	5.55	48.39	0.76	0.50	0.00	44.80	100	0.14	0.85	0.01	0.01	0.00	1.00	acicular material, possibly shelly debris
GT066	61	5.34	49.14	0.30	0.40	0.00	44.82	100	0.13	0.86	0.00	0.01	0.00	1.00	acicular material, possibly shelly debris
GT066	62	5.32	49.80	0.00	0.00	0.00	44.88	100	0.13	0.87	0.00	0.00	0.00	1.00	acicular material, possibly shelly debris

**Note: Some analytical totals were low (<90%) because of the microporous nature of the cements. Therefore all data were normalised to 100%*

4.14 SAMPLE GT071

Sample GT071 comprises numerous angular to sub-angular clasts (<100 mm diameter) of fine-grained, grey-buff coloured sandstone (Plate 74). Surfaces show some orange-brown staining from iron oxyhydroxide indicating they have suffered oxidative weathering. Some minor bioturbation has occurred.

Plate 74. Photograph of the clasts which comprise sample GT071. Field of view ~225 mm wide.

The detrital mineralogy is similar to that described in the previous samples, being dominated by quartz, with subordinate feldspar. The sandstone is reasonably well sorted, with angular to sub-angular grains (<200 µm). It has a close-packed, grain-supported fabric with simple-point grain contacts. No evidence of compactional deformation was observed. The thin section scan shows a patchy orange-brown colouration due to finely disseminated iron oxyhydroxides in the matrix and on grain surfaces (Plate 75). There is some limited secondary porosity where unstable detrital framework grains and some shell fragments have dissolved out (Plate 76).

The micritic high magnesian calcite cement forms globular aggregates (Plate 76). High resolution BSEM shows fine-grained euhedral rhombic microcrystals of calcite have nucleated around micro-cavities 1-2 µm diameter, giving the micrite a microporous texture, that may represent a microcellular fabric. These structures very closely resemble fossilised and mineralised bacterial cells, as discussed previously in sample GT004.

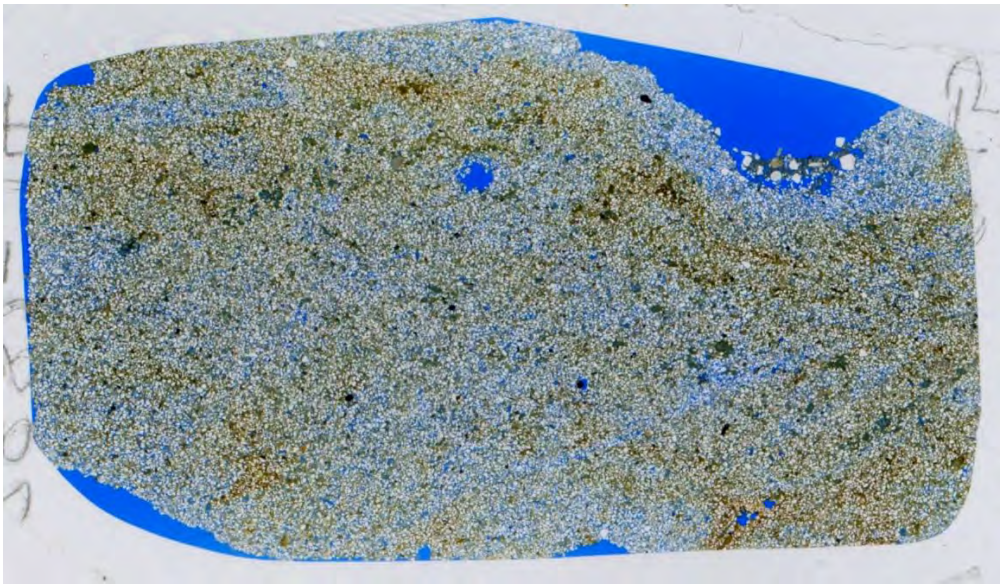

Plate 75. Scanned image of thin section prepared from sample GT071. Field of view = 48 mm wide.

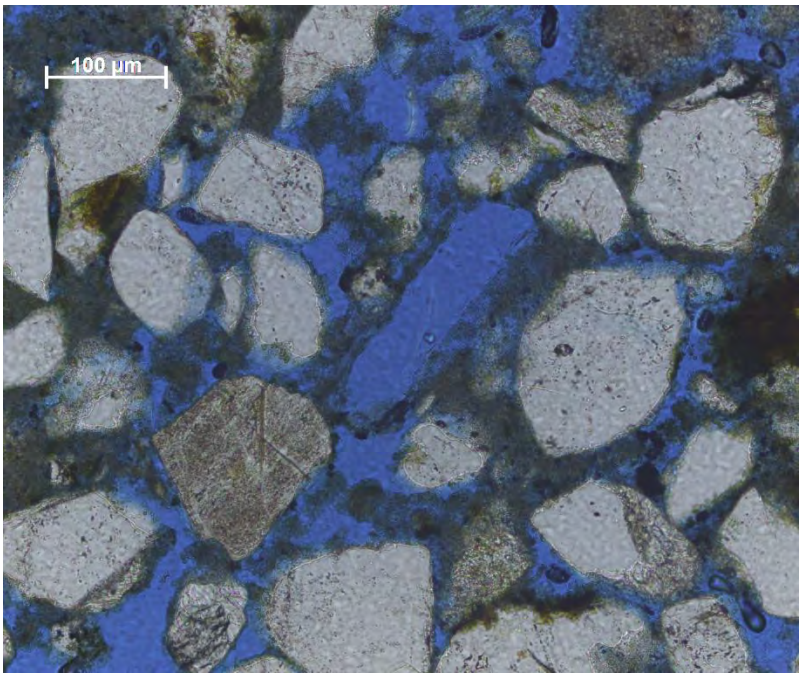

Plate 76. Transmitted light photomicrograph showing the grain supported fabric, globular micritic cement and an example of a large secondary pore (centre) resulting from the dissolution of an elongate detrital grain or shell fragment. Sample GT071

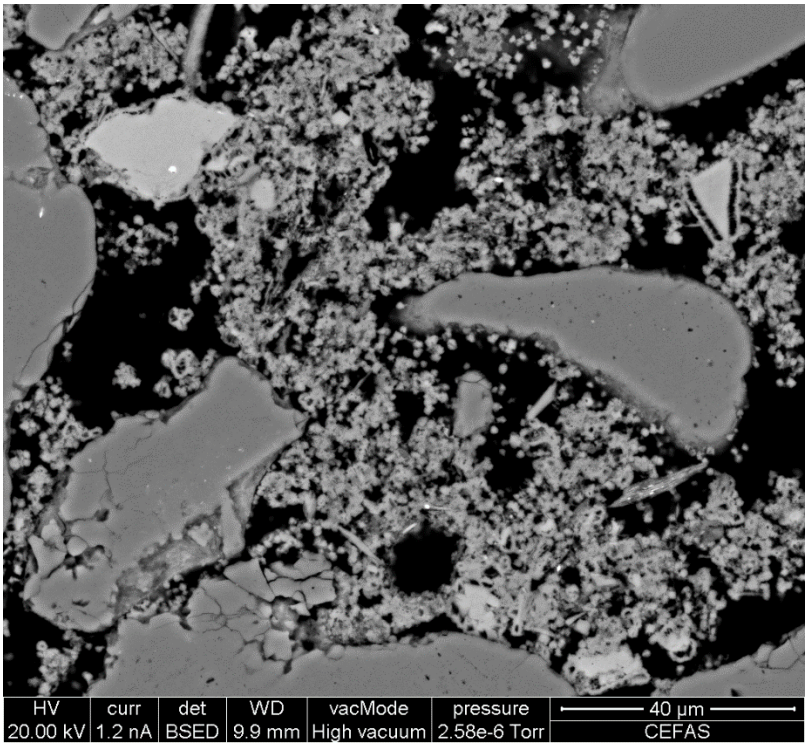

Plate 77. BSEM image detailing the micritic cement. Small rhombs of calcite are present, as well as aggregates which have nucleated around microcavities 1-2 µm in diameter. Sample GT071.

ED-EPMA analysis of the carbonate cements are presented in Table 17 and are summarised in Figure 18. The micritic magnesian calcite cements range in composition between 27 and 39 mole % $MgCO_3$ in solid solution (i.e. the structural formula of the calcite can be represented as $Ca_{0.61-0.73}Mg_{0.39-0.27}CO_3$).

The shell fragments appear to be pure calcite with no detectable levels of Sr.

The sequence of sedimentary and post-depositional diagenetic events recorded from sample GT071 can be summarised as follows:

1. Deposition of fine sand sediment.
2. Minor syndepositional bioturbation.
3. Precipitation of micritic high-magnesian calcite, causing lithification.
4. Some later boring of the lithified clast surfaces by marine biota, and minor oxidation within the cement and around some grain margins.

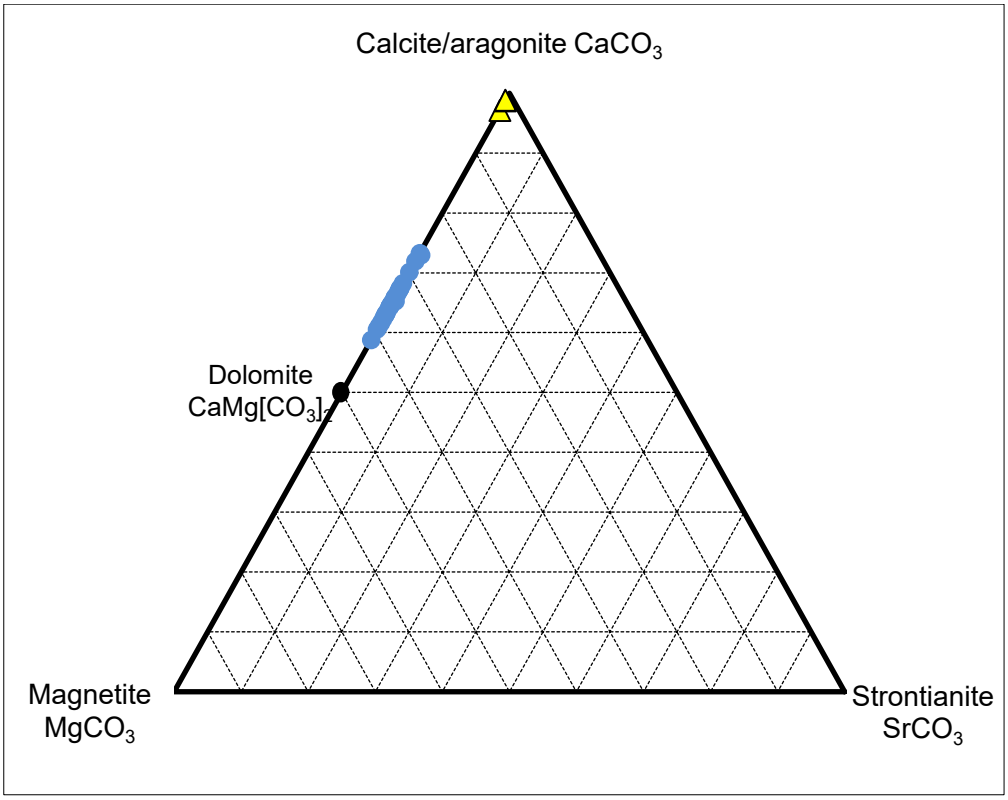

Figure 18. $CaCO_3$-$MgCO_3$-$SrCO_3$ molar ratio plot illustrating the compositions of the high-magnesian micritic cement (solid blue circles) and shell fragments (yellow triangles) from sample GT071.

Table 17. Electron microprobe analyses of carbonate cements and shell fragments in sample GT071

		Weight % oxide (normalised)							Ionic ratio [normalised to 3 [O]						COMMENTS
SAMPLE	No	MgO	CaO	MnO	FeO	SrO	CO_2 (calc)	*Total wt%	Mg^{2+}	Ca^{2+}	Mn^{2+}	Fe^{2+}	Sr^{2+}	CO_3^{2-}	
GT071	1	1.15	54.69	0.00	0.00	0.00	44.16	100	0.03	0.97	0.00	0.00	0.00	1.00	shell
GT071	2	0.50	55.08	0.00	0.41	0.00	44.01	100	0.01	0.98	0.00	0.01	0.00	1.00	shell
GT071	3	0.47	55.48	0.00	0.00	0.00	44.05	100	0.01	0.99	0.00	0.00	0.00	1.00	shell
GT071	4	13.76	39.90	0.00	0.00	0.00	46.33	100	0.32	0.68	0.00	0.00	0.00	1.00	micrite
GT071	5	13.76	39.40	0.00	0.57	0.00	46.28	100	0.32	0.67	0.00	0.01	0.00	1.00	micrite
GT071	6	11.76	41.92	0.00	0.37	0.00	45.95	100	0.28	0.72	0.00	0.00	0.00	1.00	micrite
GT071	7	11.20	42.60	0.00	0.00	0.39	45.81	100	0.27	0.73	0.00	0.00	0.00	1.00	micrite
GT071	8	15.04	38.19	0.00	0.24	0.00	46.53	100	0.35	0.64	0.00	0.00	0.00	1.00	micrite
GT071	9	14.02	37.59	0.00	2.22	0.00	46.16	100	0.33	0.64	0.00	0.03	0.00	1.00	micrite
GT071	10	14.95	38.52	0.00	0.00	0.00	46.54	100	0.35	0.65	0.00	0.00	0.00	1.00	micrite
GT071	11	14.16	39.44	0.00	0.00	0.00	46.40	100	0.33	0.67	0.00	0.00	0.00	1.00	micrite
GT071	12	11.18	42.69	0.00	0.27	0.00	45.86	100	0.27	0.73	0.00	0.00	0.00	1.00	micrite
GT071	13	14.95	38.52	0.00	0.00	0.00	46.54	100	0.35	0.65	0.00	0.00	0.00	1.00	micrite
GT071	14	13.77	39.58	0.00	0.35	0.00	46.30	100	0.32	0.67	0.00	0.00	0.00	1.00	micrite
GT071	15	13.41	40.10	0.00	0.24	0.00	46.25	100	0.32	0.68	0.00	0.00	0.00	1.00	micrite
GT071	16	13.97	39.66	0.00	0.00	0.00	46.37	100	0.33	0.67	0.00	0.00	0.00	1.00	micrite
GT071	17	15.21	38.21	0.00	0.00	0.00	46.58	100	0.36	0.64	0.00	0.00	0.00	1.00	micrite
GT071	18	15.18	37.94	0.00	0.33	0.00	46.54	100	0.36	0.64	0.00	0.00	0.00	1.00	micrite
GT071	19	14.54	38.43	0.00	0.24	0.44	46.35	100	0.34	0.65	0.00	0.00	0.00	1.00	micrite
GT071	20	15.88	37.43	0.00	0.00	0.00	46.70	100	0.37	0.63	0.00	0.00	0.00	1.00	micrite
GT071	21	12.63	41.23	0.00	0.00	0.00	46.14	100	0.30	0.70	0.00	0.00	0.00	1.00	micrite
GT071	22	15.15	36.20	0.00	2.29	0.00	46.35	100	0.36	0.61	0.00	0.03	0.00	1.00	micrite
GT071	23	14.13	37.67	0.00	1.99	0.00	46.20	100	0.33	0.64	0.00	0.03	0.00	1.00	micrite
GT071	24	14.70	37.57	0.00	1.37	0.00	46.36	100	0.35	0.64	0.00	0.02	0.00	1.00	micrite
GT071	25	14.34	38.37	0.00	0.96	0.00	46.34	100	0.34	0.65	0.00	0.01	0.00	1.00	micrite
GT071	26	14.63	37.58	0.00	1.45	0.00	46.34	100	0.34	0.64	0.00	0.02	0.00	1.00	micrite
GT071	27	15.57	34.03	0.00	4.16	0.00	46.24	100	0.37	0.58	0.00	0.06	0.00	1.00	micrite
GT071	28	16.84	33.44	0.00	3.16	0.00	46.56	100	0.39	0.56	0.00	0.04	0.00	1.00	micrite
GT071	29	14.92	37.44	0.00	1.23	0.00	46.41	100	0.35	0.63	0.00	0.02	0.00	1.00	micrite
GT071	30	15.22	35.97	0.00	2.47	0.00	46.34	100	0.36	0.61	0.00	0.03	0.00	1.00	micrite
GT071	31	15.59	33.28	0.00	4.96	0.00	46.17	100	0.37	0.57	0.00	0.07	0.00	1.00	micrite
GT071	32	14.16	31.75	0.00	8.50	0.00	45.58	100	0.34	0.55	0.00	0.11	0.00	1.00	micrite

		Weight % oxide (normalised)							Ionic ratio [normalised to 3 [O]						COMMENTS
SAMPLE	No	MgO	CaO	MnO	FeO	SrO	CO_2 (calc)	*Total wt%	Mg^{2+}	Ca^{2+}	Mn^{2+}	Fe^{2+}	Sr^{2+}	CO_3^{2-}	
GT071	33	15.76	36.37	0.00	1.32	0.00	46.55	100	0.37	0.61	0.00	0.02	0.00	1.00	micrite
GT071	34	15.39	37.15	0.00	0.93	0.00	46.52	100	0.36	0.63	0.00	0.01	0.00	1.00	micrite
GT071	36	14.25	38.60	0.00	0.82	0.00	46.34	100	0.34	0.65	0.00	0.01	0.00	1.00	micrite

**Note: Some analytical totals were low (<90%) because of the microporous nature of the cements. Therefore all data were normalised to 100%*

Glossary

Anhedral	Crystal morphology with no obvious crystal shape or faces. Synonymous with xenomorphic.
BGS	British Geological Survey.
BSEM	Backscattered electron microscopy.
Cefas	Centre for Environment, Fisheries and Aquiculture Science.
ESEM	Environmental scanning electron microscope.
Euhedral	Crystal morphology with well-developed crystal shape and good planar faces. Synonymous with *idiomorphic*.
Idiomorphic	Crystal morphology with well-developed crystal shape and good planar faces. Synonymous with *euhedra*l.
JNCC	Joint Nature Conservancy Council.
EDXA	Energy-dispersive X-ray spectroscopy.
ESEM	Environmental scanning electron microscope microscopy.
ED-EPMA	Quantitative energy-dispersive electron probe microanalysis (i.e. quantitative EDXA).
MDAC	Methane-Derived Authigenic Carbonate.
SAC	Special Area of Conservation.
cSAC	Candidate Special Area of Conservation.
SCI	Site of Community Importance.
SEM	Scanning electron microscope / microscopy.
Subidiomorphic	Crystal morphology with some well-developed crystal shape and some crystal faces. Synonymous with *subhedral*.
Subhedral	Crystal morphology with some well-developed crystal shape and some crystal faces. Synonymous with *subidiomorphic.*
Xenomorphic	Crystal morphology with no obvious crystal shape or faces. Synonymous with anhedral.
XRD	X-ray diffraction.

References

British Geological Survey holds most of the references listed below, and copies may be obtained via the library service subject to copyright legislation (contact libuser@bgs.ac.uk for details). The library catalogue is available at: https://envirolib.apps.nerc.ac.uk/olibcgi.

ALTHOFF, P.L. 1977. Structural refinements of dolomite and a magnesian calcite and implications for dolomite formation in the marine environment. *American Mineralogist*, **62**, pages 772-783.

BERNER, R.A. 1969. The synthesis of framboidal pyrite. *Economic Geology,* **64**, 383-384.

BERNER, R.A. 1980. *Early Diagenesis: A Theoretical Approach*. Princeton University Press, Princeton, New Jersey, USA, 241pp.

BOHRMANN, G., GREINERT, J., SUESS, E. AND TORRES, M. 1998. Authigenic carbonates from the Cascadia subduction zone and their relation to gas hydrate stability. *Geology*, **26**, 647-650.

CALVERT, S.E. AND PRICE, N.B. 1970. Composition of Manganese Nodules and Manganese Carbonates from Loch Fyne, Scotland. *Contr. Mineral. And Petrol*. **29**, 215-233.

CALVERT, S.E. AND PRICE, N.B. 1977. Geochemical variation in ferromanganese nodules and associated sediments from the Pacific Ocean. *Marine Chemistry*. **5**, 43-74.

CHESTER, R. AND JICKELLS, T. (2012). Chapter 15.3 'Hydrogenous' components: halmyrolysates and precipitates. In: *Marine Geochemistry*, 3rd edition. Wiley-Blackwell. Chichester.

CLAYPOOL, G.E. AND KAPLAN, I.R. 1974. The origin and distribution of methane in marine sediments. In: KAPLAN, I.R. (editor) *Natural Gases in Marine Sediments*, Plenum Press, New York, 99-140.

COLEMAN,M.L. 1985. Geochemistry of diagenetic non-silicate minerals: kinetic considerations. In: EGLINTON, G., CURTIS, C.D. MCKENZIE, D.P. AND MURCHISON, D.G. (editors). *Geochemistry of Buried Sediments*. The Royal Society, London, 39-54

CRAIG, H. 1957. Isotopic standards for carbon and oxygen & correction factors for mass spectrometric analysis. *Geochimica et Cosmochimica Acta*, 12, 133-149.

CROKER , P.F., KOZACHENKO, M. AND WHEELER, A.J. 2005. Gas-related seabed structures in the Western Irish Sea (IRL-SEA6). *Technical Report of the Petroleum Affairs Division of Ireland, produced for Strategic Environmental Assessment – SEA6*

DEER, W.A., HOWIE, R.A. AND ZUSSMAN, J. 1962a. *Rock Forming Minerals. Volume 5: Non-Silicates*. Longmans, London.

DEER, W.A., HOWIE, R.A. AND ZUSSMAN, J. 1992b. *An Introduction to the Rock Forming Minerals (2nd edition)*. Pearson Education Limited, Harlow, London.

DEFRA. 2010. Charting *Progress 2: An assessment of the state of UK seas. Feeder Report: Ocean Processes*. UK Marine Monitoring and Assessment Strategy (UKMMAS) Community, Defra, United Kingdom. http://chartingprogress.defra.gov.uk.

GLASBY, G.P. 2006. Manganese: Predominant role of nodules and crusts. In: Schulz, H.D. and Zabel, M. (editors) *Marine Geochemistry*, 2nd ed. Springer, Germany.

GOLDSTEIN, J.I., NEWBURY, D.E., ECHLIN, P., JOY, D.C., FIORI, C. AND LIFSHIN, E. 1981. *Scanning Electron Microscopy and X-Ray Microanalysis*. Plenum Press, New York.

HAYS, P.D. AND GROSSMAN, E.L. 1991. Oxygen isotopes in meteoric calcite cements as indicators of continental paleoclimate. *Geology*, **19**, 441-444.

HOEFS, J. 2009. Stable Isotope Geochemistry. 6th edition. Springer. Berlin.

HOVLAND, M. AND TALBOT, M.R. 1987. Hydrocarbon seeps in northern marine waters; their occurrence and effects. *Journal of Sedimentary Research*, **57**.

JENSEN, P., AAGAARD, I., BURKE JR., R.A., DANDO, P.R., JØGENSEN, N.O., KUIJPERS, A., LAIER, T., O'HARA, S.C.M. AND SCHMALJOHANN, R. 1992. 'Bubbling reefs' in the Kattegat: submarine landscapes of carbonate-cemented rocks support a diverse ecosystem at methane seeps. *Marine Ecology Progress Series*, **83**, 103-112.

JNCC. 2003. *Irish Sea Pilot*. Joint Nature Conservation Committee (JNCC). http://www.jncc.gov.uk/pdf/irish_finalreport(maps).pdf

JNCC, 2012. Offshore Special Area of Conservation: Croker Carbonate Slabs. SAC Selection Assessment Document V5.0. http://jncc.defra.gov.uk/pdf/CrokerCarbonateSlabs_SACSAD_v_5_0.pdf

JUDD, A.G. 2005. The distribution and extent of methane-derived authigenic carbonate. *DTI Strategic Environmental Assessment, Area 6 (SEA6)*. United Kingdom Department of Trade and Industry (Dti)

KIM, S.T. AND O'NEIL, J.R., 1997. Equilibrium and non-equilibrium oxygen isotope effects in synthetic carbonates. *Geochimica et Cosmochimica Acta*, 61, 3461–3475.

KIM, S.T. et al 2007. Phosphoric acid fractionation factors for Calcite and Aragonite between 25 and 75 °C*: Revisited Chemical Geology* 246 (2007) 135-146

KNIGHT, P.J., WILKINSON, M. AND GLORIOSO, P. 1993. Current profile and sea-bed pressure and temperature records from the northern North Sea Challenger cruises 84 and 85: September 1991 – November 1991. *Proudman Oceanic Laboratory Report*, **28 (1993)**, 417pp.

KONHAUSER, K. 2007. *Inroduction to Geomicrobiology*. Blackwell Publishing, Oxford, UK, 425pp.

LAND, L.S., 1980. The isotopic and trace element geochemistry of dolomite: the state of the art. In: ZENGER, D.H., ET AL. (Editor.), Concepts and Models of Dolomitisation, Society of Economic *Paleontologists and Mineralogists (SEPM), Special Publication*, **28**, 87–110, Tulsa, Oklahoma.

LENG, M.J. AND MARSHALL, J.D. 2004. Palaeoclimate interpretation of stable isotope data from lake sediment archives. *Quaternary Science Reviews*, **23**, 811-831.

LIESKI, L.E. AND RAYMO, M.E. 2005. A Pliocene-Pleistocene stack of 57 globally distributed benthic $\delta_{18}O$ records. *Paleooceanography*, **20**, PA1003, 17pp, .doi:10.1029/2004PA001071

MACHEL, H.G. 1987. Some aspects of diagenetic sulphate-hydrocarbon redox reactions. In: Marshall, J.D. (editor) *Diagenesis of Sedimentary Sequences.* Geological Society of London, Special Publication, **36**, 15-28.

MACKENZIE, F.T., BISCHOFF, W.D., BISHOP, F.C., LOIJENS, /M., SCHOONMAKER, J. AND WOLLAST, R. 1983. Chapter 4. Magnesian calcites: low-temperature occurrence, solubility and solid-solution behaviour. In: REEDER, R.J. (editor). *Carbonates: Mineralogy and Chemistry. Reviews in Mineralogy,* Volume 11, Mineralogical Society of America, Washington D.C. USA, pp. 97-144.

MARTILL, D.M. AND WILBY, P.R. 1994. Lithified prokaryotes associated with fossil soft tissues from the Santana Formation (cretaceous) of Brazil. *Kaupia.* **4**, 71-77.

MCCREA, J., 1950. On the isotopic chemistry of carbonates and palaeo-temperature scale. *Jour. Chem. Physics*, 18, 849-57.

MILODOWSKI, A.E. TULLBORG, E.-L., BUIL, B., GÓMEZ, P., TURRERO, M.-J., HASZELDINE, S., ENGLAND, G., GILLESPIE, M.R., TORRES, T., ORTIZ, J.E., ZACHARIÁŠ, SILAR, J., CHVÁTAL, M., STRNAD, L., ŠEBEK, O. BOUCH, J.E., CHENERY, S.R., CHENERY, C., SHEPHERD, T.J. AND MCKERVEY, J.A. 2005. Application of Mineralogical, Petrological and Geochemical tools for Evaluating the Palaeohydrogeological Evolution of the PADAMOT Study Sites. PADAMOT PROJECT - EU FP5 CONTRACT NO. FIKW-CT2001-20129. *PADAMOT Project Technical Report, WP2*. 228pp +digital appendices.

MILODOWSKI, A.E. LACINSKA, A. AND SLOANE, H. 2009. Petrography and stable isotope geochemistry of samples of methane-derived authigenic carbonates (MDAC) from the Mid Irish Sea. *British Geological Survey, Commissioned Report*, **CR/09/051**, 62pp.

MILODOWSKI, A.E. AND SLOANE, H. 2013. Petrography and stable isotope geochemistry of samples of methane-derived authigenic carbonates (MDAC) from the Braemar Pockmark Area, North Sea. *British Geological Survey, Commissioned Report*, **CR/13/078**, 112pp.

MOZLEY, P. AND BURNS, S.J. 1993. Oxygen and carbon isotope comparison of marine carbonate concretions: an overview. *Journal of Sedimentary Petrology*, **63**, 73-83.

MURALIDHAR, K., MAZUMDAR, A., KARISIDDAIAH, S.M., BOROLE, D.V. AND RAO, B.R. 2006. evidences of methane-derived authigenic carbonates from the sediments of the Krishna-Godavari Basin, eastern continental margin of India. *Current Science*, **91**, 318-323.

PECKMANN, J., REIMER, A., LUTH, U., HANSEN, B.T., HEINICKE, C., HOEFS, J. AND REITNER, J. 2001. Methane-derived carbonates and authigenic pyrite from the northwestern Black Sea. *Marine Geology*, **177**, 129-150.

PIRRIE, D AND MARSHALL, J.D. 1991. Field relationships and stable isotope geochemistry of concretions from James Ross Island, Antarctica. *Sedimentary Geology*, **71**, 137-150.

REEDER, R.J. 1983. Chapter 1. Crystal chemistry of the rhombohedral carbonates. In: REEDER, J.J. (editor), *Carbonates: Mineralogy and Chemistry*, Reviews in Mineralogy, **11**, Mineralogical Society of America, Washington D.C. USA,. pp. 1-47.RICKARD, D.T. 1970. The origin of framboids. *Lithos,* 3, 269-293. 96

RICKARD, D.T. 1975. Kinetics and mechanism of pyrite formation at low temperatures. American Journal of Science, 274, 636-652.

ROHLING E.J. 2013. Oxygen Isotope Composition of Seawater. In: ELIAS, S.A. (editor) *The Encyclopedia of Quaternary Science*, vol. 2, pp. 915-922. Elsevier, Amsterdam.

ROSENBAUM J., and SHEPPARD S.M.F. 1986. An Isotopic study of siderites, dolomites and ankerites at high temperatures *Geochimica et Cosmochimica Acta*, **50**, 1147-1150

SAKAI, H., GAMO, T., OGAWA, Y. AND BOULEGUE, J. 1992. Stable isotope ratios and origins of the carbonates associated with cold seepage at the eastern Nankai Trough: fluids in convergent margins. *Earth and Planetary Science Letters*, **3-4**, 391-404.

SEARL, A. 1994. Discontinuous solid-solution in Ca-rich dolomites: the evience and implications of dolomite petrographic and geochemical data. *Special Publication of the International Association of Sedimentologists*, **21**, 361-376.

SCHMIDT, V. AND MCDONALD, D.A. 1979. Texture recognition of secondary porosity in sandstones. *In*: SCHOLLE, P.A. AND SCHLUGER, P.R. (editors). *Aspects of Diagenesis*. Society of Economic Paleontologists and Mineralogists Special Publication, **26**, 209-225.

SCHMIDT, G.A., BIGG, G.R. AND ROHLING, E.J. 1999. *Global Seawater Oxygen-18 Database*. http://data.giss.nasa.gov/o18data/.

SCHRAG, D.P., ADKINS, J.F., MCINTYRE, K., ALEXANDER, J.L., HODELL, D.A., CHARLES, C.D. AND MCMANUS, J.F. 2002. The oxygen isotopic composition of seawater during the Last Glacial Maximum. *Quaternary Science Reviews*, **21**, 331–342.

SHARMA, T. AND CLAYTON, R.N. (1965). Quoted in: Friedman I. and O'Neil J .R. 1977. Compilation of stable isotope fractionation factors of geochemical interest. Fleischer (Ed), *Data of Geochemistry, 6th Ed*. United States Geological Survey, Professional Paper 440-KK.SKINNER, H.C.W. 1963. Precipitation of calcian dolomites and magnesian calcites in the southeast of South Australia. *American Journal of Science*, **261**, 449-472.

SWEENEY, R.E. AND KAPLAN, I.R. 1973. Pyrite framboid formation: laboratory synthesis and marine sediments. *Economic Geology*, **68**, 618-634.

TARUTANI, T., CLAYTON, R.N., AND MAYEDA, T. 1969. The effect of polymorphism and magnesium substitution on oxygen isotope fractionation between calcium carbonate and water. *Geochimica et Cosmochimica Acta*, **33**, 987–996.

TUCKER, M.E., 2001. *Sedimentary Petrology: an introduction to the origin of sedimentary rocks*, 3rd ed. Blackwell, UK.

VAHRENKAMP, V.C AND SWART, P.K., 2001.Late Cenozoic dolomites of the Bahamas: metastable analogues for the genesis of ancient platform dolomites. *Special Publication of the International Association of Sedimentologists,* **21**, 133-153.

VERNON, R.H.., 2004. *A practical guide to Rock Microstructure*, 1st ed. Cambridge University Press, UK.

WHORMERSLEY, P., WILSON, C., LIMPENNY, D. AND LESLIE, A. 2008. Understanding the marine environment – seabed habitat investigations of Submarine structures in the mid-Irish Sea and Solan Bank Area of Search (AoS) – cruise report. JNCC Contract No: F90-01-1200. *CEFAS Cruise Report* **CEND 11/08**, 120pp. JNCC CONTRACT NO: F90-01-1200.

WILBY P.R., AND WHYTE, M.A. 1995. Phosphatized soft tissue in bivalves from the Portland Roach of Dorset (Upper Jurassic) *Geological Magazine***, 132,** 117-120.